ENVIROMENTALLY BENIGN SYNTHESIS AND APPLICATION OF SOME SPINEL FERRITE NANOPARTILCES

A Thesis
Presented to
The Academic Faculty

by

Lisa A. Vaughan

In Partial Fulfillment
of the Requirements for the
Doctor of Philosophy in the
School of Chemistry and Biochemistry

Georgia Institute of Technology
August 2011

ENVIROMENTALLY BENIGN SYNTHESIS AND APPLICATION OF SOME SPINEL FERRITE NANOPARTILCES

Approved by:

Dr. Z. John Zhang, Advisor
School of Chemistry and Biochemistry
Georgia Institute of Technology

Dr. Mostafa El-Sayed
School of Chemistry and Biochemistry
Georgia Institute of Technology

Dr. Angus Wilkinson
School of Chemistry and Biochemistry
Georgia Institute of Technology

Dr. Jiří Janata
School of Chemistry and Biochemistry
Georgia Institute of Technology

Dr. Chris Jones
College of Engineering
Georgia Institute of Technology

Date Approved: June 29, 2011

ACKNOWLEDGEMENTS

I would like to express my gratitude to all those who provided support and assistance to me during the completion of my thesis. First, I would like to thank John Zhang, my advisor, who supported and guided me during my graduate years. His experience and patience helped me achieve my goals. I would also like to thank my committee members, Angus Wilkinson, Jiří Janata, Mostafa El-Sayed, and Chris Jones, for all their support. I have learned so much from all the valuable conversations with them. Their suggestions and guidance have made the quality of my work better and my time at Tech richer.

Next, I would like to thank Angus Wilkinson and Jiří Janata for using of their instruments over the course of my graduate career and never being too surprised at finding me in their labs at all hours. My appreciated and thanks also are extended to Yolande Berta for all her help with TEM from training to EDS help.

I would also like to acknowledge my colleagues for their training, suggestions, and patience. Without Dr. Man Han, my first few years at Tech would have been much rockier. Man was generous with his time, knowledge, and patience. Much thanks goes to Hyungie Doo and Gabriel Hernandez for all their help and support. I would also like to thank Dan Sabo for putting up with my craziness for five long years. Hopefully, we have both learned from each.

I am also grateful to my family and friends as this would not have been possible without their encouragement. Finally, I would like to thank my husband, Peter Vaughan, for supporting me and pushing me to be the best I could. I am not sure I would have finished without him.

TABLE OF CONTENTS

Page

ACKNOWLEDGEMENTS iv

LIST OF TABLES xii

LIST OF FIGURES xiii

SUMMARY xix

CHAPTER

1 Introduction 1

- 1.1 Applications of Magnetic Nanoparticles 1
  - 1.1.1 Sensors 2
  - 1.1.2 Separations 3
- 1.2 Synthesis Methods for Magnetic Nanoparticles 4
  - 1.2.1 Mechanical Milling Methods 7
  - 1.2.2 Combustion Methods 8
  - 1.2.3 Sol-Gel Methods 9
  - 1.2.4 Micelle Methods 10
  - 1.2.5 Thermal Decomposition Methods 11
  - 1.2.6 Aminolytic Synthesis Method 12
- 1.3 Instrumentation and Characterization 13
  - 1.3.1 X-ray Diffraction 13
  - 1.3.2 Transmission Electron Microscopy 15
  - 1.3.3 SQUID Magnetometry 16
  - 1.3.4 Inductively Coupled Plasma Optical Emission Spectroscopy 20
  - 1.3.5 Photoacoustic Infrared Spectroscopy 21

1.3.6 X-ray Photoelectron Spectroscopy 22

1.4 Spinel Ferrites 23

1.4.1 Unit Cell and Crystal Structure 23

1.4.2 Magnetic Arrangement and Properties 24

1.4.2.1 Magnetic Arrangement 24

1.4.2.2 Single Domain Particle 26

1.4.2.3 Superparamagnetism 26

1.4.2.4 Magnetic Anisotropy 28

1.4.3 Couplings and their effect on magnetic response 29

2 Facile Synthesis of Monodispersed Manganese Ferrite via Aminolytic Reaction in Non-aqueous Medium. 32

2.1 Abstract 32

2.2 Introduction 32

2.3 Experimental 34

2.3.1 Synthesis of Precursors 34

2.3.2 Synthesis of $MnFe_2O_4$ Nanoparticles 35

2.3.3 Surface Stripping of $MnFe_2O_4$ Nanoparticles 35

2.3.4 Heat Treatment of $MnFe_2O_4$ Nanoparticles in Both Ambient and Argon Atmosphere 36

2.4 Results and Discussion 36

2.4.1 Physical and Magnetic Properties of Native Nanoparticles 36

2.4.2 Surface Treatment Effects on Physical and Magnetic Properties 42

2.5 Conclusion 48

3 The Effect of Mn Substitution on the Magnetic Properties of Cobalt Ferrite Nanoparticles 49

3.1 Abstract 49

3.2 Introduction 50

3.3 Experimental 52

3.3.1 Synthesis of Precursors 52

3.3.2 Synthesis of $Co_{1-x}Mn_xFe_2O_4$ Nanoparticles 53

3.4 Results and Discussion 53

3.5. Conclusions 60

4 Effect of Cr Substitution on the Magnetic Properties of Manganese Ferrite Nanoparticles 61

4.1 Abstract 61

4.2 Introduction 62

4.3 Experimental 63

4.3.1 Synthesis of Precursors 63

4.4 Results and Discussion 64

4.5 Conclusion 70

5 Solvent Longevity for Green Chemistry Synthesis of Magnetic Ferrite Nanoparticles 72

5.1 Abstract 72

5.2 Introduction 72

5.3 Experimental 74

5.3.1 Synthesis of Precursors 74

5.3.2 Synthesis of $CoFe_2O_4$ Nanoparticles 74

5.4 Results and Discussion 75

5.5 Conclusion 84

6 Synthesis and Characterization of Iron Oxides and Oxy Hydroxides Nanoparticles 85

6.1 Abstract 85

6.2 Introduction 85

6.3 Experimental 87

6.3.1 Synthesis of Goethite 87

6.3.2 Synthesis of Maghemite 88

6.3.3 Synthesis of Magnetite 88

6.3.4 Synthesis of Hematite 89

6.4 Results and Discussion 89

6.4.1 Physical and Magnetic Properties of Goethite 89

6.4.2 Physical and Magnetic Properties of Maghemite 93

6.4.3 Physical and Magnetic Properties of Magnetite 98

6.4.4 Physical and Magnetic Properties of Hematite 102

6.5 Conclusion 106

7 Removal of arsenite contaminant using iron oxides and oxy-hydroxides Nanoparticles 107

7.1 Abstract 107

7.2 Introduction 108

7.3 Experimental 112

7.3.1 Arsenic Stock Solutions 112

7.3.2 Different Phase Removal Affinity Comparison 112

7.3.3 Arsenic Removal by Maghemite to Detection Limit 113

7.3.4 Size Influence of Maghemite Nanoparticles on Arsenic Adsorption 113

7.3.5 Surface Regeneration Study with Maghemite Nanoparticles 114

7.3.6 Core-Shell Maghemite@$CoFe_2O_4$ and Hematite@$CoFe_2O_4$ Synthesis 114

7.3.7 Core-Shell Removal Affinity 115

7.4 Results and Discussion 115

7.4.1 Different Phase Removal Affinity Comparison 115

7.4.2 Arsenic Removal by Maghemite to Detection Limit 123

7.4.3 Size Influence of Maghemite Nanoparticles on Arsenic Adsorption 124

7.4.4 Surface Regeneration Study with Maghemite Nanoparticles 128

7.4.5 Core-Shell Removal Affinity 130

7.5 Conclusion 132

8 Removal of oxo-acid contaminants, arsenate and chromate, using iron oxides and oxy-hydroxides Nanoparticles 134

8.1 Abstract 134

8.2 Introduction 134

8.3 Experimental 135

8.3.1 Arsenic and Chromium Stock Solutions 135

8.3.2 Different Phase Removal Affinity Comparison 136

8.3.3 Size Influence of Maghemite Nanoparticles on Arsenic and Chromium Adsorption 137

8.3.4 Surface Regeneration Study with Maghemite Nanoparticles 137

8.4 Results and Discussion 137

  8.4.1 Different Phase Removal Affinity Comparison 137

  8.4.2 Size Influence of Maghemite Nanoparticles on Arsenic and Chromium Adsorption 146

  8.4.3 Surface Regeneration Study with Maghemite Nanoparticles 147

8.5 Conclusion 149

REFERENCES 150

VITA 164

LIST OF TABLES

Table 3.4: Elemental Analysis of $Co_{1-x}Mn_xFe_2O_4$ Nanoparticles 55

Table 4.4: Elemental Analysis of $MnFe_{2-x}Cr_xO_4$ Nanoparticles 65

Table 7.4: Freundlich Parameters for Arsenic Adsorbents 128

Table 8.4: Contaminant uptake by different phases of iron oxides and oxy-hydroxides 138

LIST OF FIGURES

		Page
Figure 1.1	Diagram of Bragg's diffraction	14
Figure 1.2	A typical magnetic susceptibility curve	19
Figure 1.3	A typical magnetic hysteresis loop	20
Figure 1.4	Spinel Ferrite Structure	24
Figure 1.5	Magnetic spinel ferrite structure	25
Figure 1.6	Unequal antiparallel alignment of magnetic moments in cobalt ferrite	25
Figure 1.7	Potential well schematic of anisotropy energy barrier for magnetic reversal	27
Figure 1.8	Coupling vectors in spinel ferrite system	30
Figure 2.1	X-ray diffraction patterns of ~8 nm $MnFe_2O_4$ nanoparticles	37
Figure 2.2	Temperature dependent magnetization of $MnFe_2O_4$	38
Figure 2.3	Size dependence of Blocking Temperature (T_B)	38
Figure 2.4	Hysteresis curves of $MnFe_2O_4$ nanoparticles at 5 K	39
Figure 2.5	Magnetic properties dependence size for $MnFe_2O_4$ nanoparticles	41
Figure 2.6	X-ray diffraction patterns of ~7 nm native, stripped, heated in argon, and heated in air $MnFe_2O_4$ nanoparticles	43
Figure 2.7	Hysteresis curves of native (o), stripped (□) heat treated in air (Δ) and in Ar (∗) spherical ~8 nm $MnFe_2O_4$ nanoparticles at 5 K	44
Figure 2.8	Magnetic properties dependence size for native (o), stripped (□) heat treated in air (Δ) and in Ar (∗) spherical ~8 nm $MnFe_2O_4$ nanoparticles	46

Figure 3.1 Cation Distribution of $CoFe_2O_4$ 51

Figure 3.2 Cation Distribution of $MnFe_2O_4$ 51

Figure 3.3 Powder X-Ray Diffractions pattern for ~5 nm $Co_{1-x}Mn_xFe_2O_4$ nanoparticles 54

Figure 3.4 Blocking Temperature (T_B) dependence on manganese doping for ~5 nm $Co_{1-x}Mn_xFe_2O_4$ nanoparticles 56

Figure 3.5 Overlaid hysteresis curves for varying doping amounts of manganese for ~5 nm $Co_{1-x}Mn_xFe_2O_4$ nanoparticles at 5 K 57

Figure 3.6 Magnetic properties dependence on manganese doping for ~5 nm $Co_{1-x}Mn_xFe_2O_4$ nanoparticles 59

Figure 4.1 Cation Distribution of $MnFe_2O_4$ 63

Figure 4.2 Powder X-Ray Diffractions pattern for ~8 nm $Mn_2Fe_{2-x}Cr_xO_4$ nanoparticles 65

Figure 4.3 Blocking Temperature(T_B) dependence on chromium doping for ~8 nm $Mn_2Fe_{2-x}Cr_xO_4$ nanoparticles 66

Figure 4.4 Overlaid hysteresis curves for varying doping amounts of chromium for ~8 nm $Mn_2Fe_{2-x}Cr_xO_4$ nanoparticles at 5 K 68

Figure 4.5 Magnetic properties dependence on chromium doping for ~8 nm $Mn_2Fe_{2-x}Cr_xO_4$ nanoparticles 69

Figure 5.1 TEM micrograph of CoFe2O4 nanoparticles 76

Figure 5.2 Rietveld refinement of powder XRDs for $CoFe_2O_4$ nanoparticles 77

Figure 5.3 H^1NMR of “mother” solution take in CD_2Cl_2 78

Figure 5.4 Size dependence of Blocking Temperature (T_B) for $CoFe_2O_4$ nanoparticles 79

Figure 5.5 Temperature dependent magnetization of $CoFe_2O_4$ produced with the “mother” solution 80

Figure 5.6 Overlaid hysteresis curves of $CoFe_2O_4$ nanoparticles at 5 K 81

Figure 5.7 Magnetic properties dependence on size for fresh solvent and re-used solvent synthesized $CoFe_2O_4$ nanoparticles 83

Figure 6.1 Relationships between iron phases 86

Figure 6.2 Unit cells of (a) Goethite, (b) Maghemite, (c) Magnetite, and (d) Hematite 87

Figure 6.3 Powder XRD pattern for goethite nanoparticles 90

Figure 6.4 TEM micrograph of goethite nanoparticles 90

Figure 6.5 Temperature dependent magnetization of goethite nanoparticles 91

Figure 6.6 Hysteresis curve of goethite nanoparticles at 5 K 92

Figure 6.7 PAS-IR Absorbance spectrum for goethite nanoparticles 92

Figure 6.8 EDS spectrum of goethite nanoparticles 93

Figure 6.9 Powder XRD pattern for maghemite nanoparticles 94

Figure 6.10 TEM micrograph of ~ 8 nm maghemite nanoparticles 94

Figure 6.11 XRD pattern stack plot showing conversion from maghemite to hematite 95

Figure 6.12 Temperature dependent magnetization of maghemite nanoparticles 96

Figure 6.13 Hysteresis curve of maghemite nanoparticles at 5 K 97

Figure 6.14 PAS-IR Absorbance spectrum for maghemite nanoparticles 97

Figure 6.15 EDS spectrum of maghemite nanoparticles 98

Figure 6.16 Powder XRD pattern for magnetite nanoparticles 99

Figure 6.17 TEM micrograph of magnetite nanoparticles 99

Figure 6.18 Temperature dependent magnetization of magnetite nanoparticles 100

Figure 6.19 Hysteresis curve of magnetite nanoparticles at 5 K 101

Figure 6.20 PAS-IR Absorbance spectrum for magnetite nanoparticles 101

Figure 6.21 EDS spectrum for magnetite nanoparticles 102

Figure 6.22	Powder XRD pattern for hematite nanoparticles	103
Figure 6.23	TEM micrograph of hematite nanoparticles	103
Figure 6.24	Temperature dependent magnetization of hematite nanoparticles	104
Figure 6.25	Hysteresis curve of hematite nanoparticles at 5 K	105
Figure 6.26	PAS-IR Absorbance spectrum for hematite nanoparticles	105
Figure 6.27	EDS spectrum for hematite nanoparticles	106
Figure 7.1	Structure of Arsenic Compounds	108
Figure 7.2	Acid-Base Dissociation Reactions of Arsenic Acid	109
Figure 7.3	Arsenic uptake by different phases of iron oxides and oxy-hydroxide.	116
Figure 7.4	EDS spectrum of goethite nanoparticles exposed to As	117
Figure 7.5	EDS spectrum of hematite nanoparticles exposed to As	117
Figure 7.6	EDS spectrum of maghemite nanoparticles exposed to As	118
Figure 7.7	EDS spectrum of magnetite nanoparticles exposed to As	118
Figure 7.8	PAS-IR of goethite nanoparticle pure and As exposed overlaid	119
Figure 7.9	PAS-IR of hematite nanoparticle pure and As exposed overlaid	120
Figure 7.10	PAS-IR of maghemite nanoparticle pure and As exposed overlaid	120
Figure 7.11	PAS-IR of magnetite nanoparticle pure and As exposed overlaid	121
Figure7.12	XPS survey scan of As exposed goethite particles	122
Figure7.13	XPS survey scan of As exposed hematite particles	122
Figure7.14	XPS survey scan of As exposed maghemite particles	123
Figure7.15	XPS survey scan of As exposed magnetite particles	123

Figure 7.16 Arsenic Removal as a Function of Nanoparticle Amount 124

Figure 7.17 Arsenic uptake with respect to the initial arsenic concentration for various sized maghemite nanoparticles 125

Figure 7.18 Arsenic uptake with respect to surface to volume ratio for maghemite nanoparticles 126

Figure 7.19 Arsenite adsorption on maghemite nanoparticles fitted by Freundlich isotherm 127

Figure 7.20 Arsenic uptake by particles regenerated with different concentration base solutions 129

Figure 7.21 Arsenic uptake with respect to recycle number for maghemite adsorbent 130

Figure 7.22 XRD pattern for core-shell nanoparticles 131

Figure 7.23 Arsenic uptake with respect to the initial arsenic concentration for core-shell nanoparticles 132

Figure 8.1 PAS-IR of goethite nanoparticle pure and Cr exposed overlaid 139

Figure 8.2 PAS-IR of goethite nanoparticle pure and As exposed overlaid 139

Figure 8.3 PAS-IR of hematite nanoparticle pure and Cr exposed overlaid 140

Figure 8.4 PAS-IR of hematite nanoparticle pure and As exposed overlaid 140

Figure 8.5 PAS-IR of maghemite nanoparticle pure and Cr exposed overlaid 141

Figure 8.6 PAS-IR of maghemite nanoparticle pure and As exposed overlaid 141

Figure 8.7 PAS-IR of magnetite nanoparticle pure and Cr exposed overlaid 142

Figure 8.8 PAS-IR of magnetite nanoparticle pure and As exposed overlaid 142

Figure 8.9 XPS survey scan of Cr exposed goethite particles 143

Figure 8.10 XPS survey scan of As exposed goethite particles 143

Figure 8.11 XPS survey scan of As exposed hematite particles 144

Figure 8.12 XPS survey scan of Cr exposed maghemite particles 144

Figure 8.13 XPS survey scan of As exposed maghemite particles 145

Figure 8.14 XPS survey scan of Cr exposed magnetite particles 145

Figure 8.15 XPS survey scan of As exposed magnetite particles 146

Figure 8.16 Arsenic and chromium uptake with respect to the initial arsenic concentration for various sized maghemite nanoparticles 147

Figure 8.17 Arsenic and chromium uptake with respect to surface to volume ratio for maghemite nanoparticles 147

Figure 8.18 Arsenic and Chromium uptake with respect to recycle number for maghemite adsorbent 149

SUMMARY

For the past few decades research and publications on nanomaterials has grown substantially. The majority of this research is devoted to the comprehension of physical phenomena appearing in fine particle systems. This deviation from bulk properties allows for the reconsideration of the commercial viability of many materials previously deemed inappropriate for industrial applications.

This nanorevolution has been promoted by the development of analytical measuring techniques that allow for the characterization of nanoparticles. With in-depth characterization available, research has begun to focus on tuning the properties for desired physical effects. Focusing on property control through chemical manipulation requires a high quality, reproducible synthesis method that allows for comparisons between batches. Finally, once tunability is obtained, the synthesis and materials must be scalable to successfully integrate into the commercial market.

New synthesis methods are routinely reported in the literature. Methods vary from novel schemes to minor adjustments to existing procedures that allow for a new product or feature. When evaluating these methods, commercial viability should be the benchmark to determine the best procedure. With the ability to tailor magnetic nanoparticle properties, the number of possible commercial applications is almost endless, making it essential to find a reaction scheme that is scalable to industry standards.

In this thesis, the commercial viability of the aminolytic synthesis method is explored through robustness, versatility, and waste reduction studies. Since the

development of a versatile, inexpensive, environmentally compatible, and large scale synthesis method for spinel ferrites nanoparticles has been pursued for years, we report the preparation of simplistic metal precursors and the development of a synthetic approach that could be used to prepare a variety of pure and doped spinel ferrites via the aminolytic reaction of metal carboxylates in a mixture of oleylamine and non-coordinating solvent. The magnetic properties of the nanoparticles are studied by a variety of analytical techniques; these properties also show the effect of surface anisotropy for less than 10 nm particles. In turn, the aminolytic reaction is proven to be an inexpensive and versatile synthetic route for manganese ferrites and can be extended to the rest of the spinel ferrite family.

With a consideration towards potential applications, the reaction is tested with a variety of dopants in an effort to correlate atomic arrangements with physical properties. Magnetic nanoparticles are being increasingly incorporated into sensing technology. Magnetostrictive properties of oxide materials are particularly useful in sensing changes in operating systems due to their good response and chemical robustness. The magnetic properties and responses of the spinel ferrites system are greatly influenced by quantum couplings of the magnetic ions. Thus understanding the couplings between these ions allows for manipulation of the desired magnetic properties. Manganese doping in the cobalt ferrite systems allows for the investigation of the effects of orbital momentum quantum coupling by exchanging a metal ion with high orbital momentum contribution, Co^{2+}, with a metal ion with no orbital momentum contribution, Mn^{2+}. To fully investigate these quantum coupling effects, all the compositions in the series $Co_{1-x}Mn_xFe_2O_4$, where x= 0.0, 0.1, 0.2, 0.3, 0.4, 0.5, 0.6, 0.7, 0.8, 0.9, and 1.0 were synthesized via the aminolytic reaction. The manganese metal ion prefers to occupy the tetrahedral (A) sites in spinel ferrites before it fills the octahedral (B) sites. This preference explains the jag in magnetic data between 40 and 50 % doping when mixed occupancy starts to occur. The coercivity decreases with increasing Mn^{2+} concentration due to the continued swapping of high magnetic anisotropy ion (Co^{2+}) with a low magnetic anisotropy ion (Mn^{2+}). To our knowledge, this work is the first full composition series of $Co_{1-x}Mn_xFe_2O_4$ reported.

The last test of the versatile and robustness of the aminolytic methods is the synthesis of a series of manganese ferrites dope with chromium. These ferrites show increasing magnetic frustrated responses. This doping allows for the investigation of the effects of orbital momentum quantum coupling by exchanging a metal ion with high orbital momentum contribution, Fe^{3+}, with a metal ion with no orbital momentum contribution, Cr^{3+}. All the compositions in the series $MnFe_{2-x}Cr_xO_4$, where x= 0.0, 0.05, 0.13, 0.25, 0.43, 0.62, and 0.85, were synthesized via the In-situ aminolytic method. This reaction uses metal salts and sodium propionate as the precursors. Oleylamine is a reactant, solvent, and stabilizing agent in this method. Though manganese ferrite is a mixed system $[Fe^{3+}_{0.67}Mn^{2+}_{0.33}][Mn^{2+}_{0.67}Fe^{3+}_{1.33}]O_4$, chromium ions preferentially occupy the octahedral (B) sites. Low chromium concentrations strengthen the L-S couplings due to the unquenched angular orbital momentum. High chromium concentration weakens the couplings between the A and B sites which results in the decreasing in the overall magnetic moment by destroying the magnetic arrangement. Chromium coupling on similar sites is very strong and at x=1 result in a disorder state. At higher concentrations, x=2, magnetic spins start canting resulting from the loss of antiparallel alignment that defines the spinel ferrite magnetic system. In our series at the highest doping concentration, there is a dramatic shift in magnetic properties.

Since magnetic nanoparticles have increasingly shown potential in a variety of applications including catalysis support, biotechnology, and high-density data storage, it is necessary to investigate waste reduction procedures. We have developed an aminolytic synthesis for the production of magnetic spinel ferrite nanoparticles. This procedure has the potential to be scaled up to an industrial level. The aminolytic reaction utilizes metal acetate and oleylamine reagents in a dibenzyl ether solvent. In fulfillment of green chemistry principles, all by-products can be recycled for re-utilization. Furthermore, the "mother" solution can be continuously used for multiple batches without treatment. Our trials have shown that the reaction could undergo ten reactions using the same solution without scarifying the quality or yield of the nanoparticulate product.

Finally, one environmental conscious application, desalination, is explored in this thesis through the use of aminolytic particles, iron oxides. In 2001 the Environmental Protection Agency (EPA) lowered the maximum level of contaminant (MCL) of arsenic in current water system. Studies indicate that up 10% of US municipal systems will have to be revamped to meet these increased standards. Iron oxides and iron oxy-hydroxides show a high affinity for arsenic in aqueous media. There are many forms of iron oxides and most of these structures are used in arsenic removal techniques. The iron oxide is formed in-situ by adding a non-oxide iron source to water. The exact nature of the arsenic binding and the effect of impurities on binding efficiency are not well known. Synthesizing well characterized iron oxides will afford better understanding of the arsenic surface binding. Better understanding of the binding affinity for arsenic is necessary for the incorporation of iron oxides into the best available technologies (BATs). Several nanometer sized samples of goethite (α-FeO(OH)), maghemite (γ-Fe_2O_3), magnetite (Fe_3O_4), and hematite (α-Fe_2O_3) were synthesized and characterized using XRD, SQUID, PAS-IR, EDS, and TEM.

Since there is an increasing interest in the removal of arsenic from water through the utilization of iron's affinity for arsenic oxo-anions, nano-size iron oxides including goethite, maghemite, magnetite and hematite have been synthesized and characterized systematically. These nanoparticles were exposed to arsenic solutions to measure the percent uptake of arsenic by each phase of iron oxides. All show that the arsenic oxo-acid is chemically bound to the surface. Adsorption isotherms were plotted for various sized maghemite nanoparticles to obtain Freundlich parameters. The adsorption constant (K) averages over a 400% increase; the parameter (n) is above one indicating favorable adsorption.

Our research, along with most of the literature, indicates that the hematite phase has the highest arsenic removal affinity of the iron oxide adsorbent class. In trying to harness this adsorption potential merged with the magnetic control seen in spinel ferrites, we have synthesized core-shell Iron Oxides@Cobalt Ferrites. This was done via the aminolytic method using a previously synthesized $CoFe_2O_4$ core which was reacted with iron oxide. Both samples, hematite and maghemite core-shell particles, were exposed to various concentration of arsenite and maghemite core-shell particles were found to have the higher removal affinity. This results from the difference in size between the core-shell nanoparticles with the maghemite derivative being 8 nm and the hematite derivative, 20 nm.

Also, the removal of oxo-anion containments, besides arsenic, from water through the utilization of iron's affinity for oxo-acids has become a research focus. Using the nano-size iron oxides and oxy-hyrdoxide that have been synthesized and characterized systematically, we will test the removal affinity for two oxo-anions. These nanoparticles were exposed to arsenate (As^{5+}) and chromate (Cr^{6+}) solutions to measure the percent uptake of containment by each phase of iron oxides. All the utilized analyzation techniques show that the oxo-acid is chemically bound to the surface.

In conclusion, this thesis will present the results of the versatility and robustness of the aminolytic synthesis through the synthesis of spinel ferrites, doped and pure. To improve the methods commercial viability, a waste reduction study was successfully completed. This allows the system's solvent to be re-used through multiple batches without degradation of the product. Finally, an environmental conscious application is explored through the use of iron oxide particles synthesized via the aminolytic method.

CHAPTER 1

INTRODUCTION

1.1 Applications of Magnetic Nanoparticles

For the past few decades research and publications on nanomaterials has grown substantially. The majority of this research is devoted to the comprehension of physical phenomena appearing in fine particle systems. This deviation from bulk properties allows for the reconsideration of the commercial viability of many materials previously deemed inappropriate for industrial applications[1]. These unique nanoscale physical properties have been known since Roman times with the Lycurgus cup[2] and continue to find use today.

This nanorevolution has been promoted by the development of analytical measuring techniques that allow for the characterization of nanoparticles. With in-depth characterization available, research has begun to focus on tuning the properties for desired physical effects. This is demonstrated most dramatically in the color range that is produced by different size CdSe quantum dots[3]. Focusing on property control through chemical manipulation requires a high quality, reproducible synthesis method that allows for comparisons between batches. Finally, once tunability is obtained, the synthesis and materials must be scalable to successfully integrate into the commercial market.

In this thesis, the commercial viability of the aminolytic synthesis method is explored through robustness, versatility, and waste reduction studies. With a consideration towards potential applications, the reaction is tested with a variety of dopants in an effort to correlate atomic arrangements with physical properties. Finally, one environmental conscious application, desalination, is explored through the use of aminolytic particles, iron oxides.

1.1.1 Sensors

Several properties of magnetic materials make them appropriate for sensor applications. The first is coercive field dependence on surface chemistry. Depending on the surface environment, the hysteresis loop of the nanoparticle can change by as much as 50%[4]. The second property is magnetostriction phenomena. For this phenomenon, the application of stress to the material will produce a change in magnetization; inversely, changing the magnetic field will induce a dimensional change in the material[5].

Using the magnetic response as an environmental sensor takes advantage of the fundamental properties of magnetic nanoparticles. Since the size of the material is reduced, the fraction of atoms on the surface becomes very high. This causes the material to be very responsive to changes on the surface. This affect is propagated through the surface anisotropy of the nanoparticle which receives a multiplier effect for small particles. Previous studies have shown that substituting existing surfactant ligands with ligands of a higher crystal field splitting energy causes the greatest reduction in coercivity[4]. By exploring the effect of surface anisotropy on magnetic properties especially coercivity, better sensors can be designed for the detection of many gaseous agents.

Two general sensors that utilize the magnetostriction phenomena are linear-position sensors and liquid level sensors. Both use magnetically induced strain to sense changes in position. A movable magnet, attached to a component or floating in solution, interacts with magnetostrictive material to induce a change in dimension that is recorded and translated in physical movement of the monitored magnet[6]. Because none of the parts are in physical contact, the wear on the system is minimal, making the sensors lifetime quite long.

One of the limitations of magnetostrictive materials is the production of eddy-currents, which causes energy loss; however, since oxides have high electrical resistivity this concern is eliminated[5]. This property along with other properties has sparked interest in spinel ferrite magnetostriction materials. Ferrites, also, are very chemically and thermally stable allowing for incorporation into higher temperature and pressure applications required for the automotive industry[7]. Currently, most of the commercially viable materials are composed of rare-earth metals, making their product cost high[8]. Ferrites have the fundamental properties to become the next generation magnetostrictive materials for industrial applications.

1.1.2 Separations

Separation and purification are areas of chemistry where the superparamagnetism of spinel ferrites nanoparticles can have the largest effect. Superparamagnetism causes the single domain particle to have enormous response to an applied magnetic field. Therefore, another compound bound to the nanoparticle will be simple to manipulate or remove with the assistance of the particle. Two instances of this application finding commercial use are in cancer cell removal from the bloodstream and arsenic removal from the water system.

Cancer is one of most prevalent diseases affecting almost every person either directly or through a loved one. Treatments are constantly improving; one improvement is the ability to remove metastatic cancer cells from the bloodstream through functionalized cobalt ferrite nanoparticles. These ferrite nanoparticles are coated with a peptide sequence that corresponds to an over expressed surface coating of ovarian cancer cells. By performing magnetic dialysis on the patient's blood, the cancer cells can be fished out and the clean blood can be returned to the patient[9]. This is not a cure for the cancer but one step of mitigating the anguish caused by this disease.

Arsenic in the water system is global epidemic. Areas hardest hit are Bangladesh and West India but United States is not unaffected. Both the World Health Organization (WHO) and the Environmental Protection Agency (EPA) have recommended that arsenic content in drinking water not exceed 10 ppb. This will require the revamping of a percentage of the US water systems. Iron oxides have an affinity for arsenic demonstrated by the fact that most of the arsenic contamination comes from the weathering of iron minerals with high arsenic content[10]. By synthesizing nanosized iron oxides, arsenic can be removed from the water system in a large percentage per amount of adsorbent due to the surface to volume ratio and the superparamagnetism of the nanoparticles. In this thesis, the percent removal of different iron phases for different contaminants is presented.

1.2 Synthesis Methods for Magnetic Nanoparticles

New synthesis methods are routinely reported in the literature. Methods vary from novel schemes to minor adjustments to existing procedures that allow for a new product or feature. When evaluating these methods, commercial viability should be the benchmark to determine the best procedure. With the ability to tailor magnetic nanoparticle properties, the number of possible commercial applications is almost endless, making it essential to find a reaction scheme that is scalable to industry standards. To help sort through all the available methods, I propose the following checklist to determine the best candidates for commercial use.

1. Inexpensive
2. Simple Procedure
3. High Product Yield
4. Versatility and Robustness
5. High Quality Product
6. Low Waste Production

When going through each item on the checklist, certain criteria need to be considered. To use a simplistic business model, product cost can be thought of as a combination of production cost and profit. There is a fine line between making the most profit and pricing the item out of the market so keeping production cost low is a business imperative. Many factors contribute to product cost and several of these factors are address by the checklist.

Ways to make a synthesis method less inexpensive result from lowering the cost of the following: precursor, solvents, and purification. The best precursors are cheap and/or easy to synthesize precursors. The amount of solvent and surfactant used during synthesis should be minimized to reduce cost. Purification, often forgotten when calculating cost, can be adjusted by changes in the reaction scheme. These are the most direct costs to manufacturing chemical materials.

The simplicity of the reaction procedure affects production and thus cost in the following ways. Complicated methods required a skilled lab force and costly equipment. One way to reduce cost is to use a reaction scheme that is as simple as possible translating into less equipment and less cost. Also, by reducing the complexity of the procedure, businesses can lower the skill level needed by employees thus lowering the salary required.

Remembering that production cost is a ratio of expense to amount of product produced reveals another area of hidden cost. High product yield with the cheapest product is a recipe for business success.

The more robust and versatile the reaction scheme the more cost savings that will be realized later on. Materials production is driven by consumer demand. The ability to adjust the reaction to synthesize multiple materials or different compositions of the same material with minimal transition cost will give the investor an advantage over the competition.

Maintaining a consumer base is a constant concern of most businesses. If a product is cheap, people will buy it. However, if the product quality falls below expected standards, few customers will become repeat or loyal consumers of the products. Keeping product quality as high as possible without inversely affecting the pricing is another balancing act that businesses face.

Finally, in recent years environmental regulations and waste disposal procedures have added another layer of costs to materials manufacturing industry. The ratio of amount and type of waste created in relations to amount of materials produced is another area that can indirectly affect the company's bottom-line.

Using these provided standards to compare the commercial viability of published reaction schemes, a review of the recent literature can be performed with a greater focus on applicability of the method to an industrial setting. The next sections summarize a few synthesis methods that are currently in use today. The last reaction scheme presented is the aminolytic reaction method. This method was developed in the Zhang lab by a previous student, Dr. Man Han. Throughout this thesis, I will explore the aminolytic method's robustness and versatility for producing spinel ferrite magnetic nanoparticles. In a later chapter, a waste reduction and solvent longevity study is reported. Lastly, at the end of the thesis, research into an environmentally beneficial application of these particles will be presented.

1.2.1 Mechanical Milling Methods

Mechano-chemical synthesis or ball milling is a highly non-equilibrium top-down approach to synthesizing nanoparticles[11]. Nanoparticles are produced by grinding molecular precursors in a vial with grinding balls[12]. There are two main advantages to mechanical milling. First is the ability to produce large quantities of product in a fairly short timeframe. The second is the ease at which the methods can be operated. These factors have contributed to making the technique fit for industrial application. Also the generated thermal energy from the milling can facilitate chemical reactions including redox and formation reactions. For spinel ferrite synthesis, layered hydroxide compounds and metal oxides can be used as precursors as both have the benefit of facile synthesis and inexpensive reagent cost[13].

This method, however, produces nanomaterials with high polydispersity, unusual cation distribution or vacancies, and impurities. With the repeated fracture and re-welding of reagent powders, high defect densities are produced[14]. These issues greatly influence the magnetic properties of the sample, which can sometimes be 25-40% less than theoretical calculations, making reproducibility between batches near impossible[15].

Although most ball milling synthesis methods involve grinding of dry powder precursors, the use of surfactants and solvent is becoming more common to improve homogeneity and eliminate impurity formation[16]. Impurities can also be introduced to the product from the reaction vial or milling balls. Finally, extensive milling times are often required to produce particles less than 20 nm[14].

1.2.2 Combustion Methods

Self-propagating high-temperature synthesis (SHS) aka combustion synthesis is a low cost, high through-put method that is currently used on an industrial scale in at least sixty five countries[17]. This great interest arises from the simplicity of the method and cost effective processing[18]. The solution-combustion method which is favored for the production of nanosized powders contains two processes. First, the constituents of the precursor are intimately blended, and then the precursor is auto-ignited. Due to the exothermal nature of the synthesis method either a flame or fire is produced. The most important parameters surrounding the reaction are the fuel source properties as well as the miscibility and decomposition temperature of the precursors. The fuel should maintain compositional homogeneity of the precursors and have a low ignition temperature. Common examples of fuel sources used include glycine, citric acid, urea, and ascorbic acid. The heat of combustion of the reaction helps crystallize the precursor and form the desired phase[19].

Careful control of the above factors must be maintained or it will result in loss of size and dispersity control of the crystallites. Method refinement is needed to produce agglomeration free particles with a predictable morphology[17]. Though publications of magnetic nanoparticles synthesized via the combustion synthesis have been reported, it is difficult to correlate the chemical composition nanoparticles to magnetic properties due to differing size, polydispersity, and agglomerate characteristics[20]. Produced materials are also at the edge of single domain particle size adding the possibility of domain wall movement as a factor in magnetic response[21].

1.2.3 Sol-Gel Methods

Sol-gel methods or chemical solution deposition is a bottom-up synthesis utilizing a gel matrix to arrange, on a molecular level, mixing of stoichmetric precursors. The better control of the precursors allows for materials to be tailor made for their applications. This method is usually used for the fabrication of metal oxides with a solution (sol) of metal alkoxides and/or chlorides integrated into a gel of networked polymer or particles[22]. The precursors undergo hydrolysis or condensation and form small metal oxide particles. Once a sol-gel is created in the appropriate stoichmetric ratio, it is usually dried and then thermally treated which causes the fine particles to agglomerate or sinter forming the desired sized product[23]. This method is especially useful for coating nanomaterials on substrates and making fibers or composites as the product forms anywhere a sol-gel can be deposited and will mold to the shape of its container. As mentioned, the sol-gel synthesis is uncomplicated both in operation of the equipment and in changing out precursors to make varying chemical compositions. This allows for some adjustment of the materials' properties with chemical manipulation[22].

Unfortunately, irregular particle sizes and shapes are common due to variations in packing density of the sol-gels. If the solvent is not removed at the same rate throughout the gel then non-uniform shrinkage can occur. Issues caused during solvent removal are often amplified during the thermal treatment which leads to structural defects in the nanomaterials. Care also needs to be taken to match the hydrolysis rates of the precursors so that undesired crystalline phases are not produced[22]. Also the rates of hydrolysis are one parameter that controls particles size through the monodispersity and initial size of the fine metal oxide particles produced before the firing process[24]. If the precursors are not well matched, desired doping may not occur. This issue can complicate precursor synthesis and limit the versatility of the sol-gel reaction method. Another disadvantage that occurs is the inability to control side reactions which can lead to the contamination of materials with by-products[22].

1.2.4 Micelle Methods

Precipitation in microemulsion is a well-established bottom-up technique for preparing small sized nanoparticles (less than 10 nm)[12]. This use of an inorganic phase in water-in-oil micelles has received extensive attention. In some of these methods, two batches of micelles are produced each containing a reactant. When the mixtures of reactants are combined the micelles coalesce causing the reaction to take place and form the desired metal oxide precipitate. In other methods, a reducing agent is added to induce the formation of desired particles. In all cases the micelle is acts as a nanoreactor, resulting in a narrow particle size distribution which can be controlled by varying the solvent to surfactant ratio instead of thermal annealing[23]. Since the growth of the particles is relatively slow, nanoparticles produced have equilibrated cation distributions and little crystal lattice strain[25]. The particles produced by this method are ideal for studies on correlating magnetic properties with chemical composition[26]. These microemulsions also help prevent aggregation of the produced particles. After formation, sometimes the particles precipitate out of the micelles which can collected by centrifugation or an applied magnetic field.

One of the drawbacks is that sometimes heat treatment is needed to ensure high crystallinity. Another is the low yield, ~1 g, and large waste production. This is also an expensive synthesis method due to the large amount of surfactant needed for each reaction[14]. Finally, since the surfactant will also adsorb on to the particle surface, separation procedures are needed to clean the particles of organics.

1 .2.5 Thermal Decomposition Methods

Thermal decomposition of organometallic compounds has gained much attention recently. This method offers superior size control, crystallinity, and a narrow size distribution[12]. Recent developments have allowed for nanoparticle synthesis with tunable morphology[27]. In this method, a metal organic precursor is decomposed in a high boiling organic solvent in the presence of a surfactant.

The biggest drawback to this method is the precursors. If a single stoichmetric precursor is used, it is often synthetically challenging to make or expensive to purchase. The singe precursor also limits the reaction scheme to a single product. To change the chemical composition of the product, a new suitable precursor must be found and this can be a challenge. If multiple precursors are used, it is essential that the decomposition temperature of all precursors be similar or there will be incomplete incorporation of the metal ions. The use of multiple precursors allows the reaction to be used to produce a variety of nanomaterials as long as suitable precursors can be obtained. Examples of thermal decomposition precursors are metal carbonyls[28], metal acetylacetonates[27, 29], and metal carboxylates[27a]. In exchange for the superior quality of nanoparticles, only an extremely limited amount of product can be produced from this procedure[30]. Also, a relatively large quantity of high boiling, typical toxic solvent is generated as waste.

1 .2.6 Aminolytic Synthesis Method

The aminolytic synthesis developed by Dr. Man Han from the Zhang group is a version of the thermal decomposition route. Metal organic precursors are added to a high boiling point solvent in the presence of a surfactant. The improvement upon the thermal decomposition methods cited is uses precursors that are simple metal acetates. Metal acetates are easy to synthesize or purchase for a wide variety of metal ions in various oxidation states. This allows for diversity of the materials and compositions of the materials to be synthesized. The proposed mechanism for this reaction is also different than the usual thermal decomposition method[31]. Instead of decomposition temperature controlling nanoparticle synthesis, particles are produced through the formation of an amide bond between the acetate and amine of oleylamine, the surfactant; this is followed by a condensation reaction with the metal hydroxides to oxides. Because the formation of the amide bond is a relatively slow process, the formation of the nanoparticles is a slow, well control process using the limited and gradually produced supply of metal hydroxides. By being able to control the nucleation and growth process of this reaction scheme, the particles produced are of high quality, monodespersed and excellent size control. Also, oleylamine performs multiple functions as both reagent and surfactant; this dual lowers the number chemicals necessary for the reaction. Unreacted oleylamine is used to coat the metal oxide particle surface. This stabilizes the particles and prevents aggregation. This reaction method removes the issue of matching thermal decomposition temperature of the precursors but keeps the superior size control, crystallinity, and a narrow size distribution. The metal acetate precursors allow the synthesis to be used for a variety of materials.

1.3 Instrumentation and Characterization

1.3.1 Powder X-ray Diffraction

X-ray diffraction (XRD) is a useful structural characterization technique that has successfully transitioned from a bulk analysis method to nanoparticle characterization technique[32]. For the experiments in the following chapters three lab X-ray diffractometers, all with a Cu K_{α}, source were used. The Bruker D8 Advanced X-ray diffractometer was used for nanoparticle analysis where only a small amount of the sample was available. The PDW3050 X-ray diffractometer was used to complete the majority of the analysis for this thesis and finally the Scintag X1 X-ray diffractometer was used to obtain any patterns needed for Rietveld Analysis. XRD analysis is a straightforward, rapid and easy method for determining the crystalline phase of a sample[33]. By comparing the diffraction pattern obtained from the sample to the pattern reported in the International Centre for Diffraction Data's Powder Diffraction File (ICDD file number), the materials' lattice planes and corresponding crystalline structure can be elucidated[34]. Taking a XRD pattern is a nondestructive way of characterizing nanomaterials and a fast way to determine if more analysis is necessary or if the sample is unusable.

Since a crystal is a homogenous solid containing repeating patterns of atoms, powder diffraction gives distinctive peak positions and intensities in accordance to the atomic positions within the unit cell and corresponding lattice planes. X-ray diffraction patterns result from reflected X-rays's waves' interference. As the incident X-ray beam of fixed wavelength, 1.54 Å, comes in contact with the atoms in the crystal, the X-ray waves are reflected at certain angles. Due to the periodicity of the atoms in the crystal, these waves can interact constructively if the path length or the interplanar crystalline spacing, d, is an integer multiple of the wavelength[35]. This diffracted beam will have the same angle as an incident beam. This relationship is expressed as Bragg's Law

$$n\lambda = 2d\sin\Theta \qquad (1.3.1.1)$$

where n is an order of reflection, λ is the wavelength of the incident X-ray beam, d is the interplanar spacing of the crystal, and Θ is the angle of reflection or incidence[36]. This is also illustrated in Figure 1.1.

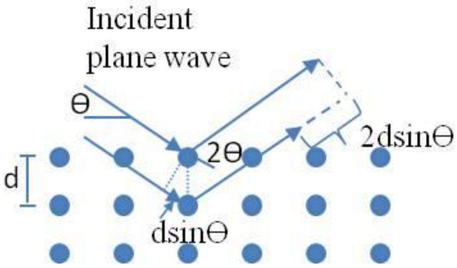

Figure 1.1. Diagram of Bragg's diffraction.

The diffracted beam intensity is detected and plotted against the corresponding 2Θ diffraction angle to obtain the diffraction pattern.

Due to the finite number of lattice planes that limit destructive and constructive interference, the peaks in XRD patterns of nanomaterials broaden. These XRD patterns can also be used to determine the average crystalline size which corresponds to the average nanoparticle size. With this lack of cancellation, the patterns are not as sharp as they would be if obtained from analogous bulk materials. Using a simple treatment, the average nanoparticle size can be determined from the broadening of XRD pattern. According to the Scherrer's equation[37]

$$D = K\lambda/(\beta\cos\Theta) \qquad (1.3.1.2)$$

where D is the average nanoparticle size, λ is the X-ray wavelength, Θ is the Bragg angle, and β is the finite size broadening, and K is a constant usually 0.9 or 0.94 that relates nanoparticle shape and the broadening calculation methods (in this case the full width at half-height maximum intensity, FWHM). This approximation of the average nanoparticles' size only works well when there is a single homogenous phase and a narrow size distribution. Most nanoparticle sizes reported in this thesis will be the result of line broadening analysis from XRD patterns.

1.3.2 Transmission Electron Microscopy

Another useful characterization tool for materials is Transmission Electron Microscopy or TEM. The development of this instrumentation revolutionized small molecule and nanomaterial research by allowing scientist to finally see the materials they were working with on the nanoscale. By breaking the boundaries created by visible light by using a beam of electrons, it is possible to clearly make out samples as small as a nanometer. Even though XRD patterns can supply average size and crystal structure, TEM allows for individual visualization of the nanoparticles. This allows for size and morphology studies as well as size distribution determination throughout a sample[38]. The TEM studies were performed on a JOEL 100CX or a Hitachi TEM HF2000 at the Center of Nanostructure Characterization, Georgia Institute of Technology. Sample preparation often is time consuming because an evenly dispersed film of nanoparticles is challenging to produce. Another consideration is that the electron beam interacts with the electrons in the specimen. For magnetic materials, this interaction can often cause the nanoparticles to move or vibrate making it difficult to obtain clear micrographs.

Chemical analysis can also be confirmed using an energy dispersive X-ray spectroscopy (EDS) analyzer that the Hitachi TEM has equipped. For EDS analysis, X-rays are emitted from the material due to the filling of an electron hole with another electron from a higher energy level. This hole is created by exciting a ground state electron with the focusing of the high energy electron beam. These X-rays are detected and plotted as a function of count and photon energy. Each element has unique characteristic photoemission energies due to atomic structure; elemental chemical composition of the sample can thus be obtained[38b].

1.3.3 SQUID Magnetometry

Superconducting Quantum Inference Device (SQUID) magnetometry is one of the most sensitive instruments with the ability to measure changes in magnetic response up to 10^{-11}G. . All magnetic measurement presented in this thesis were performed on a Quantum Design MPMS-5S instrument. A DC SQUID is composed of a closed superconducting loop that is cooled by liquid Helium and two Josephson junctions in the loop's current path. Josephson junctions are electronic structures made of two superconductors which are separate by a thin insulating barrier. Electrons move through the insulating barrier creating a Josephson current. When thermal fluctuations are kept at a minimum, near absolute zero, the Coulombic repulsion of electrons is overcome allowing two electrons to form Cooper pairs. These pairs have a spin quantum number of zero due to spin cancellation. By pairing and avoiding the Pauli Exclusion Principle, the produced Cooper pairs to be can described by wavefunction. A current is measured across the insulating barrier with the magnitude of the current proportional to the phase difference of these wavefunctions[39]. This current production across the junction is known as the Josephson effect[40]. These junctions oscillate at high speeds when maintained at temperatures near absolute zero.

To record the magnetic moment in a SQUID magnetometer, the changing current resulting from the magnetic field produced by the sample is measured. This output voltage is directly proportional to the current generated by the moving sample. Since the system is closed and cooled to near absolute zero, an extremely accurate measurement is obtained.

Powder samples are weighed out and recorded to the nearest tenth of a milligram. The sample is then transferred to a 0.5 mm by 1.5 mm gelatin capsule. Samples are immobilized by eicosane if hysteresis measurements are going to be performed. The sample capsule is then sealed with Kapton tape and inserted in a plastic straw. It is important that all materials used do not produce a magnetic response. The sample container is then taped to the end of the sample rod and inserted into the sample chamber. Both the sample chamber and space are under vacuum to prevent ice blocks from forming because atmospheric gases freeze at the low temperatures (~5K). The sample is then lowered into the sample space where the magnetic measurements will occur.

There are two routinely used types of SQUID measurements[41]. One measurement records the magnetic response of material over a broad temperature range. This is called a Magnetic Susceptibility, χ, measurement and generates a table of magnetic responses with respect to applied temperature at a constant applied field, H. Magnetic Susceptibility is the magnetization, M, of the material divided by the magnetic field, M/H, and usually is reported in units of emu/gG. For nanoparticles, it is customary to report weight susceptibility, divided by the mass of the sample, instead of molar susceptibility, divided by the molar mass, because it has more relevance to the system. The second commonly used measurement is the Magnetic Hysteresis. Here, the magnetic responses are recorded with respect to applied magnetic field at a constant temperature. The magnetic fields in this experiment are quite high usually going up to 5 T field. The temperature is usually held at 5 K but the experiment can also be performed at room temperature or 300 K. When the values are plotted, magnetic saturation, remnant magnetization, and coercivity can be determined. Magnetic responses are given in units of emu/g and the coercivity field in units of Oe or G.

A typical curve produced from the magnetic susceptibility measurements is shown in Figure 1.2. The maximum magnetization exhibited by the nanoparticle system occurs at a specific temperature known as the blocking temperature, T_B. T_B is the point when nanoparticles start exhibiting superparamagnetic behavior.

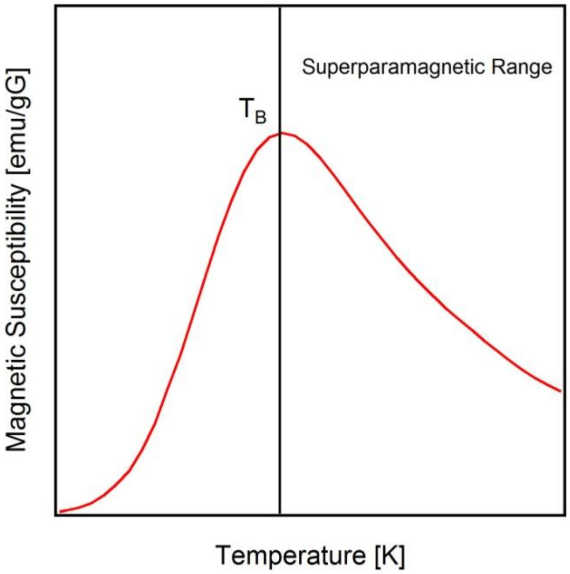

Figure1.2. A typical magnetic susceptibility curve.

Figure 1.3 is the hysteresis loop produced by plotting the magnetization as a function of applied field. Magnetic saturation, M_S, is the maximum value of magnetization achieved labeled (a) on figure. As the applied field is reduced the spins in the systems return to equilibrium and cease to be aligned so the total magnetization decreases. When there is no applied field, the magnetic response is due to the magnetic memory of the material or remnant magnetization, M_R, labeled (b) on the figure. To remove the magnetization of the sample a negative field needs to be applied. Labeled (c) on the figure, the magnitude of this field is called the coercive field, H_C. Studying the changes in magnetic properties with respect to fields and temperatures allow for better understanding of the nanoparticle system and the effects of chemical manipulation.

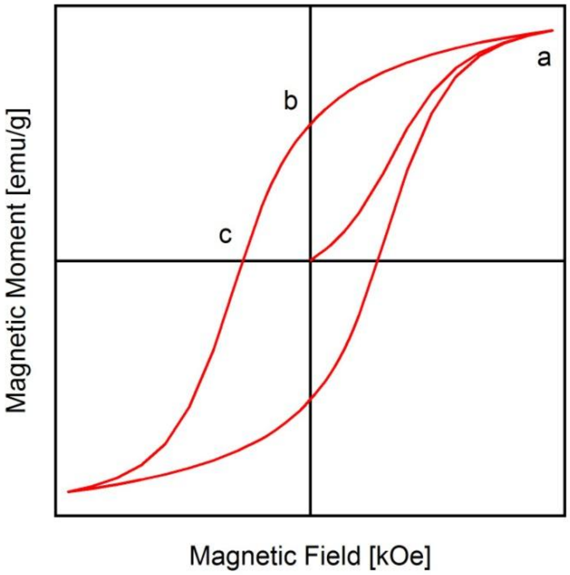

Figure1.3. A typical magnetic hysteresis loop.

1.3.4 Inductively Coupled Plasma Optical Emission Spectroscopy

Inductively Coupled Plasma Optical Emission Spectroscopy (ICP-OES) is a spectrophotometric technique used for the detection of metals down to trace amounts. Atoms or ions are excited by the inductively coupled plasma so that they emit different wavelengths of light due to the characteristic electron relaxation that is individual to each element. Since the plasma electrodes are located outside the reaction chamber, there is limited contamination. The intensity is used to quantify the elemental concentration in the specimen. However, care needs to be taken in sample preparation to make sure the desired elemental analysis will not spectrally interfere and create inconclusive results[32b]. Since samples must be in solution phase, nanoparticles are digested in nitric acid solution under high temperature and pressure provided by a parabomb reactor. For water bound containment analysis, detection limits also need to be considered to accurately interpret the results. The detection limits for arsenic and chromium are 113 ppb and 5.6 ppb respectively. All ICP-OES analysis performed for this thesis were done at Georgia Institute of Technology Chemical Analysis lab on a Perkin Elmer Inductively Coupled Plasma Optical Emission Spectrometer (ICP), OPTIMA 7300DV.

1.3.5 Photoacoustic Infrared Spectroscopy

A useful alternative to Fourier Transform Infrared Spectroscopy (FTIR) is Photoacoustic Infrared Spectroscopy (PAS-IR) which allows for a surface analysis instead of bulk analysis. PAS-IR is also a nondestructive analytical technique making it very useful for small sample amounts. PAS-IR differs from traditional IR because it uses a microphone to detect acoustic waves that results from the absorption of IR radiation by a sample (gas, liquid, or solid). Due to the sensitivity of the technique, PAS-IR is widely used for detection of trace contamination, such as arsenic and chromium under the scope of this work[42]. PAS-IR only probes the surface a few micrometers because the absorption is limited by the thermal diffusion of the material. To measure the spectra, powder samples are transferred to an aluminum cap. The sample cap is then placed in the sample chamber where it is purged at different degrees with compressed He, the carrier gas. Modulated infrared light is transmitted through the cell and absorbed by the sample material. The absorbed radiation is then converted into heat through radiationless processes. The heat is transferred to the immediate surrounding area resulting in a pressure wave. Pressure variations as a function of wavelength are recorded using a sensitive microphone and then used to produce a photo-acoustic spectrum of percent absorbance vs. wavenumber (cm^{-1})[32b]. This spectrum is similar to optical absorption spectrum[43]. For this thesis, all photoacoustic infrared spectra were obtained on a Biorad FTS-6000 Fourier transform infrared (FTIR) spectrometer with a MTEC model 300 photoacoustic (PAS) detector.

1.3.6 X-ray Photoelectron Spectroscopy

X-ray Photoelectron Spectroscopy (XPS) is a sensitive spectroscopic surface analysis technique, but unlike the other chemical analysis tools used, it is also provides information about the structure and oxidation state of specimen examined as well as qualitative and quantitative elemental composition. It is a core-level photoelectron surface specific method with penetration depths up to 10 nm, but in the case of nanoparticles with their small footprint, these scans can often give the spectrum of an entire particle. The sample surface is irradiated with a monochromatic X-ray beam causing electrons to be displaced from the inner shells of an atom. The kinetic energy of the emitted electron (E_k) is measured and then used to calculate the binding energy (E_b) in conjugation with the work function (w) of the spectrometer through the following equation

$$E_b = h\upsilon - E_k - w \qquad (1.3.6.1)$$

where $h\upsilon$ is the energy of monochromatic x-ray photons[32b]. The kinetic energy along with the number of electrons produces the XPS spectrum. However, to avoid contamination of the sample surface by oxygen or water, the measurements must be performed under ultra high vacuum (UHV) conditions which increases sample preparation. To help with out gassing from the sample and to maintain appropriate sample chamber pressure, all powder samples analyzed where placed in a vacuum oven overnight to remove adsorbed water or atmospheric gasses. A survey scan was performed on all samples to determine the elemental composition. All peaks in the spectrum should be identifiable. One element can be attributed to several peaks due to multiple inner electrons being ejected and Auger processes. Elemental scans were performed for contaminants of interest such as arsenic and chromium to determine their quantity and chemical binding state. Care needs to be taken to adjust for the charge shift as the magnetic material will accumulate charge even in the presence of the ion flood gun usually used to cancel out this effect. Elemental carbon on the sample holder has a known binding energy and can be used as an internal standard to correct for the charge accumulation shift[32a].

1.4 Spinel Ferrites

1.4.1 Unit Cell and Crystal Structure

Spinel ferrites are a class of materials that have the general spinel structure with the trivalent metal ion being iron. The general spinel structure is an FCC array of oxygen atoms creating both octahedral and tetrahedral cationic coordination sites. There are 64 tetrahedral interstitial sites but only eight are occupied. For octahedral interstitial sites, 32 are created and 16 are filled. As shown in Figure 1.4[44], spinel ferrites have the characteristic structure of $A(II)B(III)_2O_4$ with A being the tetrahedral cation site and B being the octahedral cation site usually occupied by Fe(III)[45].

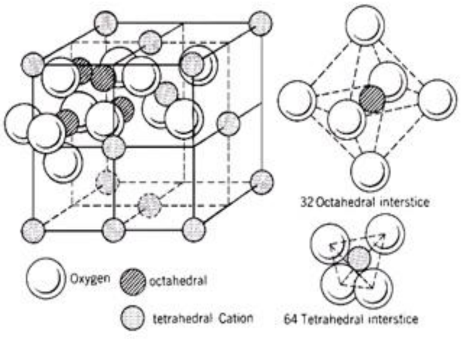

Figure 1.4. Spinel Ferrite Structure

There are several cationic arrangements possible with the spinel ferrite system. If the divalent metal ion is restricted to the tetrahedral site as well as trivalent iron ion residing in the octahedral site, then the spinel is normal. When the A sites are completely occupied by Fe(III) and the B sites are randomly occupied by M(II) and Fe(III) cations, this structure is inverse spinel, B(AB)O_4. Spinel Ferrites synthesized with wet chemistry methods are usually a mixed spinel where both cations are distributed across the octahedral and tetrahedral sites.

1.4.2 Magnetic Arrangement and Properties

1.4.2.1 Magnetic Arrangement

Spinel ferrites have antiferromagnetic ordering that arise from the alignment of the metal cation sites. The magnetic moments of the tetrahedral sites (A) are aligned in a parallel relationship. The octahedral sites (B) are also aligned parallel to other octahedral sites. However, the magnetic moments of octahedral and tetrahedral sites are aligned antiparallel in the structure (Figure 1.5).

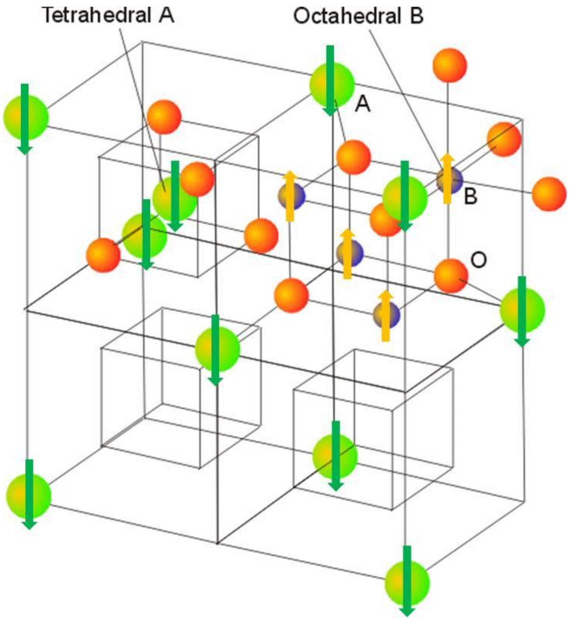

Figure 1.5. Magnetic spinel ferrite structure adapted from Shriver[46].

Ferrimagnetic behavior is exhibited for these spinels because the strengths of the magnetic moments do not cancelled each other complete. A diagram of this behavior in the cobalt ferrite system is shown below (Figure 1.6).

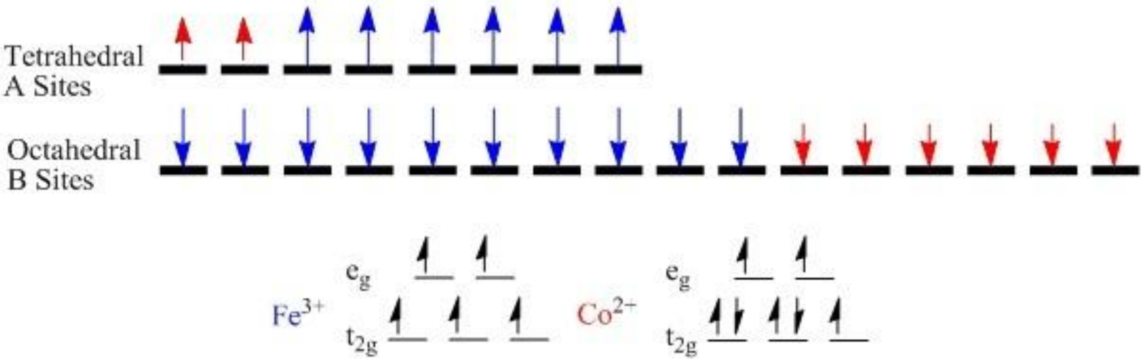

Figure 1.6. Unequal antiparallel alignment of magnetic moments in cobalt ferrite.

As illustrated above, the magnitude of the magnetic moments from the A sites do not completely eliminate the magnetic moments from the B sites resulting in an overall magnetic response.

1.4.2.2 Single Domain Particles

One fundamental difference between bulk and nanosized magnetic materials is the presence of magnetic domain where in a domain groups of moments are orientated in the same direction. Separating these domains are "walls" which helps minimized magnetostatic energy. In bulk materials, magnetization is a function of domain wall movement and formation. However, below a critical size scale, domain wall formation is not energically favored and single domain particles are produced[47]. At this point, magnetization can result from the following: coherent rotation of spins or curling. When magnetized, there is a preferred orientation direction called the easy axis. This crystallographic direction is determined by the magnetocrystalline anisotropy (K) of the material and is independent of shape[48]. Since domain walls shift with relatively weak applied fields, single domain particles are harder magnetic materials than their bulk counterparts resulting in larger values for magnetization and coercivity[47]. This intriguing difference makes magnetic nanoparticles applicable where bulk magnetic materials may not appropriate. All nanoparticles in this thesis are single domain particles.

1.4.2.3 Superparamagnetism

The magnetic vector of a nanoparticle overcomes the energy barrier separating positive and negative states (Figure 1.7) at the rate given by a Néel equation[49]

$$\tau = \tau_0 \exp(E_A/k_B T) \qquad (1.4.2.3.1)$$

where τ is the rate of reversal, τ_0 is the frequency that the magnetization vector attempts to flip, E_A is the energy barrier, k_B is the Boltzmann constant, and T is temperature. If the time frame of the measurement is shorter than the reversal rate then the magnetic moment of the material is considered blocked meaning the relaxations do not occur over the observed time period. At longer time frames, there is a rapid fluctuation of magnetic moments[50]. The blocking temperature is the point where the thermal energy is sufficient for the particular volume such that the magnetic moments are not blocked by the energy barrier[51]. Above this temperature, the particle exhibits superparamagnetic behavior. Superparamagnetism is the formation of a "superspin" with a gigantic magnetic moment per particle[52].

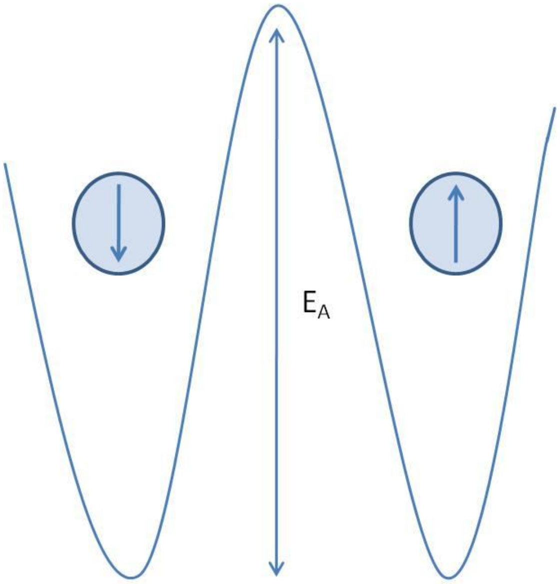

Figure 1.7. Potential well schematic of anisotropy energy barrier for magnetic reversal.

1.4.2.4 Magnetic Anisotropy

The magnetic anisotropy contribution is composed of several parts[53]. The first component is the magnetocystalline (bulk) anisotropy which is due to the spin-orbtial couplings of the magnetic moments in the crystal lattice. This anisotropy term determines the orientation of magnetization in the material. The easy axis is the crystallographic direction that produces the lowest magnetocrystalline anisotropy energy[54]. Since this property is intrinsic to the material, any hysteresis taken will be affected by its strength. In hard magnetic materials, the magnetocrystalline energy is large; in soft materials, small.

Next, shape anisotropy is an extrinsic property that is not found in spherical particles[55]. As all magnetic investigations in this thesis were performed on spherical particles, this contribution can be neglected.

Finally, surface anisotropy is an important consideration for small particles as surface effects become more prominent with smaller volume. The concept of surface anisotropy was first proposed by Néel[56]. He speculated that the reduction in coordination and lower symmetry of the surface atoms will increase the overall anisotropy. Also, atomic disorders on the surface can induce local fields whose easy axis are perpendicular to the surface[57]. Because of these three factors, symmetry, coordination, and local strains, moments on the surface often will not be aligned with the core moments of the particle[58].

To calculate the total magnetic anisotropy, the following equation[59] can be used to include the surface effects

$$K = K_{xtal} + (6/d)K_s \qquad (1.4.2.4.1)$$

where K is magnetic anisotropy, K_{xtal} is the magnetocrystalline anisotropy, d is the diameter of the particle, and K_s is the surface anisotropy. Since surface anisotropy increases the overall magnetic anisotropy, it makes the material magnetically harder.

When tailoring magnetic properties to synthesize the best materials for an application it is essential to consider all the anisotropy contributions. As smaller and smaller materials are needed, the surface contribution to magnetic anisotropy calculation becomes has a more prevalent effect on the magnetic properties. Thus, surface anisotropy needs to be directly manipulated instead of being a by-product of nanoparticle utilization to create the most appropriate materials.

1.4.3 Couplings and their effect on magnetic response

Magnetic properties of materials can be described and controlled through magnetic coupling; these couplings are influence by the chemical composition and structure of materials. Magnetic nanoparticles have a single magnetic domain structure if the particle size is less than 20 nm. As a result, atomic level magnetic couplings can be directly correlated with the observed magnetic properties. Some of these exchange couplings for the spinel system are between different types of sites, $J_{A\text{-}B}$, and the same types of sites, $J_{A\text{-}A}$ and $J_{B\text{-}B}$. These exchange interactions determine the magnetic ordering of the material. A positive exchange coupling will result in a parallel alignment of the ions' magnetic moments while a negative coupling leads to an antiparallel arrangement.

Though there are several types of exchange couplings, magnetic ordering in spinel ferrites arises due to superexchange couplings. For superexchange couplings, the magnetic moments are too far apart to interact directly. Instead, the non-magnetic ion, oxygen, directs the coupling. This causes J to become dependent on the symmetry and the orbital arrangement. With this in mind, orbital angular momentum and symmetry become extremely important when trying to elucidate magnetic behavior and tailor materials. For ferrites, A-O-B has the largest degree of orbital overlap considering a bond angle of 125˚ and the orbital geometry. This causes the $J_{A\text{-}B}$ to be the dominate coupling. Next, is the coupling between B-O-B with a bond angle of 90˚. Lastly, is the $J_{A\text{-}A}$ coupling, the weakest, due to the small bond angle of 79˚ and the atomic separation of approximately 4 Å[60]. In short, couplings between different types of sites, octahedral and tetrahedral, are usually stronger than the coupling between the same type of sites.

When an octahedral favoring cation is doped in, Fe^{3+} concentration in octahedral sites will decrease. This allows for examination of the $J_{A\text{-}B}$ coupling between Fe and the metal dopant by making a series of different compositions samples. Another aspect that affects the magnetic properties that should be considered is a different type coupling between the electron spin (S) and the angular momentum of the orbital (L) seen in Figure 1.8[61].

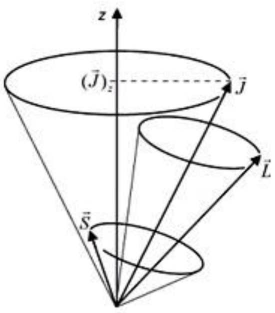

Figure 1.8. Coupling vectors in spinel ferrite system.

Orbital angular momentum is a special consideration when trying to manipulate magnetic properties. When exchanging Fe^{3+} in the octahedral site for Cr^{3+}, there is an increase in orbital angular momentum. Even though the Cr^{3+} ion has an electron configuration of $t_{2g}^3e_g^0$, it has a relatively large orbital angular momentum[62]. This occurs through the distortion of the polyhedron to create more degenerate orbital states allowing the electrons more mobility[63]. Fe^{3+} has no orbital angular momentum contribution because with a $t_{2g}^3e_g^2$ the electrons are fixed in their respective orbitals. By doping in chromium for the octahedral iron, the orbital angular momentum contribution to the magnetic properties can be investigated.

By doping in with a cation that contributes a different angular orbital momentum, the effects of changing L as well as S can be studied. Spin-orbital couplings determine the magnetic orientation of a material. Although Russell-Saunders coupling (L-S) is the most important aspect of the magnetic properties for 3d transition metals, the JJ couplings can play a major role in spinel structures[45]. In designing magnetic materials, it is important to determine the effect of these JJ couplings as well L-S interactions in 3d metal ferrites for exact control of magnetic properties at the atomic level.

CHAPTER 2

FACILE SYNTHESIS OF MONODISPERSED MANGANESE FERRITE NANOPARTICLES VIA AMINOLYTIC REACTION IN NON-AQUEOUS MEDIUM

2.1 Abstract

Development of a versatile, inexpensive, environmentally compatible, and large scale synthesis method for spinel ferrites nanoparticles has been pursued for years. In this chapter, the preparation of simplistic metal precursors and the development of a synthetic approach that could be used to prepare a variety of pure and doped spinel ferrites via the aminolytic reaction of metal carboxylates in a mixture of oleylamine and non-coordinating solvent are reported. The magnetic properties of the nanoparticles are studied by a variety of analytical techniques; these properties also show the effect of surface anisotropy for less than 10 nm particles. These effects are consistent with theoretical predictions and published results[25]. In turn, the aminolytic reaction is proven to be an inexpensive and versatile synthetic route for manganese ferrites and can be extended to the rest of the spinel ferrite family.

2.2 Introduction

Due to its unique physical properties including but not limited to strong magnetic anisotropy, high coercivity and Curie Temperature ($T_{c,}$), robust chemical stability as well as moderate magnetization, spinel ferrite magnetic nanoparticles are of great interest today in fundamental science research and for their numerous technological applications. These magnetic particles have been incorporated into various scientific advancements including high density data storage[64], ferrofluid technology[65], contrast enhancement in magnetic resonance imaging (MRI)[66], magneto-optic recording medium[67], stress sensors[68], and drug delivery systems[9, 69]. Thus there is an increasing demand for inexpensive, simplistic, high yield synthetic routes.

Research into the synthesis and characterization of spinel ferrites has been conducted over the last few decades in an effort to develop a synthetic route that can easily produce large quantities of monodispered nanoparticles. Controlling the monodispersity and size of nanoparticles is essential because the finely tunable magnetic properties that are necessary to precisely design nanostructure materials with the desired physical properties are very dependent on these two variables. For instance, simple increases in nanoparticle size from 5 to 6 nm results in ~20 % decrease in the surface to volume ratio of these particles. With this in mind, there are a number of publications on synthetic routes including ball milling[13b], co-precipitation[4, 70], hydrothermal[71], microemulsion[25, 72], sol-gel[73], and thermal decomposition of metal-organic complexes[27a, 74] that use different variables to control the size and distribution. However, each of these methods has its own merits and drawbacks.

The co-precipitation method, with and without micelles, utilizes the oxidation of metal cations in basic conditions followed by heat treatment up to 600°C. Since both schemes use high temperature to provide enough energy to convert the amorphous phase of metal hydroxide to a crystalline spinel, aggregation of particles is commonly observed[25]. The wet chemical deposition or sol-gel method is where the precursors undergo hydrolysis and polycondensation reactions. The final stage, heat treatment, usually reduces the control over morphology and quality of crystallinity making it difficult to achieve the desired materials. Generally, high quality nanoparticles are produced through a thermal decomposition method with metal organic precursors. The quality of the final product can be greatly improved by the addition of a surface stabilizing reagents (i.e. surfactants). However, the synthesis of the metal organic precursors can be challenging, time consuming and/or expensive.

To eliminate this issue, we have designed a metal organic precursor with a facile synthesis route that has the possibility of supplying a variety of metal cations which will be used to produce a multitude of ternary metal oxides. Herein, we report a convenient, cost effective, and large-scale synthesis method of manganese ferrite nanocrystals using inexpensive metal acetate(s) in a moderately hot oleylamine and dibenzyl ether solvent. The manganese ferrite system was also chosen to test the robustness of the aminolytic reaction. Of all the spinel ferrites, $MnFe_2O_4$ is the least thermal stable and will often decompose to its constituent metal oxides, Mn_2O_3 and Fe_2O_3, upon heat treatment in ambient atmosphere. No impurities were found in the nanoparticles synthesized via the aminolytic method and no decomposition was observed at mild heat treatment. We also investigated the surface contribution to magnetic anisotropy and the effects on magnetic properties.

2.3 Experimental

2.3.1 Synthesis of Precursors

The metal acetate precursor was prepared by reacting metal hydroxide with acetic acid. $MnCl_2 \cdot 4H_2O$ (5 mmol) and $FeCl_3 \cdot 6H_2O$ (10 mmol) were dissolved in 100 mL distilled water and stirred for one hour under ambient conditions. Upon the addition of

100 mL of 1 M NaOH solution, a dark brown metal hydroxide precipitate formed. The mixture was stirred for another hour and then the precipitate was collected via centrifugation. The solid was washed several times with distilled water. Metal hydroxide was dissolved with 30 mL of glacial acetic acid at 70˚C overnight. Upon complete evaporation of the liquid, a fine powder with a stoichemetric ratio of 1:2 mixture of $Mn^{2+}(CH_3COO^-)_2$ and $Fe^{3+}(CH_3COO^-)_3$ was collected.

2.3.2 Synthesis of $MnFe_2O_4$ Nanoparticles

$MnFe_2O_4$ was synthesized via the aminolytic reaction. The metal acetate precursor (7.5 mmol) was dissolved in a mixture of 10 mL of oleylamine and 40 mL of dibenzyl ether and stirred for one hour. While purging with Ar, the turbid metal acetate solution was heated to 140˚C and the temperature was maintained for 1 hour. Then the temperature was raised to 240˚C at a ramping rate of 5˚C/min, and the reaction solution was agitated for another hour. Upon cooling to room temperature, the nanoparticles were collected with a magnetic field and washed three times using absolute ethanol. A TEM sample was prepared by dissolving ~6 mg of nanoparticles into 15 mL of hexanes.

2.3.3 Surface Stripping of $MnFe_2O_4$ Nanoparticles

Native nanoparticles were stripped using a 50:50 by volume of 10 M NaOH and absolute ethanol. Native nanoparticles were transferred to a 50 mL beaker with 30 mL of stripping solution. Nanoparticles were agitated in the stripping solution for 3 hours then separated via an applied magnetic field and washed several times with distilled H_2O. After repeating this procedure four times, the nanoparticles were stirred overnight in the stripping solution. The hydroxide coated nanoparticles are separated by an applied magnetic field, washed several times with distilled H_2O then allowed to dry overnight. Dried nanoparticles were then re-ground and transferred to a vial.

2.3.4 Heated Treatment of $MnFe_2O_4$ Nanoparticles in Both Ambient and Argon Atmosphere

Native nanoparticles were heated in tube furnace under ambient atmosphere and continuous argon flow to 200˚C at ramping rate of 5˚C/min for 20 hours. Upon cooling to room temperature, samples were characterized by XRD and SQUID.

2.4 Results and Discussion

2.4.1 Physical and Magnetic Properties of $MnFe_2O_4$

The X-ray diffraction pattern shown in Figure 2.1 indicates that pure spinel phase $MnFe_2O_4$ nanoparticles were synthesized via the aminolytic reaction using a metal-acetate precursor in a mixture of oleylamine and dibenzyl ether. Excellent crystallinity was observed at or above 240 ˚C. Peak position and relative intensity of the products' diffraction pattern matched the standard powder diffraction pattern (ICDD File Number 10-319). The sizes of the nanoparticles were calculated using TOPAZ commercial program which utilizes Bragg peak broadening data to calculate the average size of the nanoparticles. These average sizes correlated nicely to the sizes determined from the TEM micrographs. The shape of particles was near-spherical polyhedron.

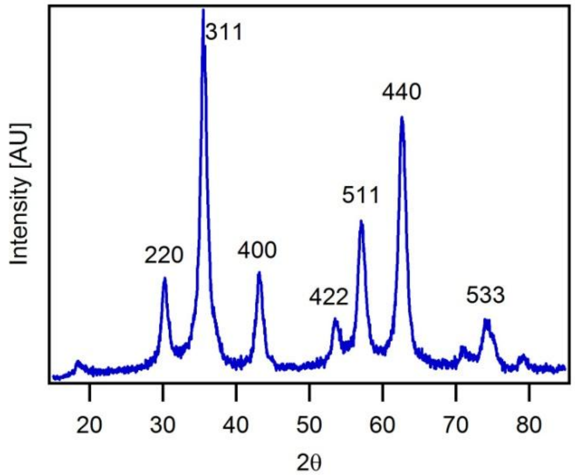

Figure 2.1. X-ray diffraction pattern of ~8 nm $MnFe_2O_4$ nanoparticles.

Figure 2.2 is the temperature dependent magnetic susceptibility measurements at 100 G of different sized nanoparticle. Clearly, each nanoparticle has its own characteristic blocking temperature (T_B), where T_B increases with size (Figures 2.2 and 2.3). The energy barrier (E_A) for rotation of magnetization orientation in a single domain particle has been described by the Stoner-Wohlfarth theory and is given by

$$E_A = KV\sin^2\Theta \qquad (2.4.1.1)$$

where K is the anisotropy of the material, V is the volume of the nanoparticle, and Θ is the angle between an applied magnetic field and the easy axis of a nanoparticle. The blocking temperature of a material is the temperature at which the moments of the nanoparticle are no longer blocked and thus are able to overcome the energy barrier, E_A[48]. As expected the blocking temperature increases with increasing nanoparticle size.

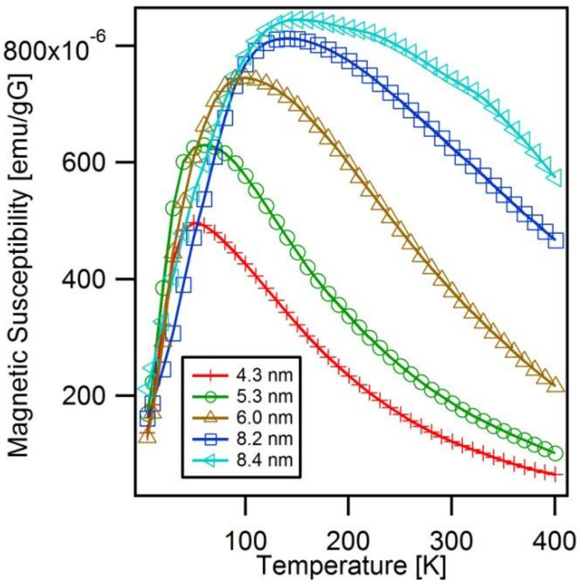

Figure 2.2. Temperature dependent magnetization of $MnFe_2O_4$.

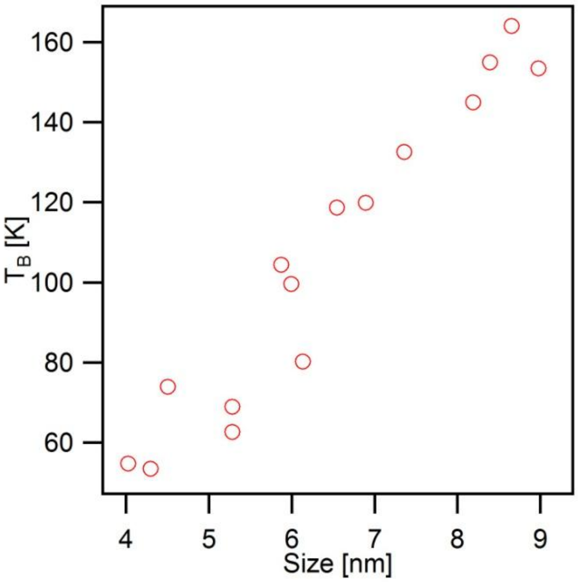

Figure 2.3. Size dependence of blocking temperature (T_B).

Field dependent magnetization measurements at 5 K show the expected hysteresis curve in Figure 2.4. Both the remnant magnetization and saturation magnetization increase with increasing particle size (Figure 2.5).

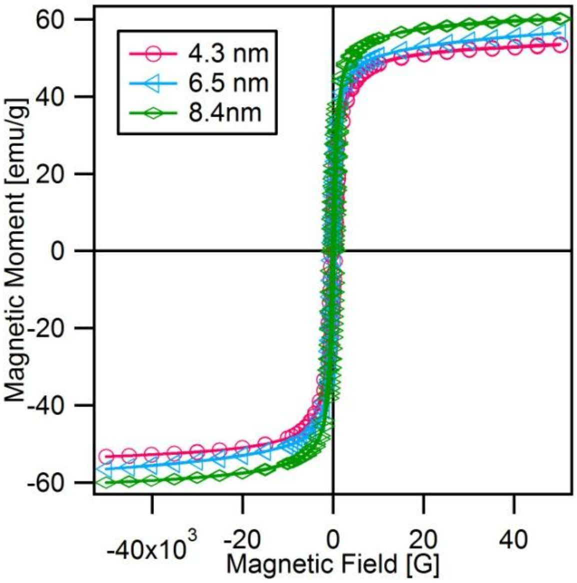

Figure 2.4. Hysteresis curves of $MnFe_2O_4$ nanoparticles at 5 K.

The presence of surface anisotropy accounts for the effects of symmetry reduction caused by an incomplete coordination sphere on the nanoparticle's surface as proposed by Néel. The surface anisotropy (K_s) of a nanoparticle contributes to the total magnetic anisotropy as

$$K = K_{xtal} + (6/d)\, K_s \qquad (2.4.1.2)$$

where K_{xtal} is the bulk magnetocrystalline anisotropy and d is the diameter of the particle[48]. Because the aminolytic reaction produces less than 10 nm particles the surface anisotropy effect on the magnetic properties is large and for the smaller particles it receives a multiplier effect. This is illustrated in the coercivity of the nanoparticles which remains relatively constant over the size range. Two major factors (surface and volume) are contributing to the coercivity strength over this size range for single domain particles.

The coercivity represents the field strength needed to surpass the anisotropy barrier and to allow the magnetization of the nanoparticles to align with the field. This is shown by the Stoner-Wohlfarth theory.

$$H_c = 2K/(\mu_o M_s) \tag{2.4.1.3}$$

where μ_o is the permeability of vacuum and M_s is the magnetic saturation[48]. Since the magnetic anisotropy is directly proportional to activation energy as well as coercivity, the hysteresis loop is expected to widen with increasing particle volume. However, if the surface characteristics dominate the anisotropy calculation as expected in small particles, the field required for alignment will be less for decreasing surface to volume ratio that accompanies increasing particle size[4, 75]. Since the functionalized particles are capped with oleylamine as part of the reaction, the surface effects are lessen because the spins on the surface are not pinned by defects[4]. The surface is passivated by the surfactant and the two factors, volume and surface, balance out giving a level coercivity versus size function for small particles. Because the surfactant is incorporated as part of the reaction, incomplete coverage can occur as modifying the surface spin order. As these factors compete to affect the coercivity through the magnetic anisotropy, the results are shown in the coercivity behavior for particles with a size of 10 nm or less (Figure 2.5).

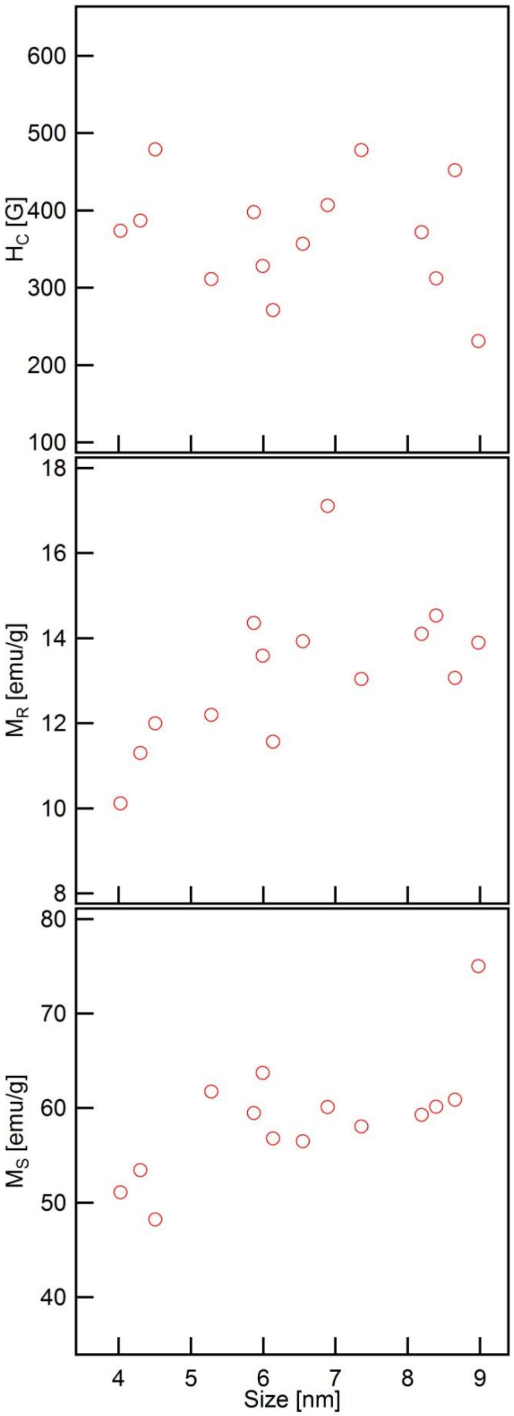

Figure 2.5. (a) Size dependence of coercivity for $MnFe_2O_4$ nanoparticles. (b) Size dependence of remnant magnetization. (c) Size dependence of saturation magnetization.

To help elucidate the factors that affect the magnetic anisotropy, a surface chemistry study was done with six different sized nanoparticles. The next section will discuss effects of the treatments on nanoparticles' magnetic properties

2.4.2 Physical and Magnetic Properties of Surface Modified Nanoparticles

The X-ray diffraction pattern shown in Figure 2.6 indicates no variance between the Ar heated sample, stripped, and the native sample. This confirms that the heat treatment under argon and the stripping with concentrated base solution just removed the surface functionalization of the amine-capped native nanoparticles and did not alter the overall crystal structure of the nanoparticles. However, for the ambient environment heated sample, there is a characteristic shift in the XRD pattern to larger angles indicative of oxidation of manganese ion from 2^+ to 3^+[76]. Without using neutron diffraction to determine any cation distribution changes from sample treatment, all we can do is speculate on changes in cation distribution and coordination state. This change in oxidation state may cause the manganese ion to transition to the octahedral site where it may undergo a Jahn-Teller distortion[76a, 77]. Since diffraction patterns were taken after each treatment, we were able to determine that the average size of the particles did not vary greatly with any of the treatments.

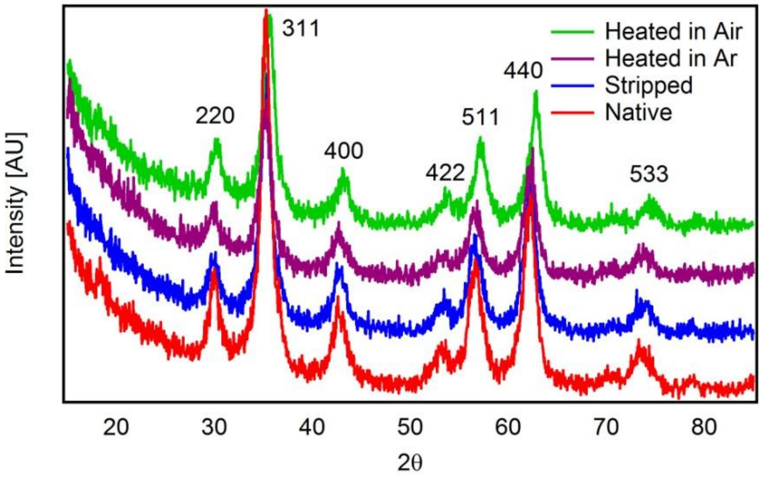

Figure 2.6. X-ray diffraction patterns of ~7 nm native, stripped, heated in argon, and heated in air $MnFe_2O_4$ nanoparticles

Field dependent magnetization measurements at 5 K show that the hysteresis curve changes greatly upon heat treatment of the particles as shown in Figures 2.7 and 2.8. For the native and stripped particles, remnant magnetization and saturation magnetization generally increase with increasing particle size (Figures 2.7 and 2.8). As stated above Néel proposed that surface anisotropy can be affected by surface chemistry and this is reflected in a change in the magnetic properties of nanomaterials. By removing the surfactant in a variety of ways, a comparison can be done to determine the influence of different surface environments on the magnitude of the surface anisotropy effect.

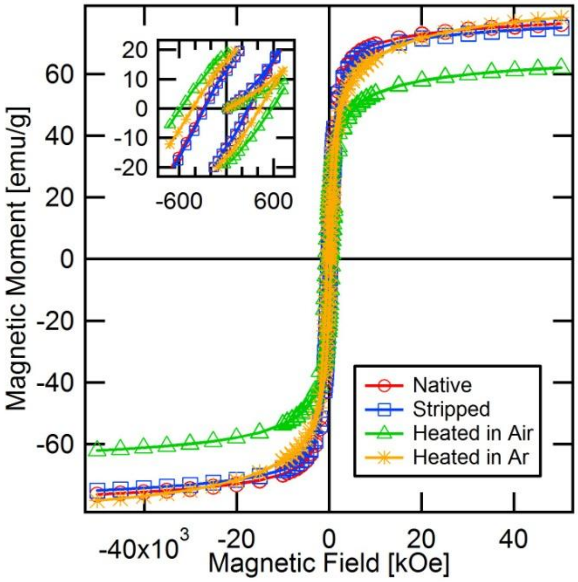

Figure 2.7. Hysteresis curves of native (o), stripped (□) heat treated in air (Δ) and in Ar (∗) spherical ~8 nm $MnFe_2O_4$ nanoparticles at 5 K. Inset shows the coercivity and remnant magnetization in an expand scale.

Because the aminolytic reaction generally produces less than 10 nm particles the surface anisotropy effect on the magnetic properties is large and for the smaller particles it receives a multiplier effect (Equation 2.7). This is illustrated in the coercivity for the native and stripped particles which remains relatively constant over the size range. As discussed before the two major factors contributing to the coercivity strength over this size range for single domain particles are surface characteristics and volume of nanoparticles. Since the coercivity represents the field strength needed to surpass the anisotropy barrier, any change in anisotropy will affect the coercive field. If the surface characteristics dominate the anisotropy calculation as expected, any changes to the surface chemistry should directly correlate to changes in magnetic properties especially coercivity. In the native particles capped with oleylamine from the reaction and the stripped particles capped with hydroxide units due to the basic stripping agent, the surface effects lessen because the spins on the surface are not pinned by defects[4]. The surface is passivated by the surfactant (amine and hydroxide) and the two factors, volume and surface, balance out to give a level coercivity versus size function for small particles. The surfactant on both sets of particles, native and stripped, causes all the particles' magnetic properties to trend together.

However, when the surfactant was removed via heat treatment, the magnetic trends diverge. The surface anisotropy is increased due to the spin disorder created by surface defects from removing the surfactant. Knowing how the surfactant is removed is essential to understanding the cation oxidation and distribution. Coercivity is affected differently for each of the different heat treatments. For the heat treatment under argon, the coercivity is increased due to the increased surface anisotropy caused by removing the surfactant. This causes the coercivity to be inversely related to particle size. As particle size increases the surface anisotropy contribution decreases due to the reduced surface to volume ratio and the bulk anisotropy domination in coercivity calculation. However, the particles treated in ambient atmosphere show a large jump in coercivity which cannot be completely attributed to larger surface anisotropy contribution. In the case of the oxidation of the manganese ions, there would be an increase in local strain that could cause an increase in crystal (bulk) anisotropy[76c]. This anisotropy increase in combination with the greater surface contribution results in a much larger coercivity increase than samples heated in argon which is illustrated in Figures 2.7 and 2.8.

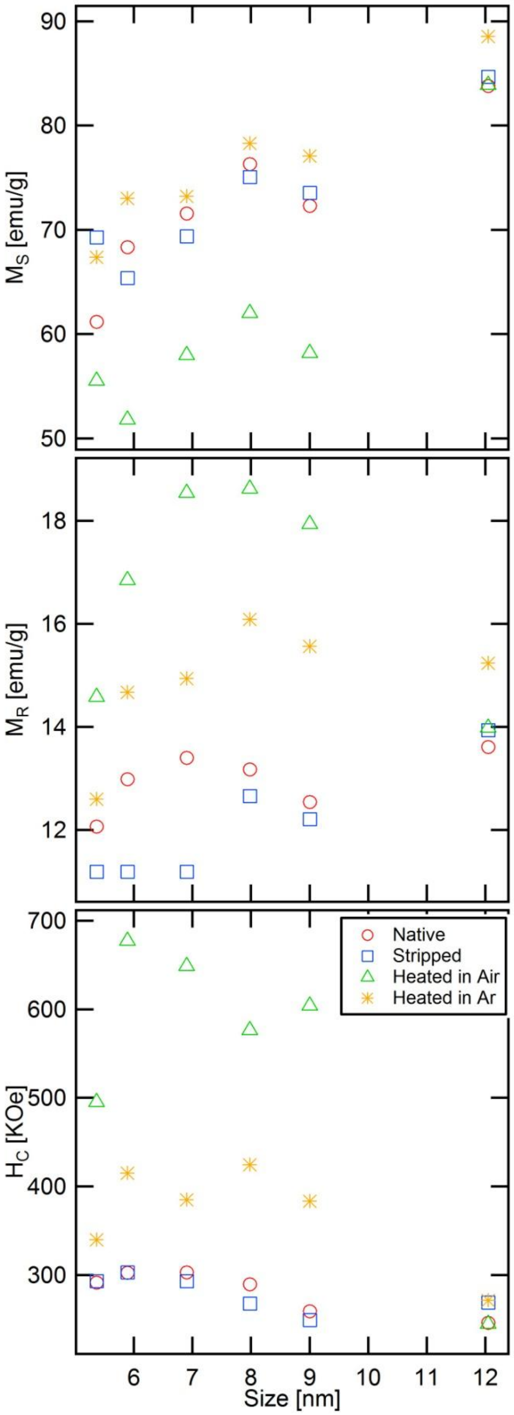

Figure 2.8. (a) Size dependence of saturation magnetization for $MnFe_2O_4$ nanoparticles. (b) Size dependence of remnant magnetization. (c) Size dependence of coercivity.

Surface passivation and defects also explain the increase in remnant magnetization upon heating both in air and in argon. With the surface functionality intact, the surface spins rotate and relax more freely thus when the magnetic field is removed, less magnetization is retained. However, for the heat treated samples the surface spins are pinned into place by defects and do not relax as quickly upon the removal of the field making the magnetic memory greater than the native and the stripped particles. The difference in the magnitude of the increase is due to the same properties that influence magnetic saturation.

The magnetic saturation of both the native and the stripped particles varies from the heated samples. For the sample heated in argon, there is a slight increase in magnetic saturation. This is probably due to the addition of thermal energy to the system. This would allow the nanoparticles to come to a more stable equilibrium by correcting any cation site or surface defects due to the aminolytic synthesis[78]. Also, the heated sample may have a cation distribution closer to the ceramic methods 81% normal spinel ferrite conformation instead of the wet chemical methods 33% normal which would affect the nanoparticles saturation magnetization[78-79]. For the sample heated in air, there is a loss in overall saturation magnetization. This is due to the oxidation of some of the manganese cations. The Mn^{3+} resulting from the oxidation state changes might then occupy the octahedral site due to a better Crystal Field Stabilization Energy than found at the tetrahedral sites[80]. Once in the octahedral sites, the manganese cation could undergo a Jahn-Teller distortion[77]. This will lower its magnetic contribution from $5\mu_B$ to $0\mu_B$. Even if the oxidized manganese ions do not undergo distortion there is still a reduction in magnetic contribution from $5\mu_B$ to $4\mu_B$ drop[81]. Both of these situations would result in a drop in overall magnetization as seen in Figures 2.7 and 2.8.

2.5 Conclusion

Synthesis of manganese ferrite via the aminolytic reaction in dibenzyl ether along with oleylamine has been demonstrated, and the magnetic properties regarding size are in excellent agreement with theoretical predictions and literature values. The magnetic properties of nanoparticles are largely dependent on the volume and surface characteristics of the spinel ferrites. The aminolytic reaction is a truly robust synthesis method for production of high quality monodispersed nanoparticles in large quantities with a minimal amount of toxic organic waste. We have also shown that a simplistic single source metal-carboxylate can be used as a metal precursor, which will allow for easier scalability, required for the transition to industry. Surface chemistry and particle treatment have a large affect on the magnetic properties and need to be considered for any potential application. These aminolytic nanoparticles are an ideal start for the investigations in sensors utilizing magnetic output response.

CHAPTER 3

THE EFFECT OF MN SUBSTITUION ON THE MAGNETIC PROPERTIES OF COBALT FERRITE NANOPARTICLES

3.1 Abstract

Magnetic nanoparticles are being increasingly incorporated into sensing technology. Magnetostrictive properties of oxide materials are particularly useful in sensing changes in operating systems due to their good response and chemical robustness. Cobalt ferrites doped with manganese show increasing magnetostriction responses. The magnetic properties and responses of the spinel ferrites system are greatly influenced by quantum couplings of the magnetic ions. Thus understanding the couplings between these ions allows for manipulation of the desired magnetic properties. Manganese doping in the cobalt ferrite system allows for the investigation of the effects of orbital momentum quantum coupling by exchanging a metal ion with high orbital momentum contribution, Co^{2+}, with a metal ion with no orbital momentum contribution, Mn^{2+}. To fully investigate these quantum coupling effects, all the compositions in the series $Co_{1-x}Mn_xFe_2O_4$, where x= 0.0, 0.1, 0.2, 0.3, 0.4, 0.5, 0.6, 0.7, 0.8, 0.9, and 1.0 were synthesized via the aminolytic reaction. The manganese metal ion prefers to occupy the tetrahedral (A) sites in spinel ferrites before it fills the octahedral (B) sites. This preference explains the jag in magnetic data between 40 and 50 % doping when mixed occupancy starts to occur. The coercivity decreases with increasing Mn^{2+} concentration due to the continued swapping of high magnetic anisotropy ion (Co^{2+}) with a low

magnetic anisotropy ion (Mn^{2+}). To our knowledge, this work is the first full composition series of $Co_{1-x}Mn_xFe_2O_4$ reported.

3.2 Introduction

Research into doped magnetic materials continues to attract attention due to the ability to tune magnetic properties for desired applications. The series $Co_{1-x}Mn_xFe_2O_4$ shows great promise as magnetostrictive materials for applications in sensing technology and the automotive industry[5, 7, 82]. Magnetostriction is a magnetic property where the dimensions of the magnetic material changes when the material is exposed to a magnetic field[5]. Sensors utilizing spinel ferrite materials are superior to the current available technology as these systems are very thermally stable over a wide temperature range. Cobalt ferrite has shown the highest anisotropic magnetostrictive strains, up to 900 ppm, for the ferrite family[7b, 8, 83]. Since $CoFe_2O_4$ has high magnetocrystalline anisotropy (K) mostly from the Co(II)[84] contribution, replacing this divalent metal ion with a much smaller contributor such as Mn(II)[85] will greatly affect the magnetic properties and lead to a new area of investigation for magnetostrictive materials[83].

Manipulations of magnetic properties require understanding of the spinel ferrite crystal and magnetic structure. Spinel ferrite, which is a cubic lattice of closed-packed oxygen ions, has the characteristic structure of $A^{2+}B^{3+}{}_2O_4$ with A being the tetrahedral interstitial sites and B being the octahedral interstitial sites usually occupied by Fe(III)[45]. When the A sites are completely occupied by Fe^{3+} and the B sites are randomly occupied by M^{2+} and Fe^{3+} cations, this structure is called inverse spinel, $B(AB)O_4$. The cobalt ferrite is almost completely inverse with just a few Co^{2+} cations occupying the tetrahedral (A) sites[84, 86]. The manganese ferrite is a mixed spinel system with the Mn^{2+} occupying both the octahedral (B) and tetrahedral (A) sites[87]. The spinel ferrite nanoparticle system exhibits superparamagnetic behavior above the blocking temperature (T_B) and antiferromagnetic ordering below the T_B because the net magnetic moment points along the "easy" axis. Magnetic ordering occurs because the magnetic moments of the tetrahedral sites are aligned in a parallel relationship while the octahedral sites are also aligned parallel to other octahedral sites. Ferrimagnetic behavior is exhibited for spinel ferrites because the magnetic moments of the octahedral sites are aligned antiparallel with respect to the tetrahedral sites in the structure but the magnitudes of these moments for the octahedral and tetrahedral sites are not cancelled by each other (Figure 3.1 and 3.2).

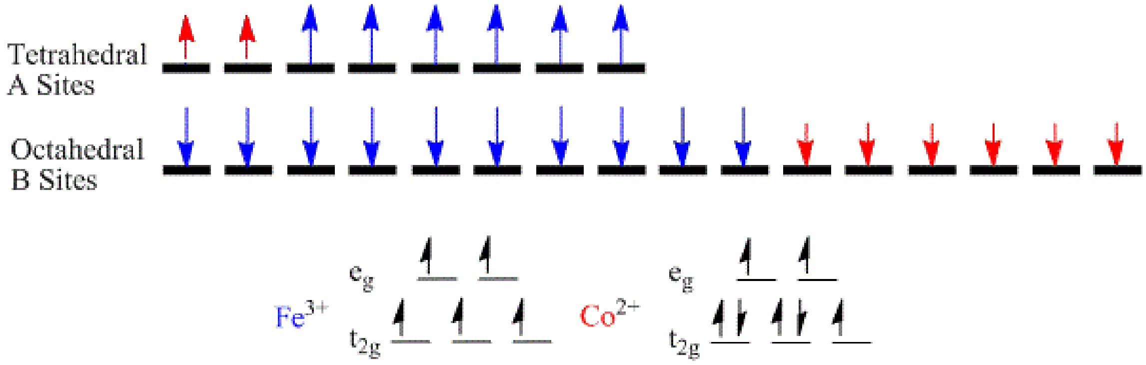

Figure 3.1 Cation Distribution of $CoFe_2O_4$

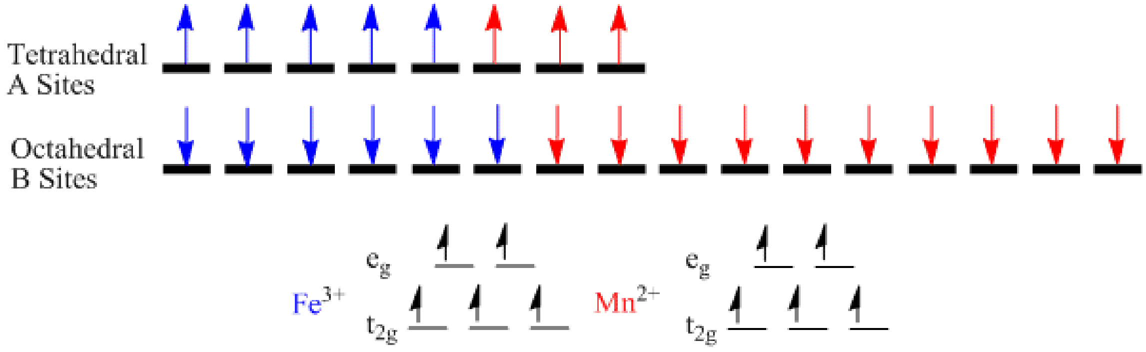

Figure 3.2 Cation Distribution of $MnFe_2O_4$

Limitations of the alloy current systems such as Terfenol-D, $SmFe_2$ and other rare-earth iron compounds include poor mechanical properties, expensive materials, eddy currents at high frequencies, and the need for a single crystal for many applications. By focusing on manipulations of oxide nanoparticle magnetic properties, we can hopefully eliminate some of these issues. These materials would be much cheaper, have good corrosion resistance and better mechanical properties as well as no eddy currents at high frequencies[7b, 88]. To make these materials viable, the magnetomechanical hysteresis would need to be reduced especially at elevated temperatures. Literature indicates that doping in manganese for cobalt in the cobalt ferrite system reduces magnetomechanical hysteresis[7a, 82a]. To find the best materials for sensing application (e.g. lowest hysteresis) we synthesized and characterized a complete series of cobalt ferrites doped with manganese.

3.3 Experimental

3.3.1 Synthesis of Precursors

The metal acetate precursor was prepared by reacting metal hydroxide with acetic acid. $CoCl_2 \cdot 4H_2O$ (5-x mmol) $MnCl_2 \cdot 4H_2O$ (x mmol) and $FeCl_3 \cdot 6H_2O$ (10 mmol) were dissolved in 100mL distilled water and stirred for one hour under ambient conditions. Upon the additional of 100mL of 1 M NaOH solution, a dark brown metal hydroxide precipitate formed. The mixture was stirred for another hour and then the precipitate was collected via centrifugation and washed several times with distilled water. Metal hydroxide was dissolved with 30 mL of glacial acetic acid (99%) at 70 ˚C overnight.

Upon complete evaporation of the liquid, a fine powder with a stoichemetric ratio of 1:2 mixture of Co^{2+} and $Mn^{2+}(CH_3COO^-)_2$ and $Fe^{3+}(CH_3COO^-)_3$ was collected.

3.3.2 Synthesis of $Co_{1-x}Mn_xFe_2O_4$ Nanoparticles

All the compositions in the series $Co_{1-x}Mn_xFe_2O_4$, where x= 0.0, 0.1, 0.2, 0.3, 0.4, 0.5, 0.6, 0.7, 0.8, 0.9, and 1 were synthesized via the aminolytic reaction. Pre-mixed metal acetate (7.5 mmol) was dissolved in a mixture of 10 mL of oleylamine and 40 mL of dibenzyl ether, and stirred for one hour. While purging with Ar, the turbid metal acetate solution was heated to 140 ˚C and the temperature was maintained for one hour. Then the temperature was raised to 240˚C at a ramping rate of 5˚C/min, and the reaction solution was agitated for another hour. Upon cooling to room temperature, the nanoparticles were separated with a magnetic field and washed three times using absolute ethanol. The samples were characterized by magnetic measurement using a Quantum Design MPMS-5S SQUID magnetometer and powder x-ray diffraction studies using a Panalytical X-Ray Diffractometer. Particles were immobilized in eicosane ($C_{20}H_{42}$, Aldrich) for the hysteresis measurements. Inductively Coupled Plasma Atomic Emission Spectroscopy (ICP-AES) sample were made by digesting ~ 5 mg nanoparticles with 10 mL nitric acid (40%) overnight in parabomb at 220 ˚C overnight. Then 1 mL aliquot was removed and diluted to 10 mL with HPLC grade water. Samples were submitted to Chemical Analysis lab at Georgia Institute of Technology for element analysis on Perkin Elmer Inductively Coupled Plasma Optical Emission Spectrometer (ICP), OPTIMA 7300DV.

3.4 Results and Discussions of Physical and Magnetic Properties

The X-ray diffraction pattern shown in Figure 3.3 indicates that pure spinel phase $Co_{1-x}Mn_xFe_2O_4$ nanoparticles were synthesized via the aminolytic reaction using a metal-acetate precursor in a mixture of oleylamine and dibenzyl ether solvent. Excellent crystallinity was observed at or above 240 ˚C. Peak position and relative intensity of the products' diffraction pattern matched the standard powder diffraction pattern (ICDD File Number 22-1086).

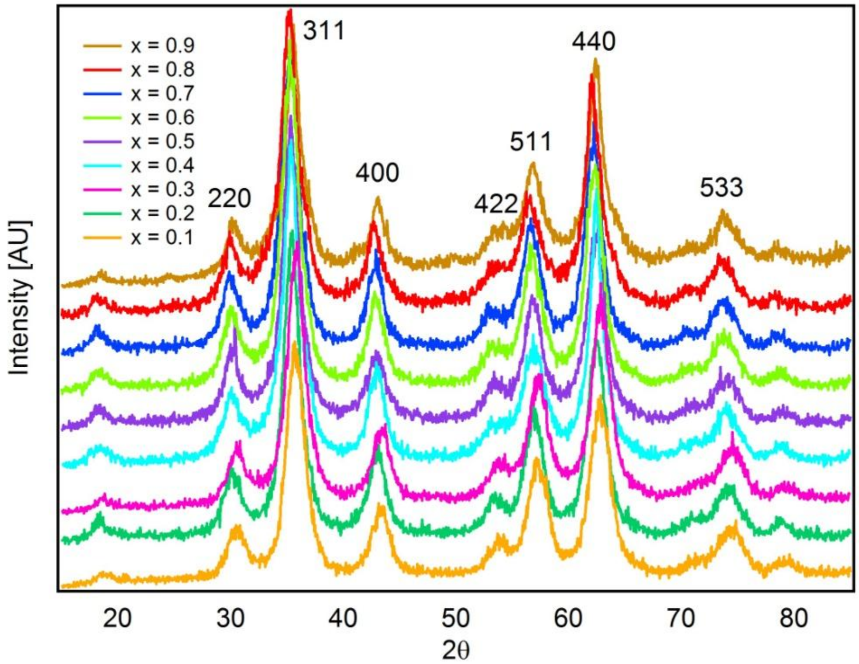

Figure 3.3 Powder X-Ray Diffractions pattern for ~5 nm $Co_{1-x}Mn_xFe_2O_4$ nanoparticles.

Average particle size ~5 nm was determined by the Scherrer equation using the Bragg peak broadening data. The sizes of the nanoparticles were calculated using the strongest five peaks. ICP-AES data confirmed the cationic ratio between Co^{2+}:Mn^{2+} and Fe^{3+} of 1:2 is maintained for all nanoparticles produced and theoretical Mn composition calculated from the molar ratio in reagents and the actual composition in nanoparticles by elemental analysis (Table 3.4).

Table 3.4: Elemental Analysis of $Co_{1-x}Mn_xFe_2O_4$ Nanoparticles

Theoretical Mn percentage	0	10	20	30	40	50	60	70	80	90	100
Mn percentage from ICP-AES	0	10.1	19.5	30.3	40.2	48.5	59.2	70.3	81.1	91.1	100

Figure 3.4 shows the manganese doping dependence on the magnetic susceptibility measurements of the nanoparticles at 100 G. Clearly, each nanoparticle has its own characteristic blocking temperature (T_B); T_B increases initially with doping and then decreases as the particles enter the mixed occupancy state around 40 and 50%. Cobalt and iron metal ions will occupy both tetrahedral (A) and octahedral (B) sites as pure cobalt ferrite is a mixed spinel system. The manganese metal ion prefers to occupy the tetrahedral (A) sites in the spinel ferrites before it will fill the octahedral (B) sites. For the pure cobalt ferrite, the blocking temperature is much higher due to the influence of Co^{2+} ion and is greatly reduced with the introduction of any manganese. This preference explains the jag in magnetic data between 40 and 50 % doping when mixed occupancy starts to occur.

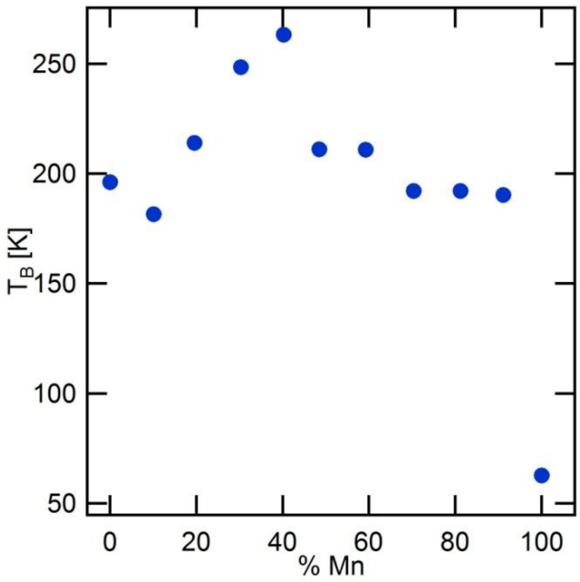

Figure 3.4. Blocking Temperature (T_B) dependence on manganese doping for ~5 nm $Co_{1-x}Mn_xFe_2O_4$ nanoparticles.

The energy barrier (E_A) for rotation of magnetization orientation in a single domain particle has been described by the Stoner-Wohlfarth theory and is given by

$$E_A = KV\sin^2\Theta \tag{3.4.1}$$

where K is the anisotropy of the material, V is the volume of the nanoparticle, and Θ is the angle between an applied magnetic field and the easy axis of a nanoparticle. The blocking temperature of a material is the temperature at which the magnetic moments of the nanoparticles are no longer blocked and are able to overcome the energy barrier, E_A[54]. We speculate that the blocking temperature initially increases because the activation energy barrier is increased by the increased Co^{2+} ion occupancy of the octahedral sites. Cobalt ion has high magnetic anisotropy[84] and the octahedral sites contribute more to the material's anisotropy due to symmetry. At 40-50% manganese content the decrease in magnetic anisotropy from the swapping of high magnetic anisotropy ion (Co^{2+}) with a low magnetic anisotropy ion (Mn^{2+}) starts to reduce the cobalt couplings on the octahedral sites by the introduction of manganese metal ion onto the B sites causing the T_B decrease. Neutron diffraction studies will need to be performed to confirm that cation distributions for the manganese doped cobalt ferrite spinels.

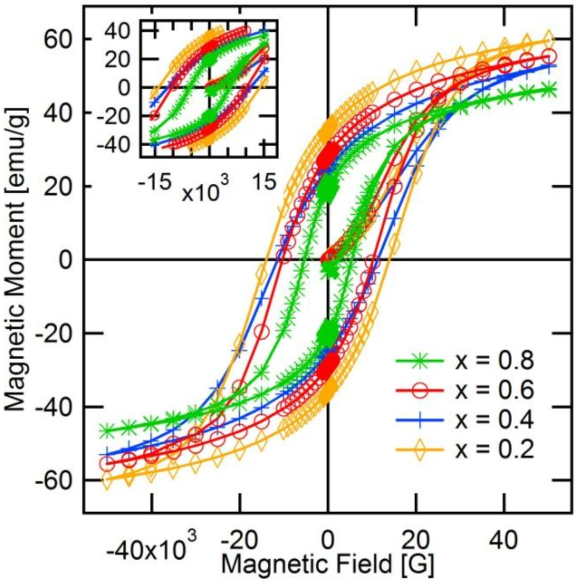

Figure 3.5 Overlaid hysteresis curves for varying doping amounts of manganese for ~5 nm $Co_{1-x}Mn_xFe_2O_4$ nanoparticles at 5 K. Inset shows the coercivity in detail.

Field dependent magnetization measurements at 5 K show that hysteresis curve changes with increasing manganese ion content of the nanoparticles (Figure 3.5). For the doped nanoparticles, remnant magnetization and saturation magnetization decrease with increasing manganese doping (Figure 3.6). The magnetic arrangement of the spinel ferrite system is antiparallel coupling of two parallel magnetically aligned sheets that corresponds to the coupled tetrahedral and octahedral sites. Since the octahedral and tetrahedral sites are aligned in opposite directions, doping with the manganese ion on the tetrahedral sites will decrease the magnetic response as shown in Figure 3.6 even though Mn^{2+} has $5\mu_B$ response to the $3\ \mu_B$ response of Co^{2+} ion that it replaces. This magnetic response occurs because the tetrahedral sites cancel out some of the magnetic moments of the octahedral sites and thus reduce the overall magnetic moment of the unit cell.

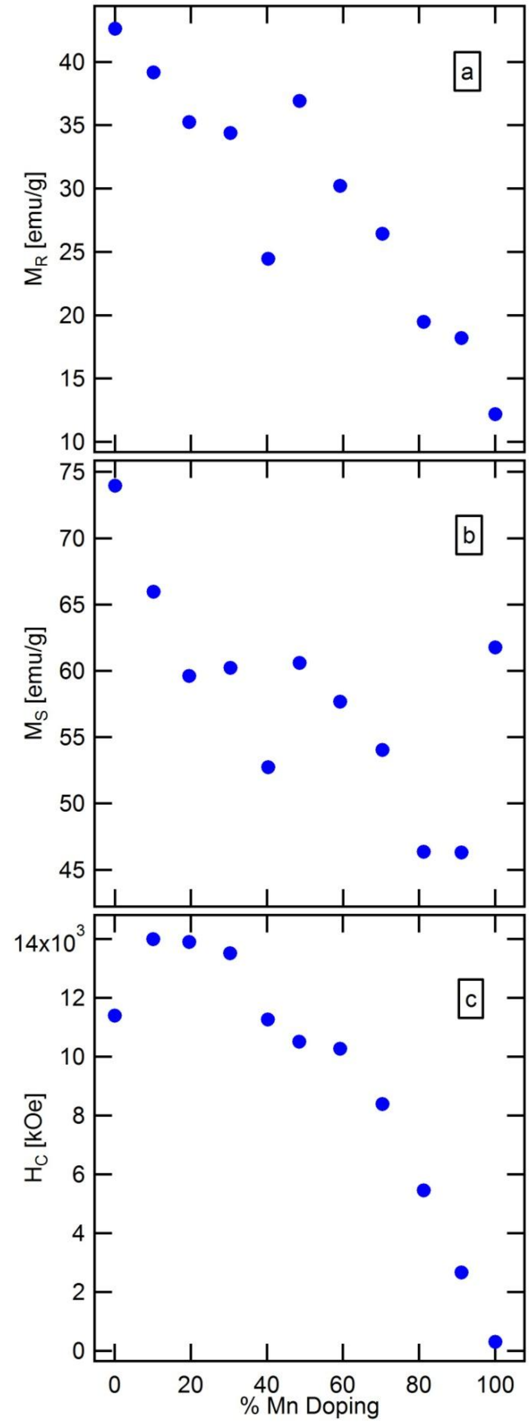

Figure3.6. (a) Remnant magnetization dependence on manganese doping for ~5 nm $Co_{1-x}Mn_xFe_2O_4$ nanoparticles. (b) Saturation magnetization dependence on manganese doping. (c) Coercivity dependence on manganese doping.

The coercivity represents the field strength needed to surpass the anisotropy barrier and to allow the magnetization of the nanoparticles to align with the applied field. This is shown by the Stoner-Wohlfarth theory

$$H_c = 2K/(\mu_o M_s) \tag{3.4.2}$$

where μ_o is the permeability of vacuum and M_s is the magnetic saturation[48]. Since the magnetic anisotropy is directly proportional to the activation energy as well as the coercivity, the hysteresis loop is expected to widen with increasing particle volume so for the purpose of determining the effect of manganese ion concentration on coercivity, particle size was held constant at ~5 nm. The coercivity decreases with increasing Mn^{2+} concentration due to the continued swapping of high magnetic anisotropy ion (Co^{2+}) with a low magnetic anisotropy ion (Mn^{2+}) (Figure 3.6).

3.5 Conclusions

All the compositions in the series $Co_{1-x}Mn_xFe_2O_4$, where x= 0.0, 0.1, 0.2, 0.3, 0.4, 0.5, 0.6, 0.7, 0.8, 0.9, and 1 were synthesized via the aminolytic reaction. We have shown that the coercivity does decrease with increasing Mn^{2+} concentration in the cobalt ferrite nanoparticles systems. These materials should be good candidates for magnetostriction studies and will hopefully find applications in the automotive industry.

CHAPTER 4

THE EFFECT OF CR SUBSTITUION ON THE MAGNETIC PROPERTIES OF MANGANESE FERRITE NANOPARTICLES

4.1 Abstract

Manganese ferrites doped with chromium show increasing magnetic frustrated responses. This doping allows for the investigation of the effects of orbital momentum quantum coupling by exchanging a metal ion with high orbital momentum contribution, Fe^{3+}, with a metal ion with no orbital momentum contribution, Cr^{3+}. All the compositions in the series $MnFe_{2-x}Cr_xO_4$, where x= 0.0, 0.05, 0.13, 0.25, 0.43, 0.62, and 0.85, were synthesized via the In-situ aminolytic method. This reaction uses metal salts and sodium propionate as the precursors. Oleylamine is a reactant, solvent, and stabilizing agent in this method. Though manganese ferrite is a mixed system $[Fe^{3+}_{0.67}Mn^{2+}_{0.33}][Mn^{2+}_{0.67}Fe^{3+}_{1.33}]O_4$, chromium ions preferentially occupy the octahedral (B) sites. Low chromium concentrations strengthen the L-S couplings due to the unquenched angular orbital momentum. High chromium concentration weakens the couplings between the A and B sites which results in the decreasing in the overall magnetic moment by destroying the magnetic arrangement. Chromium coupling on similar sites is very strong and at x=1 result in a disorder state. At higher concentrations, x=2, magnetic spins start canting resulting from the loss of antiparallel alignment that defines the spinel ferrite magnetic system. In our series at the highest doping concentration, there is a dramatic shift in magnetic properties due to frustration of the system and a loss of the strong Fe^{3+}_A-Fe^{3+}_B coupling[60].

4.2 Introduction

Research into doped magnetic materials continues to attract attention due to the ability to tune magnetic properties for desired applications. Control over the magnetic properties such as superparagmagnetism and coercivity requires a fundamental understanding of magnetism including the effects of quantum couplings, orbital angular momentum, and metal ion site preferences. Analyzing the magnetic properties of the series $MnFe_{2-x}Cr_xO_4$ is a systematic way to correlate the fundamentals concepts with their applicable properties.

Spinel ferrites have a well studied crystal structure and a very informative magnetic ordering structure that can help elucidate the links between atomic changes, made by chemical manipulations, on marcoproperties of the synthesized materials[25]. Spinel ferrite has the characteristic structure of $A^{2+}B^{3+}{}_2O_4$ containing two cation sites, A being tetrahedral and B octahedral, with oxygen coordinating to the central metal ion in both cases[45]. The manganese ferrite is a mixed spinel system with the Mn^{2+} occupying both the octahedral (B) and tetrahedral (A) sites[87]. The spinel ferrite nanoparticle system exhibits superparamagnetic behavior above the blocking temperature (T_B) and antiferromagnetic ordering occurs below the T_B because the net magnetic moments point along the “easy” axis. Magnetic ordering occurs because the magnetic moments of the tetrahedral sites are aligned in a parallel relationship while the octahedral sites are also aligned parallel to other octahedral sites. Ferrimagnetic behavior is exhibited for spinels because the magnetic moments of octahedral and tetrahedral sites are aligned antiparallel in the structure but the magnitude of the resultant vector of the magnetic moments is not zero (Figure 4.1).

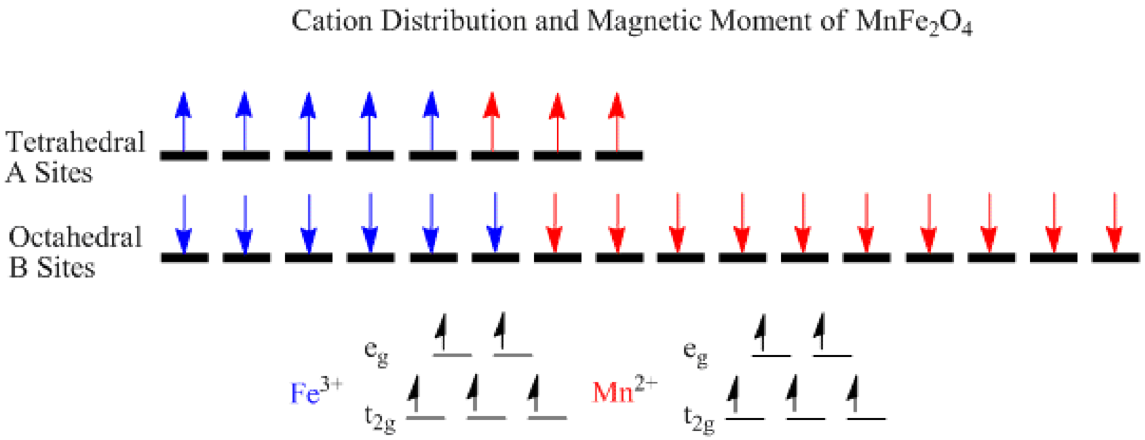

Figure 4.1. Cation Distribution of $MnFe_2O_4$

This system, analogous to a previously published study done by our group[62], gives another vantage point to study the role of Fe^{3+} in spinel ferrites through the variation of chromium ion doping. A decrease in magnetization is expected due to the replacement of iron ion with the weaker magnetic ion, chromium. Since Cr^{3+} has a relatively large unquenched orbital angular momentum, the replacement of the zero orbital angular momentum contributor Fe^{3+} should offer insight into the influence of d-orbital degeneracy and symmetry towards magnetic properties.

4.3 Experimental

4.3.1Synthesis of $MnFe_{2-x}Cr_xO_4$ Nanoparticles

A series of compositions in the system $MnFe_{2-x}Cr_xO_4$, where x= 0.0, 0.05, 0.13, 0.25, 0.43, 0.62, and 0.85 were synthesized via the In-Situ aminolytic method. $MnCl_2 \bullet 4H_2O$, 5 mmol (Alfa Aesar, 98.0%), $FeCl_3$, 10-x mmol (Alfa Aesar, 98.0%), $[Cr(H_2O)_4Cl_2]Cl \bullet 2H_2O$, x mmol (Alrich, Reagent Grade), and sodium propionate,

CH_3CH_2COONa 40 mmol (TCI, Reagent Grade), were dissolved 50 mL of oleylamine (TCI, 99%) and then stirred for one hour. Oleylamine is a reactant, solvent, and stabilizing agent in this method. While purging with Ar, the turbid metal propionate solution was heated to 140 ˚C and the temperature was maintained for one hour. Then the temperature was raised to 240˚C at a ramping rate of 5˚C/min and the reaction solution was agitated for another hour. Upon cooling to room temperature, the nanoparticles were separated with applied magnetic field and washed several times using absolute ethanol and DI water. The samples were characterized by magnetic measurements using a Quantum Design MPMS-5S SQUID magnetometer and powder x-ray diffraction studies using a Panalytical X-Ray Diffractometer. Particles were immobilized in eicosane ($C_{20}H_{42}$, Aldrich) for the hysteresis measurements. Inductively Coupled Plasma Atomic Emission Spectroscopy (ICP-AES) samples were made by digesting ~ 5 mg nanoparticles with 10 mL nitric acid (40%) overnight in parabomb at 220 ˚C overnight. Then 1 mL aliquot was removed and diluted to 10 mL with HPLC grade water. Samples were submitted to Chemical Analysis lab at Georgia Institute of Technology for elemental analysis on a Perkin Elmer Inductively Coupled Plasma Optical Emission Spectrometer (ICP), OPTIMA 7300DV.

4.4 Results and Discussion of Physical and Magnetic Properties

The X-ray diffraction patterns shown in Figure 4.2 indicates that pure spinel phase $Mn_2Fe_{2-x}Cr_xO_4$ nanoparticles were synthesized via the In-Situ aminolytic method using metal salts and sodium propionate in oleylamine. Excellent crystallinity was observed at or above 240 ˚C. Peak position and relative intensity of the products' diffraction pattern matched the standard powder diffraction pattern (ICDD File Number

10-319). Average particle size ~8 nm was determined by the Scherrer equation using the Bragg peak broadening data. The sizes of the nanoparticles were calculated using the most intense five peaks.

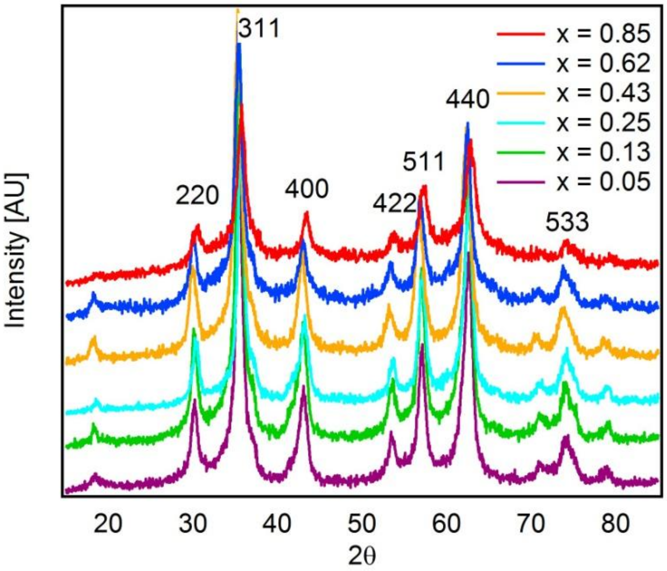

Figure 4.2. Powder X-Ray Diffractions pattern for ~8 nm $Mn_2Fe_{2-x}Cr_xO_4$ nanoparticles.

ICP-AES data calculated the cationic ratio between Mn^{2+}, Fe^{3+}, Cr^{3+} for all nanoparticles produced and theoretical Cr composition calculated from the molar ratio in reagents and the actual composition in nanoparticles by elemental analysis (Table 4.4).

Table 4.4: Elemental Analysis of $MnFe_{2-x}Cr_xO_4$ Nanoparticles

Theoretical Cr percentage	0	2.5	10	20	25	42.5
Cr percentage from ICP-AES	0	2.5	6.5	12.75	21.4	30.75

Figure 4.3 shows the magnetic susceptibility measurements dependence on chromium doping of nanoparticles at 100 G. Clearly, each nanoparticle has its own characteristic blocking temperature (T_B), and the T_B increases initially with doping and

then decreases as the particles enter the magnetically disordered (canting) state around 20%. Manganese and iron metal ions will occupy both tetrahedral (A) and octahedral (B) sites as pure manganese ferrite is a mixed spinel system. The chromium metal ion prefers to occupy the octahedral (B) sites in the spinel ferrites before it fills the tetrahedral (A) sites[26, 60, 75].

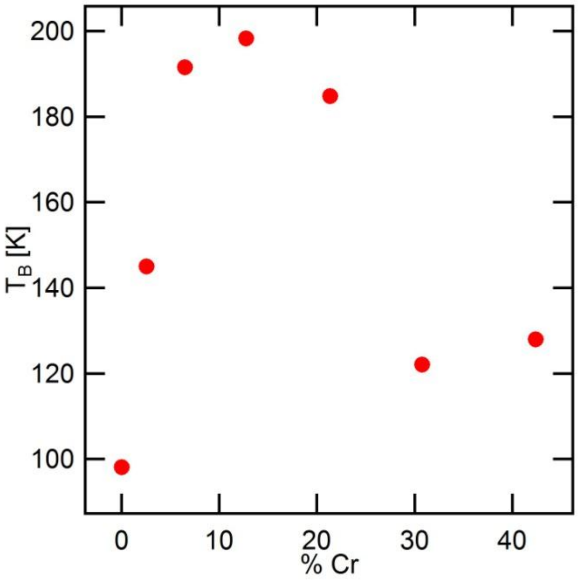

Figure 4.3. Blocking Temperature (T_B) dependence on chromium doping for ~8 nm $Mn_2Fe_{2-x}Cr_xO_4$ nanoparticles.

The energy barrier (E_A) for rotation of magnetization orientation in a single domain particle has been described by the Stoner-Wohlfarth theory and is given by

$$E_A = KV\sin^2\Theta \tag{4.4.1}$$

where K is the anisotropy of the material, V is the volume of the nanoparticle, and Θ is the angle between an applied magnetic field and the easy axis of a nanoparticle. The blocking temperature of a material is the temperature at which the moments of the nanoparticle are no longer blocked and are able to overcome the energy barrier, E_A[54]. For the pure manganese ferrite, the blocking temperature is lower due to the influence of Fe^{3+} ion zero orbital angular momentum. T_B is increased with the introduction of any chromium, which has a much larger orbital angular momentum contribution, thus increasing the material's overall magnetic anisotropy. Chromium has a larger orbital angular momentum contribution due to the decrease in symmetry of the polyhedron which increases the degeneracy of the d-orbitals. This results in stronger spin-orbital coupling that raises the magnetic anisotropy of the whole system[63]. We speculate that the blocking temperature decreases at ~20% chromium is due to magnetic disorder introduced by Cr^{3+} contribution to the quantum couplings on the octahedral sites. Chromium also has a large negative exchange constant indicating a strong preference for antiparallel coupling between the octahedral (B) sites. This causes a deviation from Néel's model and increases the magnetic frustration of the material[60]. Upon further chromium doping eventually the spinel ferrite antiparallel A-B couplings would be destroyed and the magnetic moments would form a canted spiral[89]. Because of these chromium couplings the magnetic anisotropy is reduced at ~20% chromium concentrations and causes a decrease in T_B. Neutron diffraction studies will be need to confirm that cation distributions and determine the magnetic unit cell for the chromium doped manganese ferrite spinels.

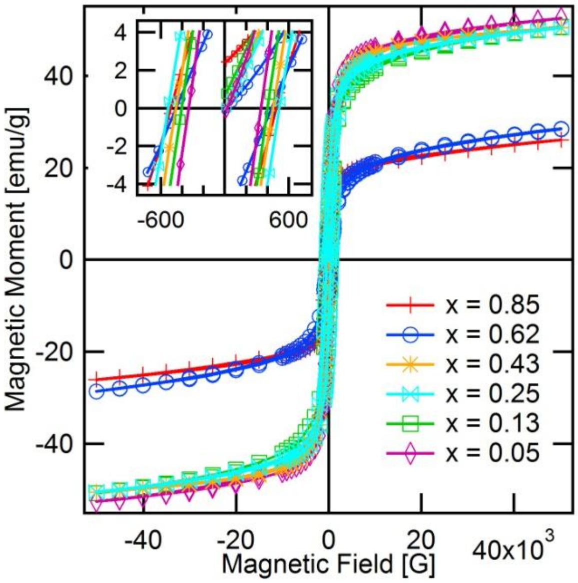

Figure 4.4. Overlaid hysteresis curves for varying doping amounts of chromium for ~8 nm $Mn_2Fe_{2-x}Cr_xO_4$ nanoparticles at 5 K. Inset shows the coercivity in detail.

Field dependent magnetization measurements at 5 K show that the hysteresis curves change with increasing chromium ion content of the nanoparticles (Figure 4.4). For the doped nanoparticles, remnant magnetization and saturation magnetization decrease with increasing chromium doping (Figure 4.5). The saturation and remnant magnetization are due to the resultant of magnetic moments from the metal ions in the system. By replacing a Fe^{3+} with Cr^{3+}, the magnetic contribution is lowered from $5\mu_B$ to $3\mu_B$ leading to the loss of magnetic response seen in the doped system.

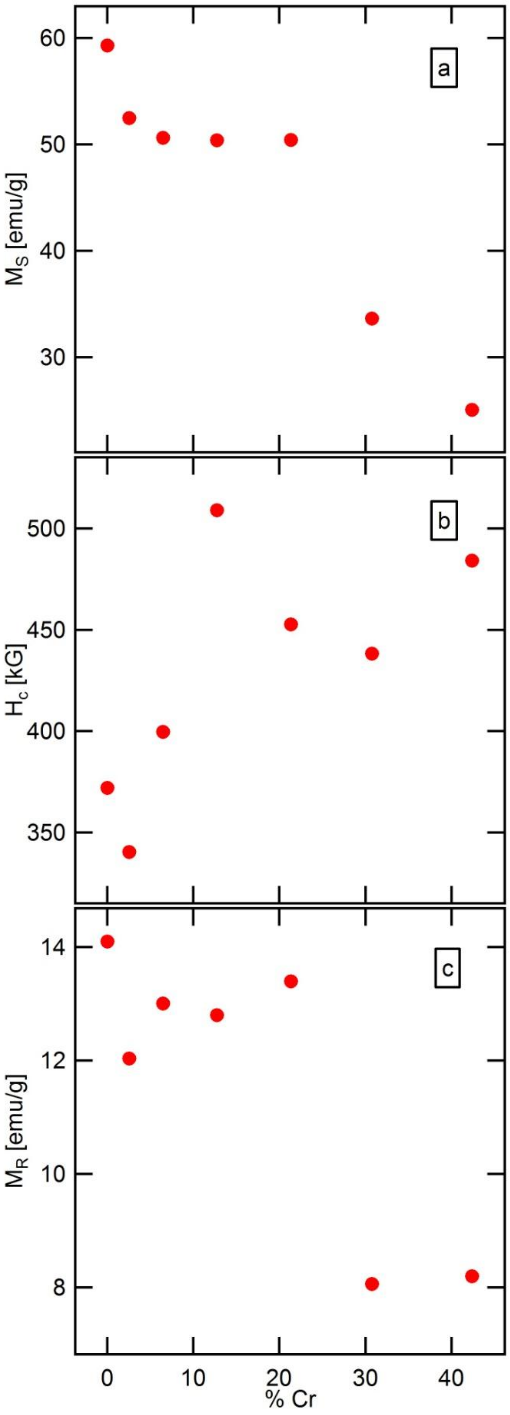

Figure 4.5. (a) Saturation magnetization dependence on chromium doping for ~8 nm $Mn_2Fe_{2-x}Cr_xO_4$ nanoparticles. (b) Coercivity dependence on chromium doping. (c) Remnant magnetization dependence on chromium doping.

The coercivity represents the field strength needed to surpass the anisotropy barrier and to allow the magnetization of the nanoparticles to align with the field. This is shown by the Stoner-Wohlfarth theory

$$H_c = 2K/(\mu_o M_s) \tag{4.4.2}$$

where μ_o is the permeability of vacuum and M_s is the magnetic saturation[48]. Since the magnetic anisotropy is directly proportional to activation energy as well as coercivity, the hysteresis loop is expected to widen with increasing particle volume so for the purpose of determining the affect of chromium ion concentration on coercivity particle size was held constant at ~8 nm. The coercivity initially decreases with the weakening of Fe^{3+}-Fe^{3+} cross couplings between octahedral and tetrahedral sites upon the addition of any chromium. As the chromium content increases, magnetic anisotropy increases causing the field needed for alignment to be greater. At ~20% chromium doping, the coercivity decreases due to magnetic disorder introduced by Cr^{3+} large negative exchange constant. This exchange constant causes a loss of the magnetic parallel and antiparallel alignment that allows the spinel ferrite system to be antiferromagnetically ordered with an overall ferrimagnetic response.

4.5 Conclusions

A series of compositions in the system $MnFe_{2-x}Cr_xO_4$, where x= 0.0, 0.05, 0.13, 0.25, 0.43, 0.62, and 0.85 were synthesized via the In-Situ method. We have shown that the magnetic disorder and frustration is introduced to the spinel ferrite system with increasing Cr^{3+} concentration in the manganese ferrite nanoparticles and has extensive influence on the magnetic properties of these materials. These materials should continue to be investigated for their spin-orbital couplings, angular orbital momentum contribution to magnetic system and magnetic disorder and sperimagnetic systems properties.

CHAPTER 5

THE SOLVENT LONGEVITY FOR GREEN CHEMISTRY SYNTHESIS OF MAGNETIC FERRITES NANOPARTICLES

5.1 Abstract

Magnetic nanoparticles have increasingly shown potential in a variety of applications including catalysis support, biotechnology, and high-density data storage. It is desirable to produce high quality nanoparticles on the large scale through an environmentally benign green chemistry method. We have developed an aminolytic synthesis for the production of magnetic spinel ferrite nanoparticles. This procedure has the potential to be scaled up to an industrial level. The aminolytic reaction utilizes metal acetate and oleylamine reagents in a dibenzyl ether solvent. In fulfillment of green chemistry principles, all by-products can be recycled for re-utilization. Furthermore, the "mother" solution can be continuously used for multiple batches without treatment. Our trials have shown that the reaction could undergo ten reactions using the same solution without scarifying the quality or yield of the nanoparticulate product. The assessment of product quality was conducted using XRD combining with Rietveld analysis and SQUID magnetometry for magnetic properties.

5.2 Introduction

Magnetic materials research continues to attract attention because of their unique nanoscale properties. Magnetic nanoparticles are being utilized in everyday items and are considered the next step in the advancement of many current technologies[68a, 90]. These particles are found in a variety of applications such as computers and electronics, motor, toys, and many modern medical devices[65a, 91]. Magnetic nanoparticles have found using in medical applications such as targeted drug delivery[9, 90] and magnetic fluid hyperthermia[69]. Other uses for magnetic nanoparticles include media for high-density recording[64, 92], magnetocaloric refrigeration[93], and high-contrast magnetic resonance imaging[66, 94]. Since these particles can be utilized in wide range of applications, there is need for a synthesis methods appropriate for industrial production.

Developing industrial syntheses requires careful consideration by both the researcher and the company. Many issues need to be addressed during the scale up of any process including: bulk properties of the material, cost of the synthesis, the supply and demand of the product, as well as many others concerns such as reaction control. While most of these facets are economical in nature, one of the costs that has remained in the relatively hidden until recently are the environmental impacts of the synthesis. Due to increasing pressure on industry from the government and NGOs, companies are now striving to take measures to reduce their environmental impact in addition to helping their bottom line spending. This pressure for the consideration of the environmental impact has facilitated the growth and development of "Green Chemistry," which now lies firmly between the intersection of the laboratory and industry. While getting the highest yield out of any synthesis is a necessity, it is important to consider the extent of usefulness of the solvent, which is the focus of this experiment.

The aminolytic synthesis of nanoparticles is ideal for industrial scale use. This reaction method has many promising features including a relatively short synthesis time, low cost, stable acetate precursors, and high product yield. However, the high boiling solvent used in the synthesis is expensive and toxic which makes the utilization in an industrial setting less appealing. Focusing on this concern, we have examined the ability of the solvent to be used repeatedly in the same synthetic route, and subsequently analyzed the affect of solvent reuse on the quality and properties of the nanoparticles. Depending on the preference of the company, the synthesis may be suitable for continual production of magnetic nanoparticles with limited consideration of solvent consistency and saturation.

5.3 Experimental

5.3.1 Synthesis of Precursors

The metal acetate precursor was prepared by reacting metal hydroxide (Metal = Co, Fe) with acetic acid. $CoCl_2 \cdot 4H_2O$ (5 mmol) and $FeCl_3 \cdot 6H_2O$ (10 mmol) were dissolved in 100mL distilled water and stirred for one hour under ambient conditions. Upon the addition of 100mL of 1 M NaOH solution, a dark brown metal hydroxide precipitate formed. The mixture was stirred for another hour and then the precipitate was collected via centrifugation and was washed several times with distilled water. Metal hydroxide was dissolved with 30 mL of Glacial Acetic acid (99%) at 70 ˚C overnight. Upon complete evaporation of the liquid, a fine powder with a stoichemetric ratio of 1:2 mixture of $Co^{2+}(CH_3COO^-)_2$ and $Fe^{3+}(CH_3COO^-)_3$ was collected.

5.3.2 Synthesis of $CoFe_2O_4$ Nanoparticles

$CoFe_2O_4$ was synthesized via the aminolytic reaction. Pre-mixed metal acetate (7.5 mmol) was dissolved in a mixture of 10 mL of oleylamine and 40 mL of dibenzyl ether, and stirred for one hour. While purging with Ar, the turbid metal acetate solution was heated to 140 ˚C and the temperature was maintained for one hour. Then the temperature was raised to 240˚C at a ramping rate of 5˚C/min, and the reaction solution was agitated for another hour. Upon cooling to room temperature, the nanoparticles were separated with a magnetic field and washed using absolute ethanol. The used solvent was collected to form a “mother” solution. This procedure was repeated four times to generate enough used solvent to proceed with the study.

The aminolytic synthesis was repeated using the 40 mL of the “mother” solution and fresh reactants: oleylamine (10mL) with the premixed metal acetate (7.5mmol). The solvent was collected after each run and combined with the excess “mother” solution. This procedure was repeated for ten trials. TEM samples were prepared by dissolving ~6mg of nanoparticles into 10mL of hexanes.

5.4 Results and Discussion of Physical and Magnetic Properties

The powder X-ray diffraction pattern confirms that single phase $CoFe_2O_4$ nanoparticles with the spinel structure were synthesized via the aminolytic reaction using a metal-acetate precursor in a mixture of oleylamine and dibenzyl ether solvent. The sizes of the nanoparticles were calculated using Debye-Scherrer equation, which utilizes Bragg peak broadening data to calculate the average size of the nanoparticles. These average sizes were in good agreement to the sizes determined from the TEM micrographs (Figure 5.1).

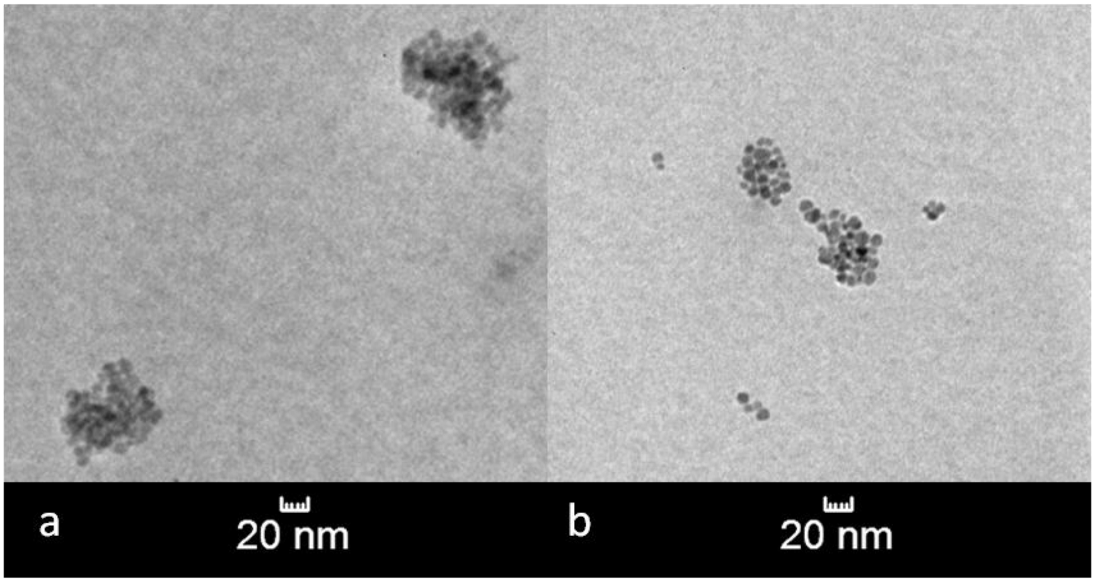

Figure 5.1. TEM micrograph of CoFe2O4 nanoparticles from (a) fresh solvent and (b) "mother" solution.

Rietveld analysis of the powder x-ray diffraction data was used to determine the impact of solvent recycling on the crystalline quality of the nanoparticles[55, 58]. The "goodness of fit" parameter, χ^2, was 1.228 and 1.366 for fresh solvent and tenth use of the "mother solution", respectively. This parameter measures the difference between the theoretical and experimental outcomes for the XRD patterns, and as the value approaches 1 it shows a minimization of the differences between the two outcomes within the error of the data. Fresh solvent and final use of the "mother" solution also had an $R(f^2)$ of 16.11% and 18.83%. $R(f^2)$ analyzes the model quality and determines the variance between measured structure factors squared and ideal structure factors squared. This value indicates the difference by percentages, with 0% being ideal. These results indicate that the experimental data agree well with the model. Thus these values and the difference curve shown in refinement plots (Figure5.2) indicate that the nanoparticle crystallinity is not degraded with the use of recycled solvent.

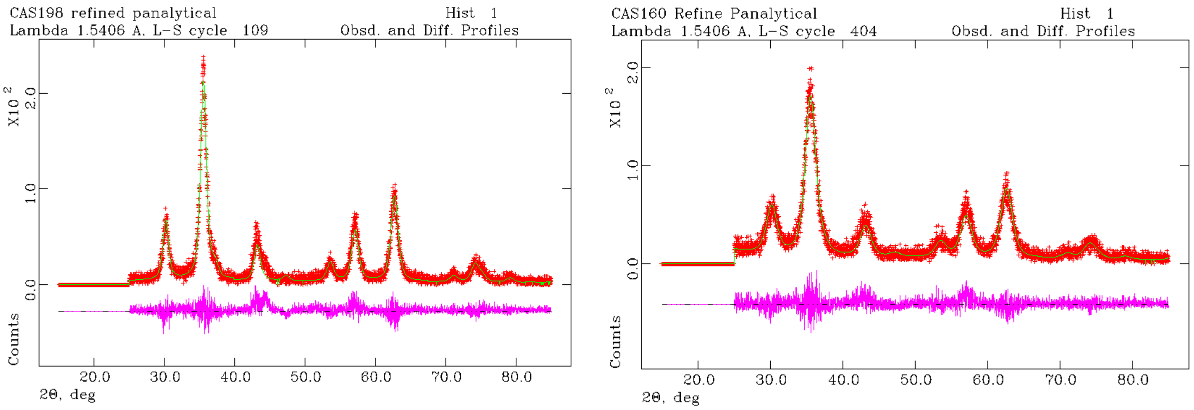

Figure 5.2. Rietveld refinement of powder XRDs for $CoFe_2O_4$ nanoparticles. CAS160 is the fresh solvent nanoparticles and CAS198 is the “mother” solution nanoparticles. The goodness of fit parameters are 1.228 and 1.366 respectively for χ^2 and 16.11% and 18.83% for $R(f^2)$ respectively.

Figure 5.3 is H^1 NMR was performed on the “mother” solution. The amine peak at 1.1ppm in dichloromethane solvent disappeared with the completion of the reaction but an acetate peak was found at 1.9ppm. This indicates that fresh oleylamine does need to be added with each reuse because it is a reactant.

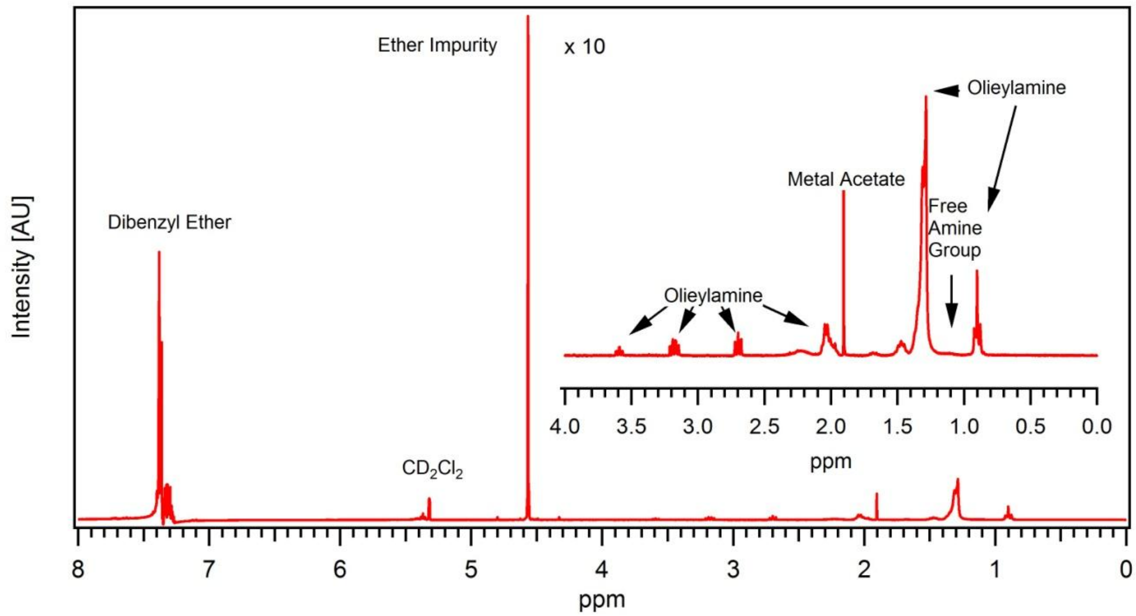

Figure 5.3. H^1NMR of “mother” solution take in CD_2Cl_2.

Magnetic properties of $CoFe_2O_4$ nanoparticles were measured by a Quantum Design MPMS 5S SQUID magnetometer with a magnetic field up to 5T. Figure 5.4 is a plot of blocking temperature of nanoparticles with respect to their diameter. The open circles represent particles from clean solvent and the open squares are particles from the “mother” solution. As expected the two sets of data trend well with each other. The energy barrier (E_A) for uncoupling of magnetization orientation in a single domain particle has been described by the Stoner- Wohlfarth theory and is given by

$$E_A = KV\sin^2\Theta \qquad (5.4.1)$$

Where K is the anisotropy of the material, V is the volume of the nanoparticle, and Θ is the angle between an applied magnetic field and the easy axis of a nanoparticle. The blocking temperature of a materials is the temperature at which the moments of the nanoparticle are no longer blocked and are able to overcome the energy barrier, E_A[48]. Since the blocking temperature increases at the same ratio as increasing nanoparticle size for both the fresh solvent nanoparticles and "mother" solution nanoparticles, we conclude that the bulk magnetic properties are unaffected by solvent reuse as susceptibility measurement correlate closely with bulk magnetic properties[4].

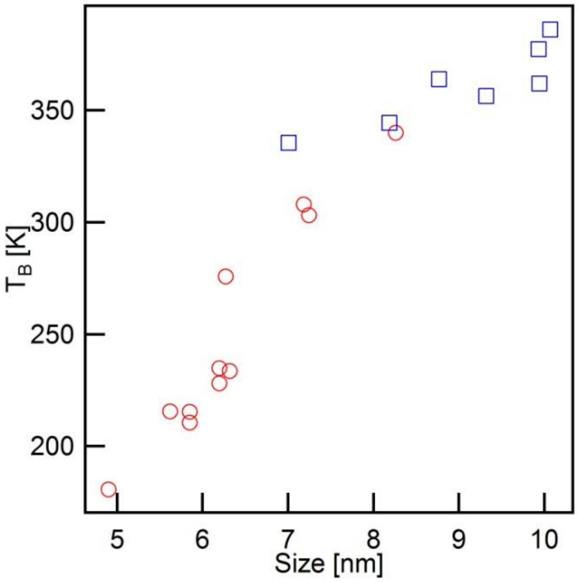

Figure 5.4. Size dependence of Blocking Temperature (T_B) for $CoFe_2O_4$ nanoparticles. Open circles are the fresh solvent synthesis and open squares are utilizing the "mother" solution.

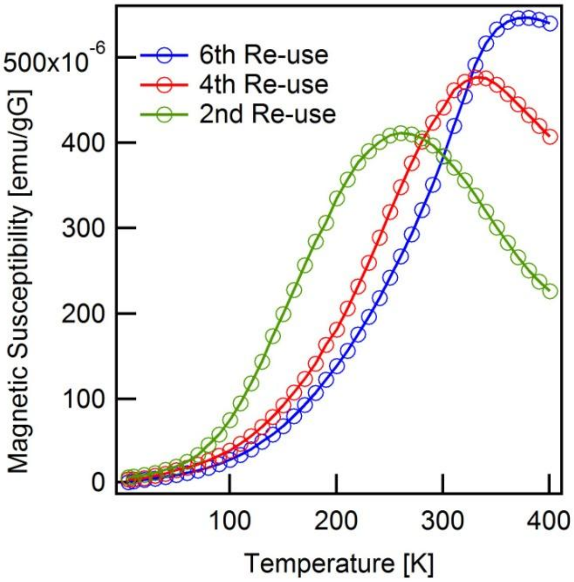

Figure 5.5. Temperature dependent magnetization of $CoFe_2O_4$ produced with the "mother" solution.

Figure 5.5 is temperature dependent magnetic susceptibility measurements at 100G of nanoparticles produced by increasing reuses of the "mother" solution. As seen, the susceptibility graph increases in intensity and the peak shifts to higher temperature with the subsequent reuse of the "mother" solution. This can be explained by the increase in particle size that also occurs with each reuse due to the leftover precursor in the "mother" solution. Also, small nanoparticles could be forming during the first few reactions and are not removed during the magnetic separation due to their small response to applied magnetic field. These nanoparticles would be acting a seed particles during later reactions and encourage larger particle growth than is normally obtained by the aminolytic method.

Field dependent magnetization measurements at 5 K show hysteresis curve for a fresh synthesis and the ninth reuse of the "mother" solution in Figure 5.6. The two curves are almost identical and show expected behavior for $CoFe_2O_4$ nanoparticles.

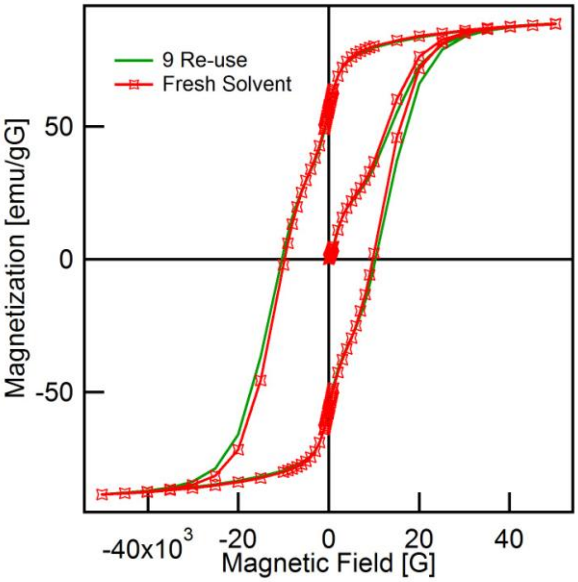

Figure 5.6. Overlaid hysteresis curves of $CoFe_2O_4$ nanoparticles at 5 K.

The remnant magnetization and saturation magnetization increase with increasing particle size (Figure 5.7). Again the open circles indicate clean solvent synthesis and the open squares, “mother” solution synthesis. The data from the two synthesis conditions trend well together indicating that the bulk and surface magnetic properties are maintained during the solvent longevity study. The presence of surface anisotropy can account for the effects of symmetry reduction caused by incomplete coordination sphere at nanoparticle surface as proposed by Néel. The surface anisotropy (K_s) of a nanoparticle contributes to the total magnetic anisotropy as

$$K = K_{xtal} + (6/d)\, K_s \tag{2}$$

where K_{xtal} is the bulk magnetocrystalline anisotropy and d is the diameter of the particle[48]. Since there are two major factors are contributing to the coercivity strength over this size range for single domain particles, surface and bulk magnetocrystalline anisotropy, the strong correlation between the two studies indications the production of high quality nanoparticles with both synthesis[4]. The coercivity represents the field strength needed to surpass the anisotropy barrier and to allow the magnetization of the nanoparticles to align with the field. This is shown by the Stoner-Wohlfarth theory

$$H_c = 2K/(\mu_o M_s) \qquad (3)$$

where μ_o is the permeability of vacuum and M_s is the magnetic saturation[48]. Since the magnetic anisotropy is directly proportional to activation energy as well as coercivity, the hysteresis loop is expected to widen with increasing particle volume. However, if the surface characteristic dominate the anisotropy calculation as expected in small particles, the field require for alignment will be less for decreasing surface area that accompanies increasing particle size[4, 75].

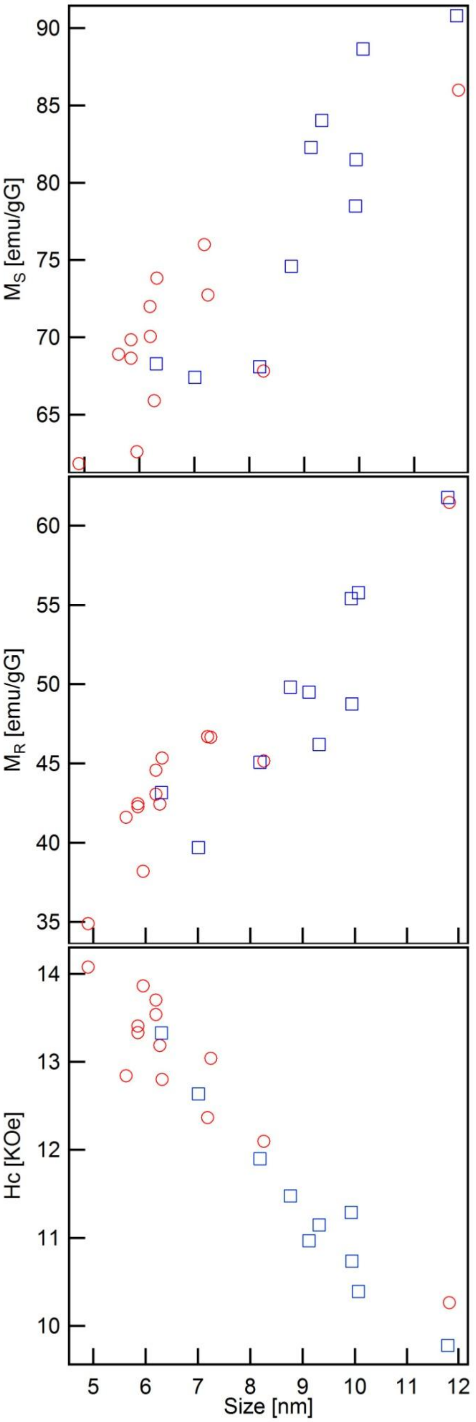

Figure 5.7. (a) Size dependence of saturation magnetization for $CoFe_2O_4$ nanoparticles. (b) Size dependence of remnant magnetization. (c) Size dependence of coercivity. Open circles are the fresh solvent synthesis and open squares are utilizing the “mother” solution.

5.5 Conclusions

We have shown that the reuse of the aminolytic method's high boiling solvent, dibenzyl ether, has no affect on the magnetic and crystalline properties of the synthesis cobalt ferrite nanoparticles. This low waste procedure is an important step in the search for scalable nanoparticle synthesis.

CHAPTER 6

SYNTHESIS AND CHARACTERIZATION OF DIFFERENT PHASE IRON OXIDES AND OXY-HYDROXIDES NANOPARTICLES

6.1 Abstract

In 2001 the Environmental Protection Agency (EPA) lowered the maximum level of contaminant (MCL) of arsenic in current water system from 50 ppb to 10 ppb[95]. Studies indicate that up 10% of US municipal systems will have to be revamped to meet these increased standards. Iron oxides and iron oxy-hydroxides show a high affinity for arsenic in aqueous media. There are many forms of iron oxides and most of these structures are used in arsenic removal techniques. The iron oxide is formed in-situ by adding a non-oxide iron source to water. The exact nature of the arsenic binding and the effect of impurities on binding efficiency are not well known. Synthesizing well characterized iron oxides will afford better understanding of the arsenic surface binding. Better understanding of the binding affinity for arsenic is necessary for the incorporation of iron oxides into the best available technologies (BATs). Several nanometer sized samples of goethite (α-FeO(OH)), maghemite (γ-Fe_2O_3), magnetite (Fe_3O_4), and hematite (α-Fe_2O_3) were synthesized and characterized using XRD, SQUID, PAS-IR, EDS, and TEM.

6.2 Introduction

There are many structures of iron oxides and most of these structures are used in arsenic removal techniques. The iron oxide is formed in-situ by adding a non-oxide iron source to water. The exact nature of the arsenic binding and the effect of impurities on binding efficiency are not well known[96]. Synthesizing well characterized iron oxides will afford better understanding of the arsenic surface binding. This information on binding affinity for arsenic is necessary for the incorporation of iron oxides into BATs.

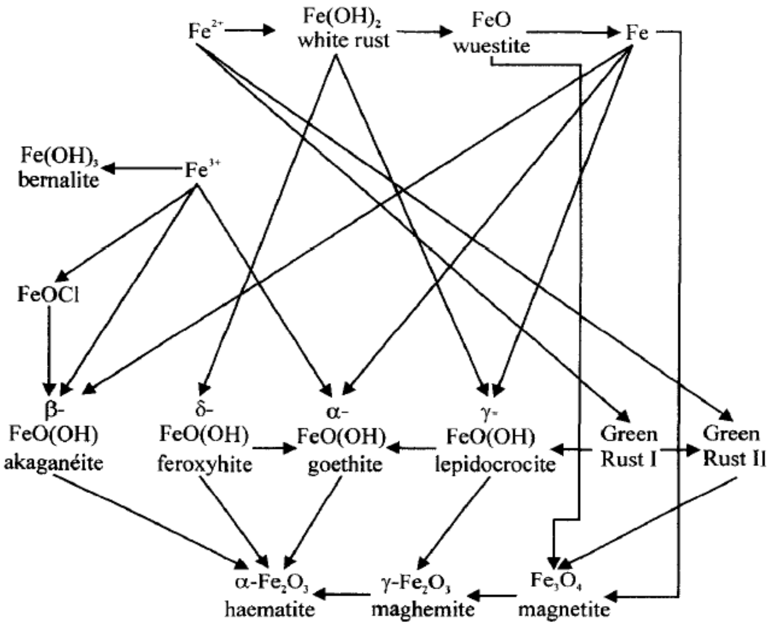

Figure 6.1. Relationships between iron phases[97].

The phases of iron oxides, as shown in Figure 6.1, were chosen to be synthesized based to the following criteria: promise shown in the literature[98], are products of iron's reaction with water, are stable in ambient conditions, and have useful magnetic properties. These phases are alpha oxy-hydroxide (goethite), gamma oxy-hydroxide (lepidocrocite), alpha oxide (hematite), gamma oxide (maghemite), and mixed oxidation state oxide (magnetite). All of these phases were successfully synthesized except for lepidocrocite.

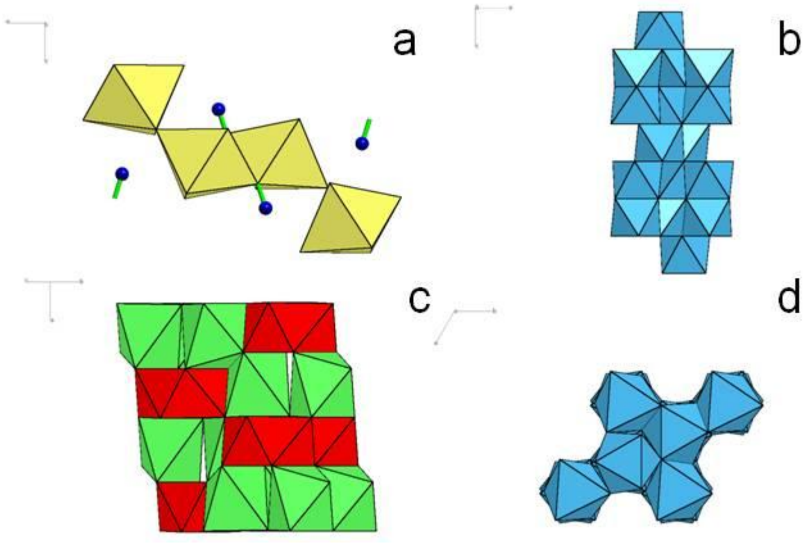

Figure 6.2 Unit cells of (a) goethite, (b) maghemite, (c) magnetite, and (d) hematite

The iron oxides that were synthesized for this project are naturally occurring minerals in the earth's crust. Ferrihydrite is a metastable mineral and usually a precursor to goethite. Goethite (α-FeO(OH)) has an orthorhombic structure which originates from ramsdellite and can be seen as a single direction compression that flattens the tunnels in the structure so they are just large enough to accept H (Figure 6.2a). Maghemite (γ-Fe_2O_3) and magnetite (Fe_3O_4) share the same inverse spinel ferrite structure and are both magnetic in nature (Figure 6.2b&c). Hematite (α-Fe_2O_3) is a corundum structure that has hexagonal closed packed array of oxygen atoms in one layer and the Fe^{3+} ions placed in 67% of the octahedral holes (Figure 6.2d)[99]. This gives it antiferromagnetic ordering [100,45].

6.3 Experimental

6.3.1 Synthesis of Goethite (α-FeO(OH))

Goethite nanoparticles were synthesized via a previously reported method by Thies-Weesie[101]. In summary, iron nitrate (25 mmol) was dissolved in distilled water then precipitated out as iron hydroxide via the addition of base. The solid was then re-dissolved in a basic solution and allowed to age for an hour. The solution was heated to above room temperature (~60˚C) and stirred for three days. The reaction was cooled to room temperature while maintaining agitation for another three days. The solid produced was collected via centrifugation and washed with distilled water. The product was dried in air and analyzed as produced.

6.3.2 Synthesis of Maghemite (γ-Fe_2O_3)

Maghemite nanoparticles were synthesized via the aminolytic reaction. Iron (III) acetate was dissolved in a mixture of 10 mL of oleylamine and 40 mL of dibenzyl ether, and stirred for one hour. While purging with Ar, the turbid metal acetate solution was heated to 140˚C and the temperature was maintained for one hour. Then the temperature was raised to 240˚C at a ramping rate of 5˚C/min, and the reaction solution was agitated for another hour. Upon cooling to room temperature, the nanoparticles were separated with a magnetic field and washed using absolute ethanol.

6.3.3 Synthesis of Magnetite (Fe_3O_4)

Magnetite nanoparticles were synthesized via the aminolytic reaction. Pre-mixed iron (II) and iron (III) acetate were dissolved in a mixture of 10 mL of oleylamine and 40 mL of dibenzyl ether, and stirred for one hour. While purging with Ar, the turbid metal acetate solution was heated to 140˚C and the temperature was maintained for one hour.

Then the temperature was raised to 240˚C at a ramping rate of 5˚C/min, and the reaction solution was agitated for another hour. Upon cooling to room temperature, the nanoparticles were separated with a magnetic field and washed using absolute ethanol.

6.3.4 Synthesis of Hematite (α-Fe_2O_3)

Hematite nanoparticles were synthesized via the water-in-toluene reverse micelle method[87]. In summary, iron (III) chloride (15 mmol) was dissolved in distilled water. The inorganic phase was combined with a sodium docdecylbezenesulfonate (NaDBS) (0.4 M) solution. This is followed by the addition of a large amount of toluene. The volume ratio of water and toluene determines the size of the hematite particles. The mixture was stirred until it became a single phase containing micelles (~4 hrs). Methylamine was added to precipitate the nanoparticles, followed by refluxing the solution for several hours. After the solution settled, the particles were separated by centrifugation and washed with distilled water. The dried powder was heated to 600˚C at a ramping rate of 5˚C/ min for ~22 hours.

6.4 Results and Discussion

6.4.1 Physical and Magnetic Properties of Goethite (α-FeO(OH))

The powder X-ray diffraction pattern confirms that single phase goethite nanoparticles (ICDD File Number 29-713) with the orthorhombic structure were synthesized is shown in Figure 6.3. The average sizes of the nanoparticles were calculated using Debye-Scherrer equation which utilizes Bragg peak broadening data. Since the particles are lathlike, the size determined from the XRD patterns (~15 nm) was an average of all the dimensions thus TEM micrographs were used to determined a more realistic average length and width of the particles (~15 nm by ~185 nm) (Figure 6.4). The dimensions of the nanorods are best controlled by the stirring rate.

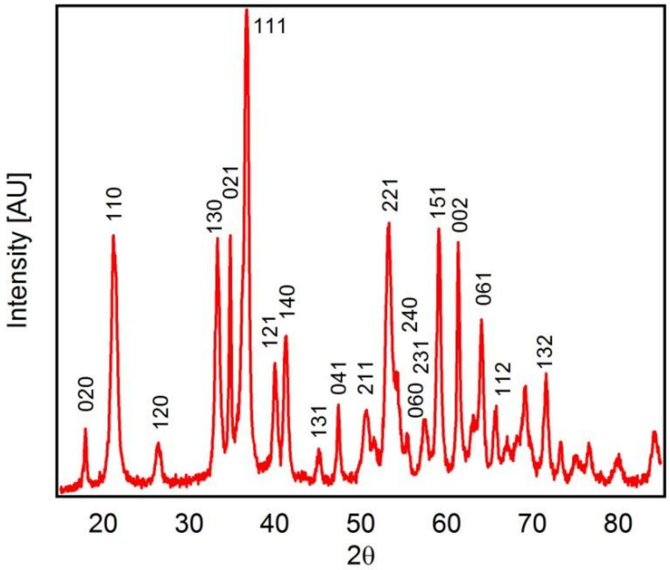

Figure 6.3. Powder XRD pattern for goethite nanoparticles.

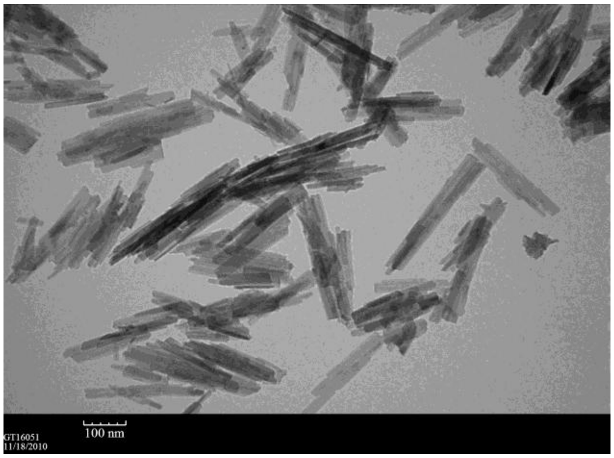

Figure 6.4. TEM micrograph of goethite nanoparticles

The magnetic properties of goethite nanoparticles were measured by a Quantum Design MPMS 5S SQUID magnetometer with a magnetic field up to 5 T. The nanoparticles are not very responsive to an applied magnetic field and this is confirmed by the magnetic susceptibility measurement near zero at room temperature graphed in Figure 6.5.

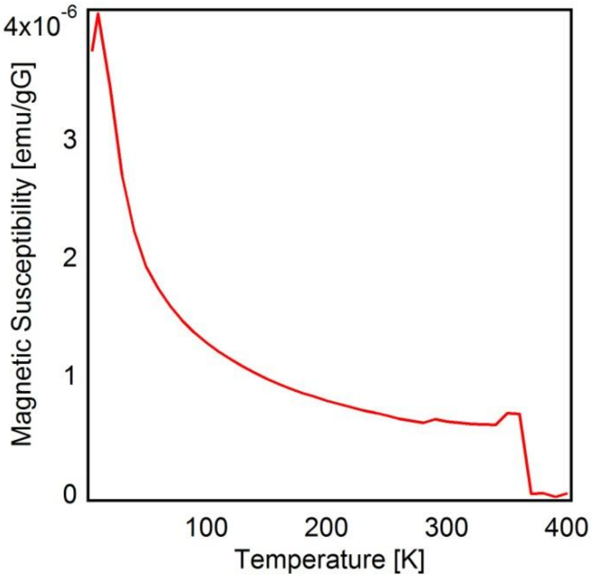

Figure 6.5. Temperature dependent magnetization of goethite nanoparticles

The goethite nanoparticles showed very little response to a changing magnetic field as shown in Figure 6.6. Magnetic Saturation is very low and the materials have almost no magnetic memory. The coercive field required is small (~280 Oe). Photoacoustic IR (PAS-IR) was also performed on the nanoparticle sample and the spectrum corresponds well with published literature (Figure 6.7). Especially, evident are the characteristic hydroxide in- and out-of-plane scissoring peaks at ~890 and 800 wavenumbers. The vibrations of the bulk Fe-OH bonds, $\upsilon_{1,}$ is seen at ~3140 wavenumbers[102].

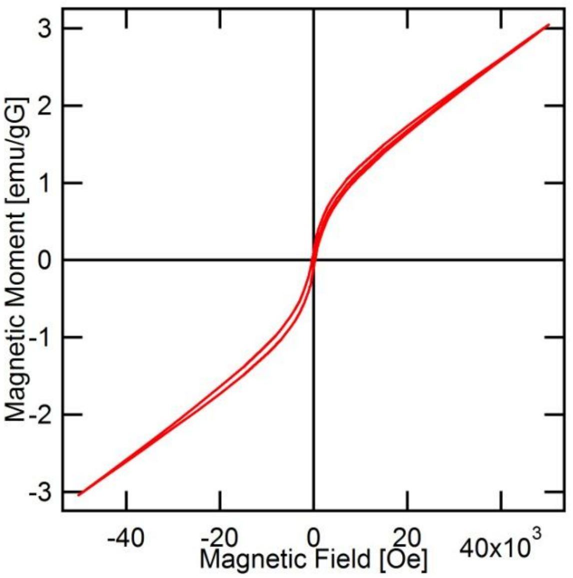

Figure 6.6. Hysteresis curve of goethite nanoparticles at 5 K.

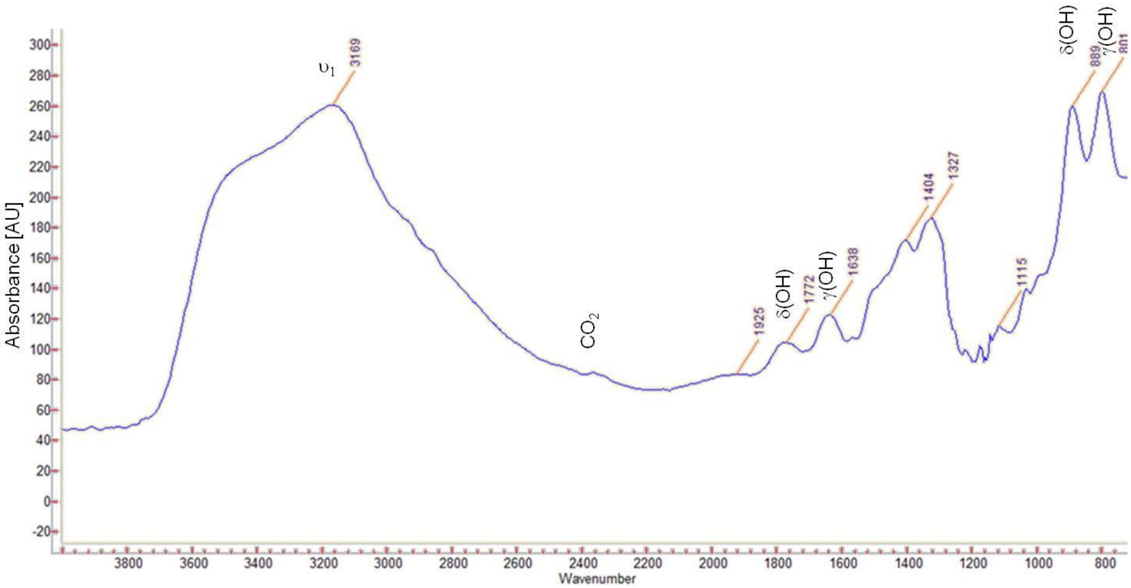

Figure 6.7. PAS-IR Absorbance spectrum for goethite nanoparticles.

Finally, Energy Dispersive X-ray Spectroscopy (EDS) was performed on the goethite nanoparticles. The spectrum shown in Figure 6.8 indicates that no non-crystalline impurities were found in the sample that would not have appeared in the XRD pattern. The copper and carbon found correspond to the carbon coated copper grid that the measurement was performed on.

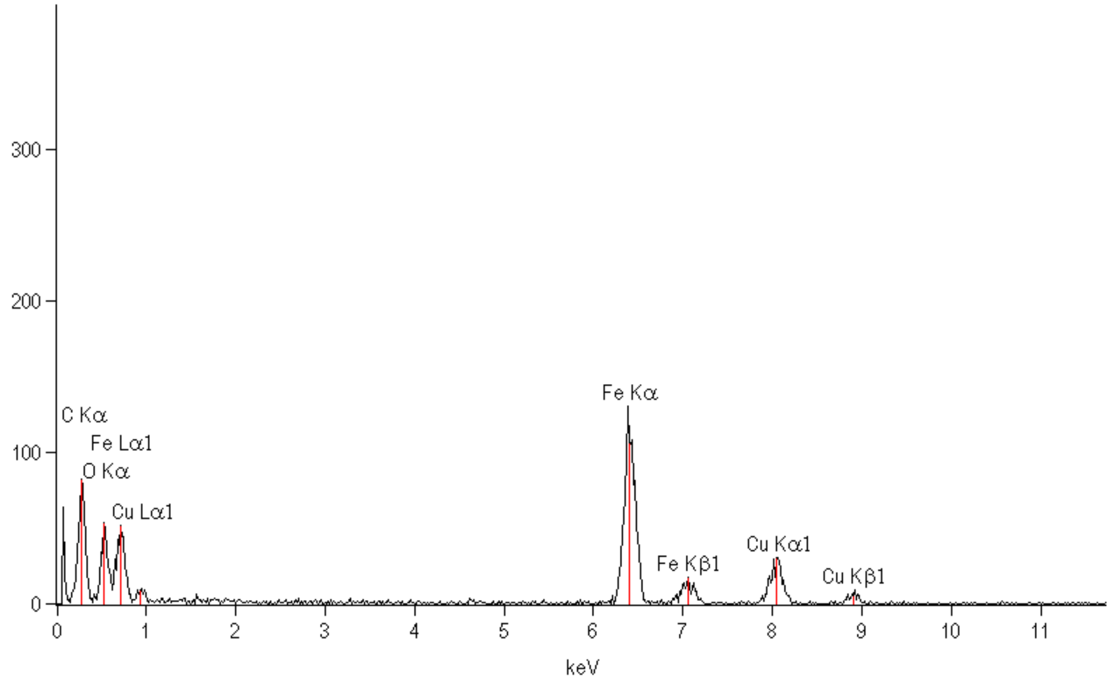

Figure 6.8. EDS spectrum of goethite nanoparticles.

6.4.2 Physical and Magnetic Properties of Maghemite (γ-Fe_2O_3)

The powder XRD pattern that confirms that maghemite nanoparticles (ICDD File Number 39-1346) with the spinel structure were synthesized is shown in Figure 6.9. The arrows indicate an impurity phase that corresponds to hematite. All maghemite nanoparticles had some degree of hematite impurity present. The average sizes of the nanoparticles were calculated using Debye-Scherrer equation. Since the particles are quasi spherical, this average size correlates well with the size calculated from the TEM micrographs (Figure 6.10). Shown in Figure 6.11, full conversion to hematite from maghemite was observed at 550˚C; these measurements were performed on the Bruker

D8 Advantage XRD with a heat stage. A layer of particles were deposited by evaporation then heated at 50˚C interval and a 30 minute scan was preformed.

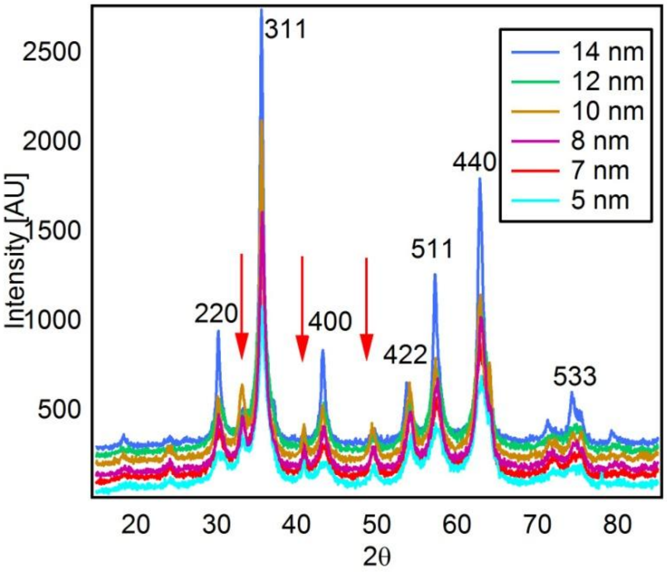

Figure 6.9. Powder XRD pattern for maghemite nanoparticles.

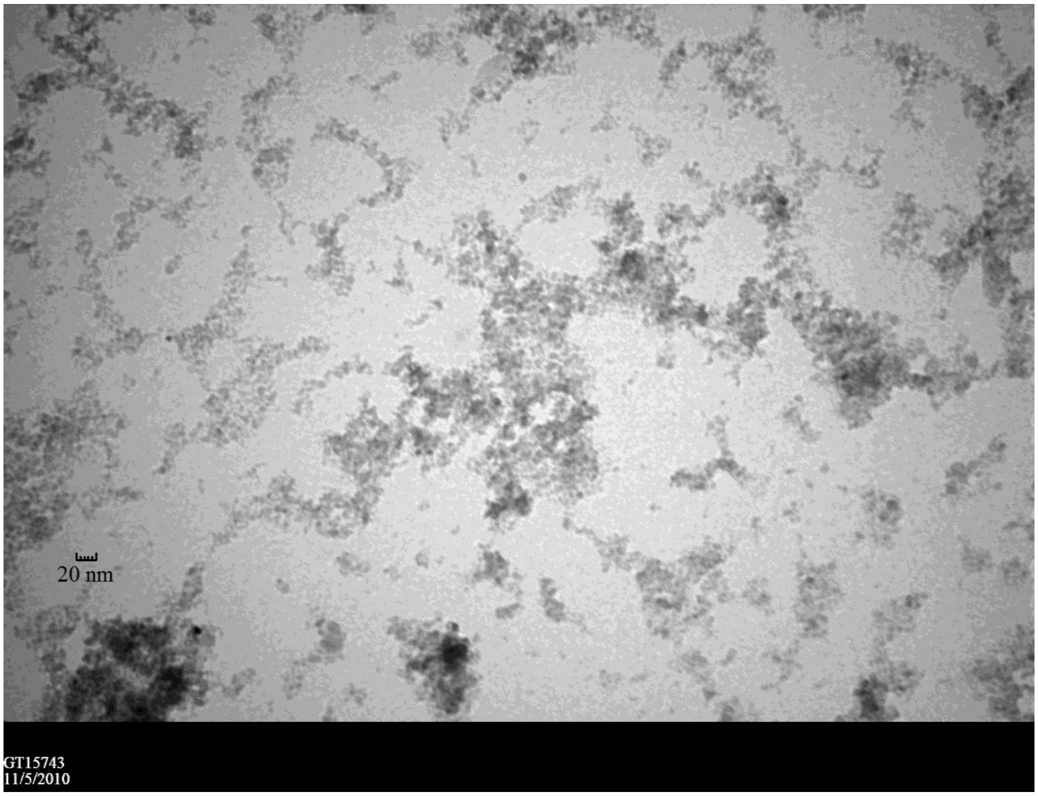

Figure 6.10. TEM micrograph of ~ 8 nm maghemite nanoparticles

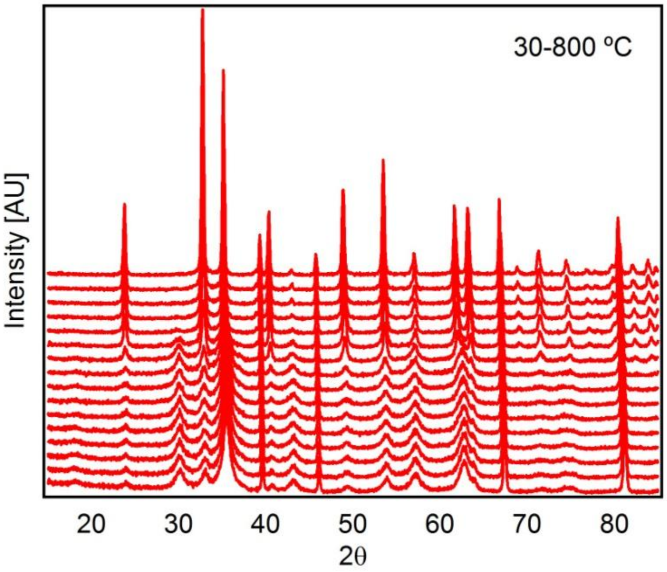

Figure 6.11. XRD pattern stack plot showing conversion from maghemite to hematite

The magnetic properties of maghemite nanoparticles were measured by a SQUID magnetometer. The nanoparticles are very responsive to an applied magnetic field and this is confirmed by the magnetic susceptibility measurement in the superparamagnetic range at room temperature graphed in Figure 6.12.

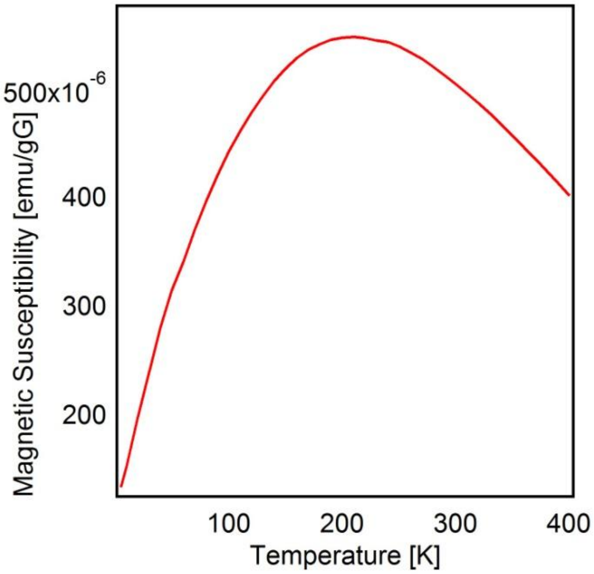

Figure 6.12. Temperature dependent magnetization of maghemite nanoparticles

Maghemite nanoparticles were responsive to a changing magnetic field as shown in Figure 6.13. Responses close to magnetic saturation are obtained with a one tesla field and higher. The material also displays very little memory and coercivity. These properties make the material ideal for magnetic separations. Photoacoustic IR (PAS-IR) was also performed on the nanoparticle sample (Figure 6.14). The large peak at ~3400 wavenumbers corresponds to surface OH singly coordinated to iron and will be seen in all the PAS-IR spectra of the iron oxides in this chapter[102].

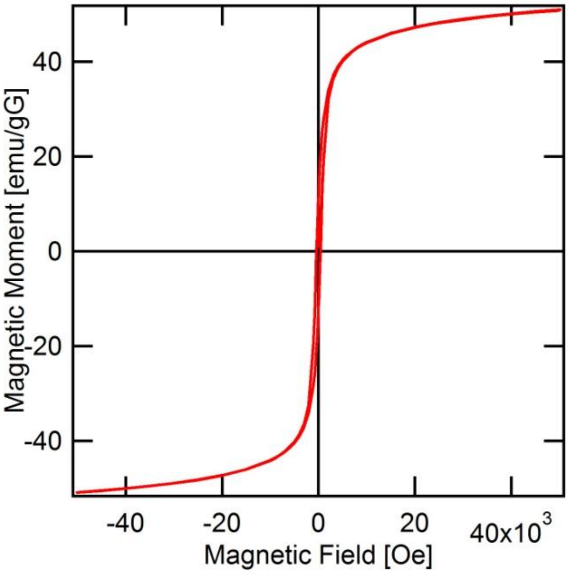

Figure 6.13. Hysteresis curve of maghemite nanoparticles at 5 K.

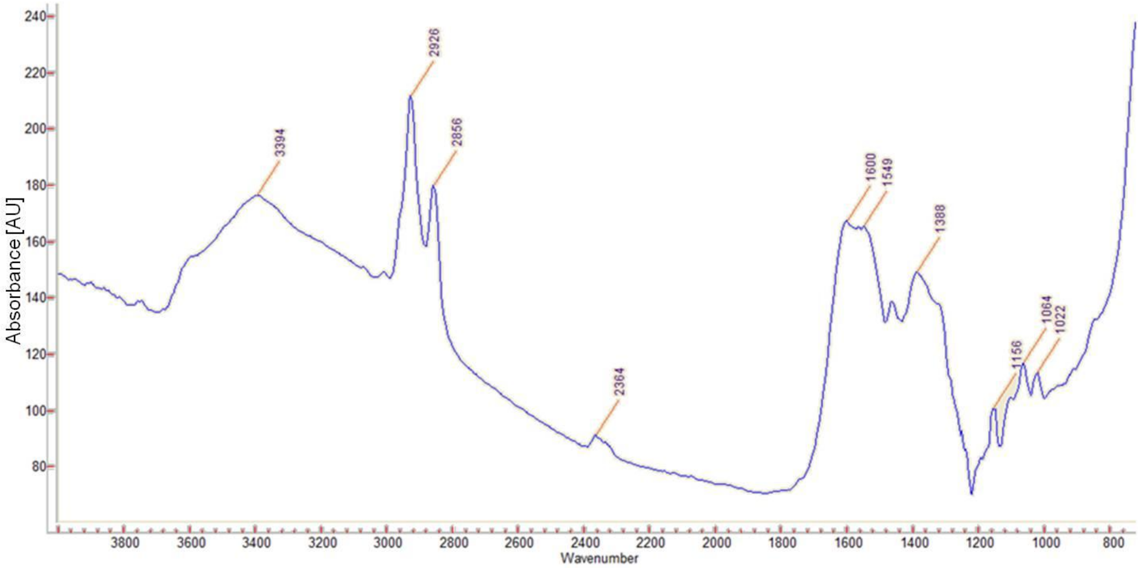

Figure 6.14. PAS-IR Absorbance spectrum for maghemite nanoparticles.

Finally, EDS was done on the maghemite nanoparticles. The spectrum shown in Figure 6.15 indicates that there are no impurities in the sample that would not have appeared in the XRD pattern. The silicon peak correlates to some scattered electrons striking the detector which sometimes occurs with high energy electron beam.

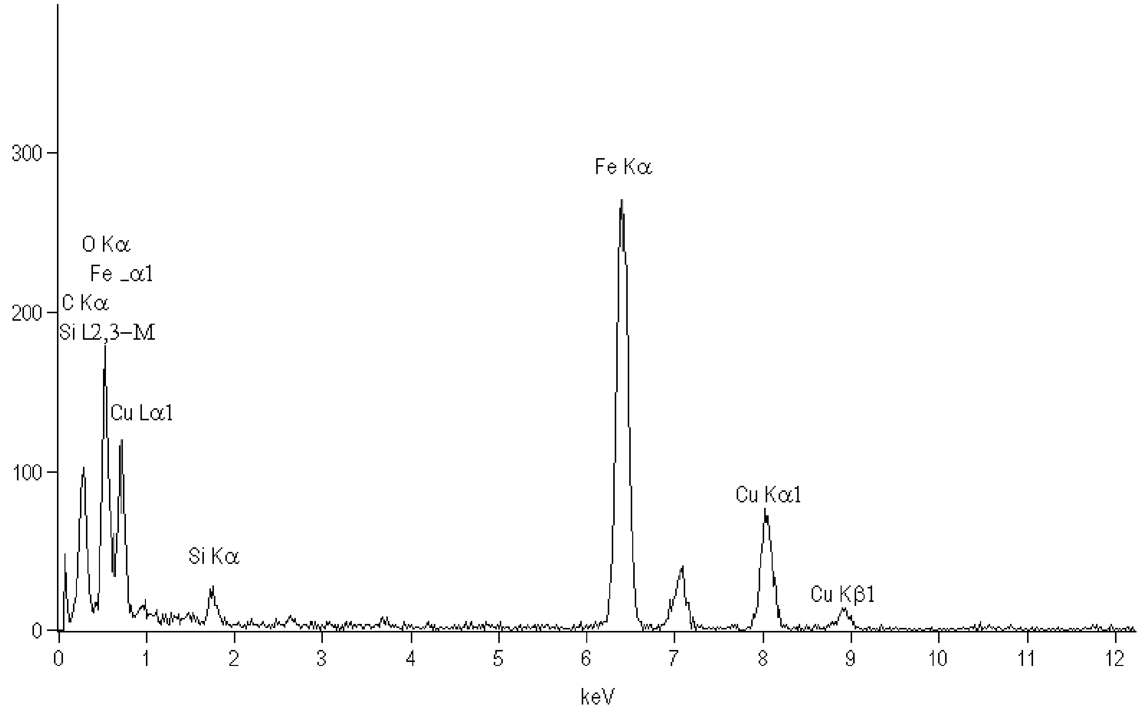

Figure 6.15. EDS spectrum of maghemite nanoparticles.

6.4.3 Physical and Magnetic Properties of Magnetite (Fe_3O_4)

Figure 6.16 shows the powder XRD pattern of magnetite nanoparticles (ICDD File Number 19-629). According to the Debye-Scherrer equation, the average size of the nanoparticles was found to be ~7 nm. This average size correlates well with the size calculated from the TEM micrographs (Figure 6.17).

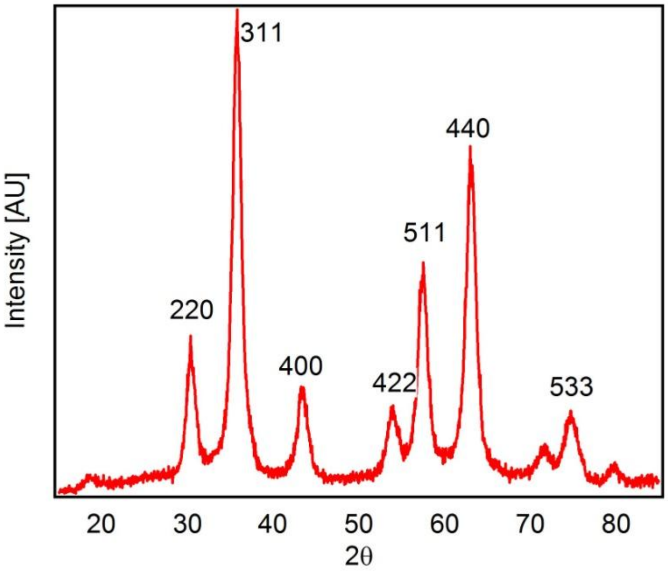

Figure 6.16. Powder XRD pattern for magnetite nanoparticles.

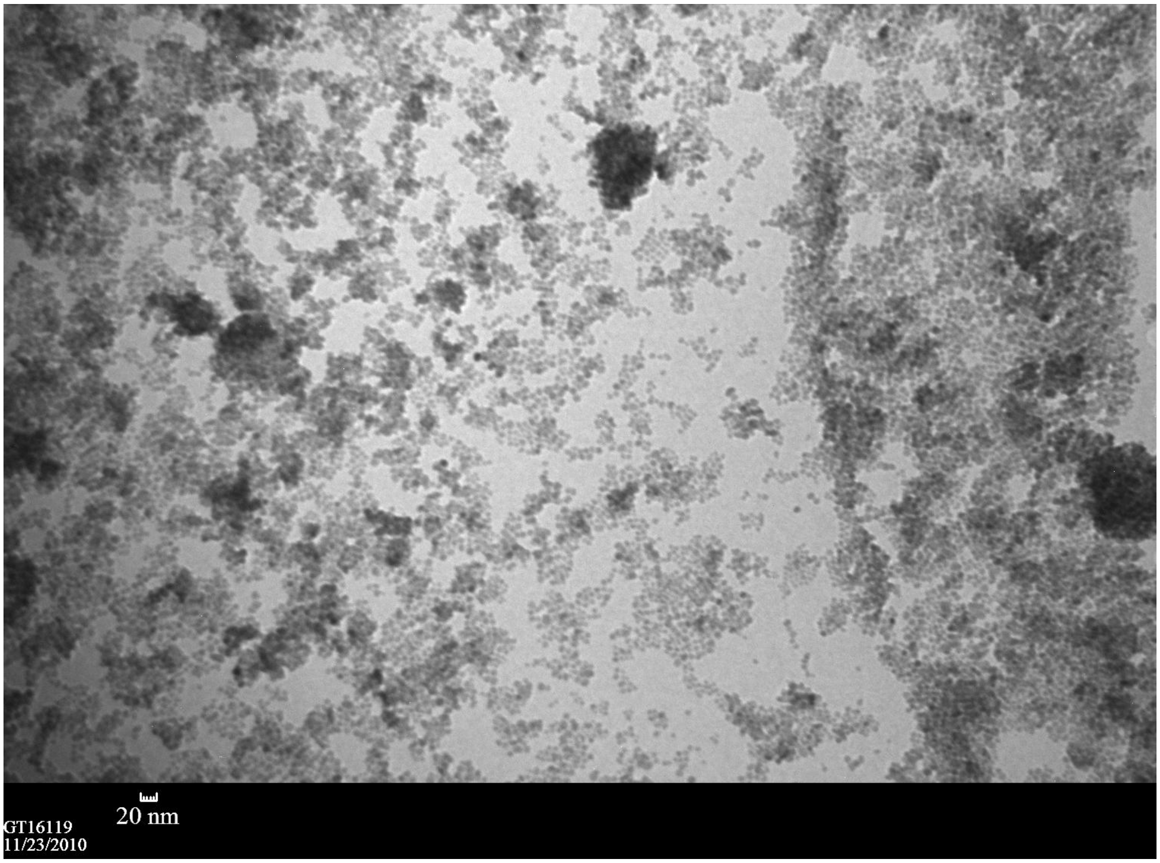

Figure 6.17. TEM micrograph of magnetite nanoparticles

The magnetic properties of magnetite nanoparticles were taken. These nanoparticles were also found to be very responsive to an applied magnetic field which is confirmed by the magnetic susceptibility measurements in the superparamagnetic range at room temperature graphed in Figure 6.18.

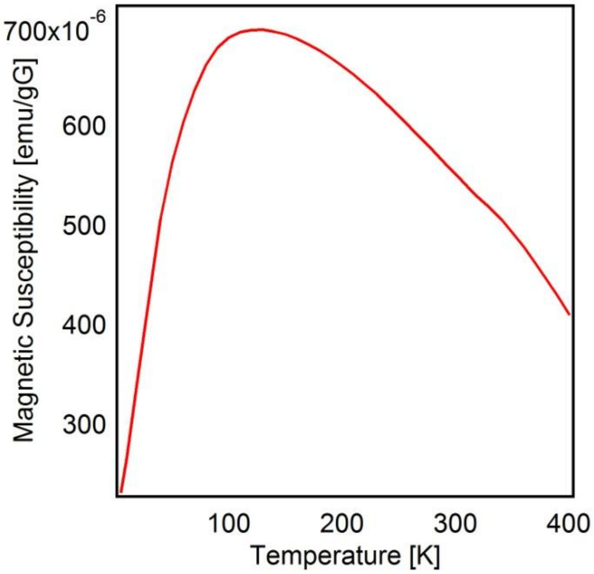

Figure 6.18. Temperature dependent magnetization of magnetite nanoparticles

Magnetite nanoparticle responded to a changing magnetic field as shown in Figure 6.19. Though the magnetic saturation is very high, the material has almost no magnetic memory or coercivity (~230 Oe). PAS-IR was also performed on the nanoparticle sample (Figure 6.20).

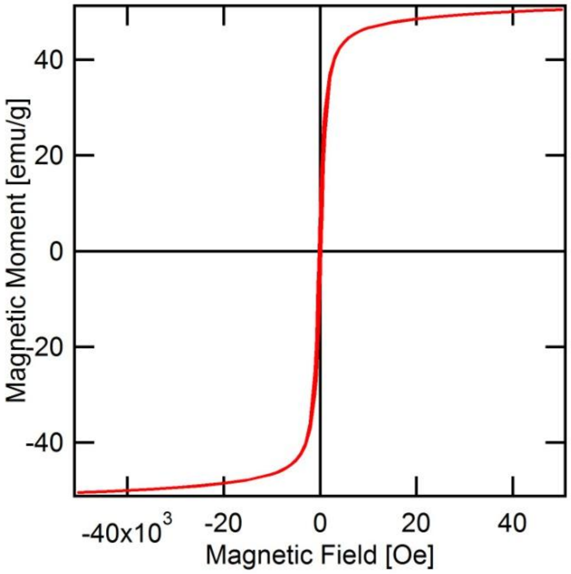

Figure 6.19. Hysteresis curve of magnetite nanoparticles at 5 K.

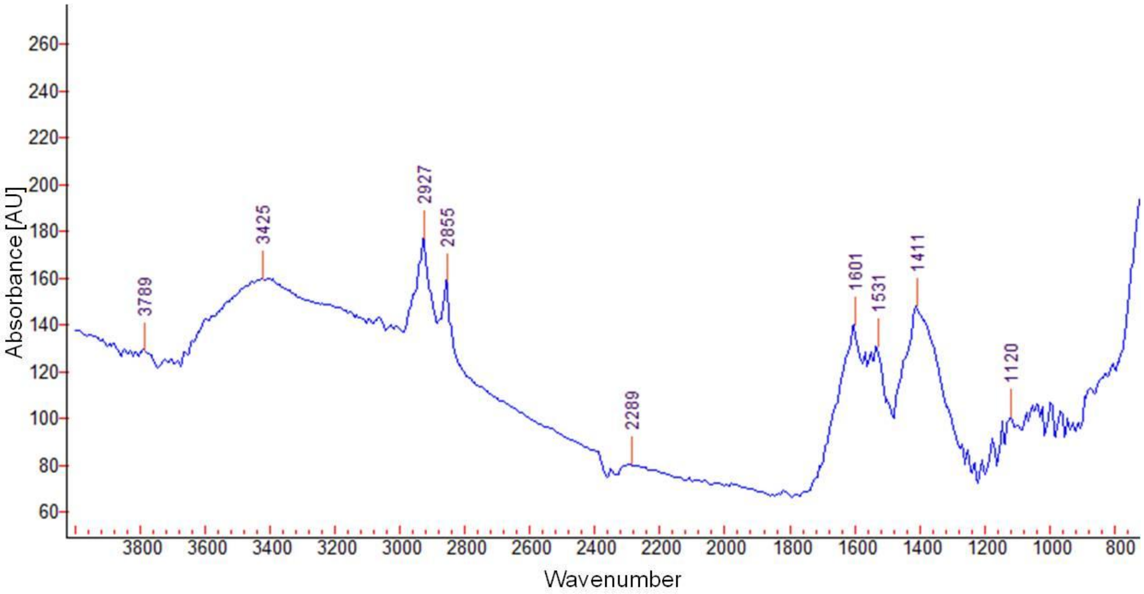

Figure 6.20. PAS-IR Absorbance spectrum for magnetite nanoparticles.

Again, EDS was performed on the magnetite nanoparticles. The spectrum shown in Figure 6.21 indicates the absence of impurities in the sample that would have been missed in the XRD pattern.

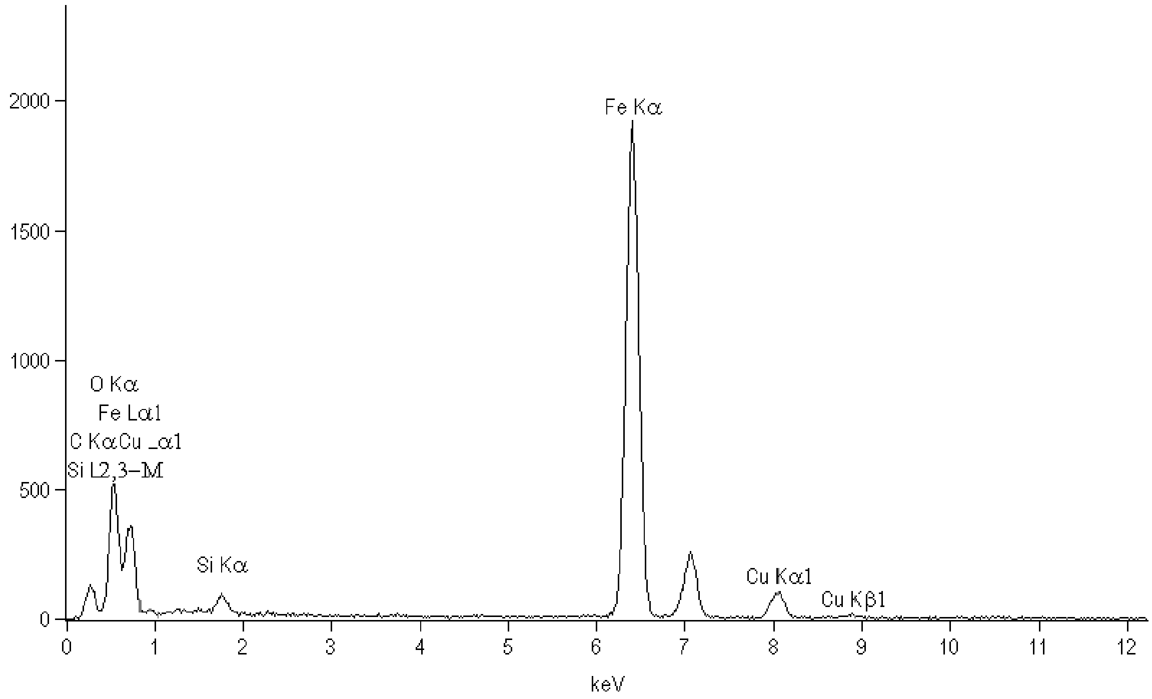

Figure 6.21. EDS spectrum for magnetite nanoparticles.

6.4.4 Physical and Magnetic Properties of Hematite (α-Fe_2O_3)

The powder XRD pattern in Figure 6.22 confirms that single phase hematite nanoparticles (ICDD File Number 47-1409) with the rhombohedral structure were synthesized. The average sizes of the nanoparticles were calculated. Since the particles are a mix of rods and spheres, the size determined from XRD pattern (~22 nm) was an average of all the dimensions so TEM micrographs were used to determined a more realistic average length and width of the particles (~20 nm by ~170 nm) of the nanorods and an average size for the spherical particle (~18 nm) (Figure 6.23). Again, the dimensions of the nanorods are best controlled by the stirring rate and the water to toluene ratio. These were adjusted to produce batches of just spherical particles.

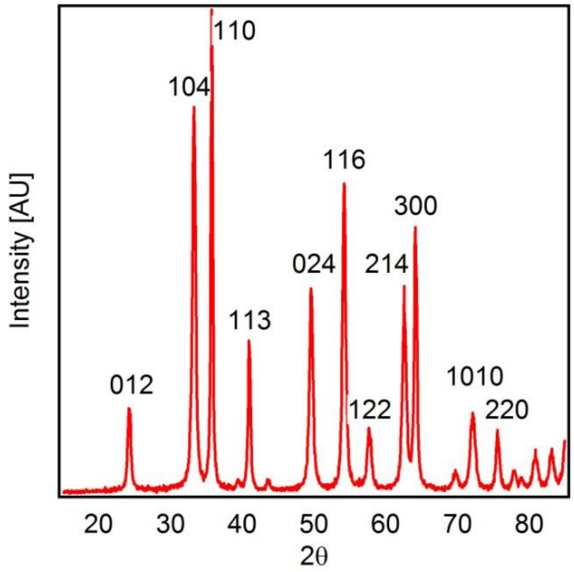

Figure 6.22. Powder XRD pattern for hematite nanoparticles.

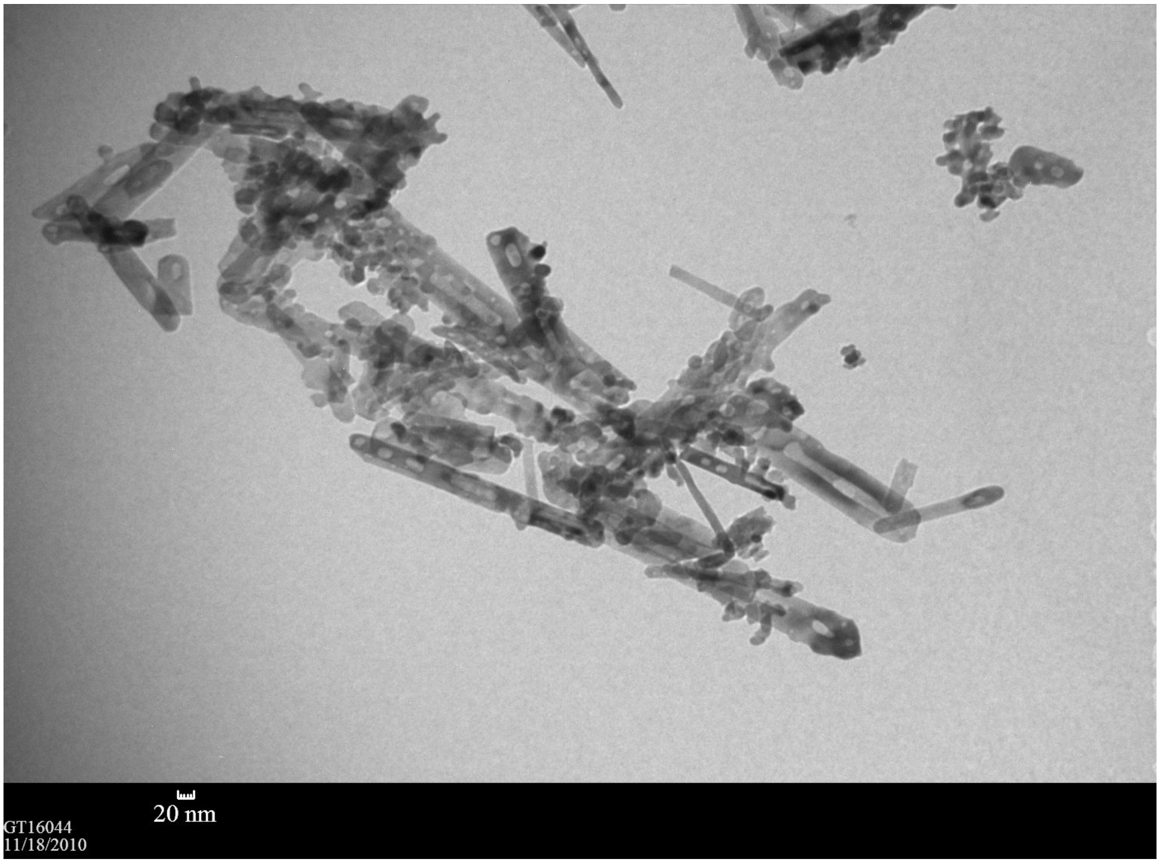

Figure 6.23. TEM micrograph of hematite nanoparticles

The magnetic properties of hematite nanoparticles were obtained. The nanoparticles show antiferromagnetic behavior below the Morin transition temperature (T_M) then the magnetic response increases as the amount of thermal energy in the system starts overcome the couplings. Between T_M of ~ 256 K and the Néel Temperature (T_N) of ~961 K , hematite is weakly ferromagnetic[103]. This is shown in Figure 6.24 by the increase in magnetic response at around 300 K. This system is not very responsive to an applied magnetic field at room temperature.

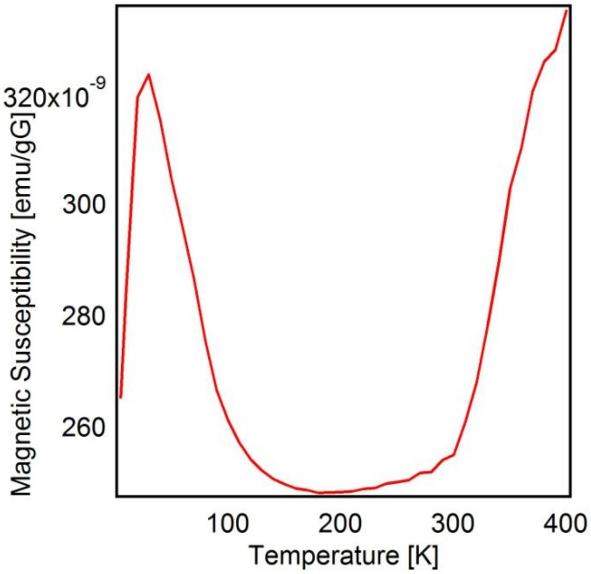

Figure 6.24. Temperature dependent magnetization of hematite nanoparticles

Hematite nanoparticles showed very little response to a changing magnetic field as shown in Figure 6.25. Magnetic saturation is very low and the material has almost no remnant magnetization. The coercive field required is ~2220 Oe. PAS-IR was also performed on the nanoparticle sample (Figure 6.26).

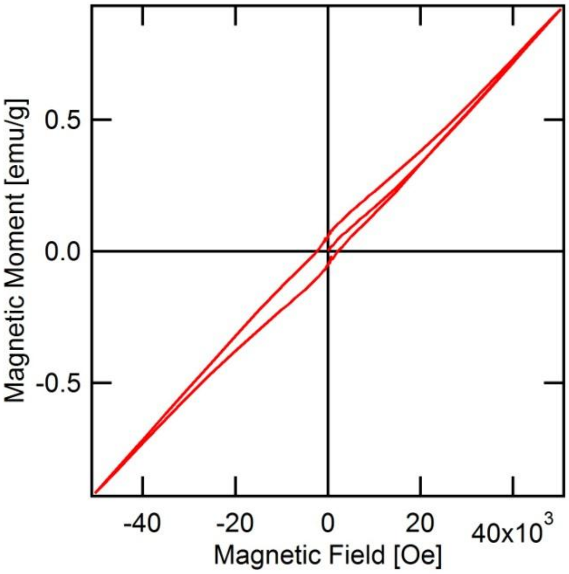

Figure 6.25. Hysteresis curve of hematite nanoparticles at 5 K.

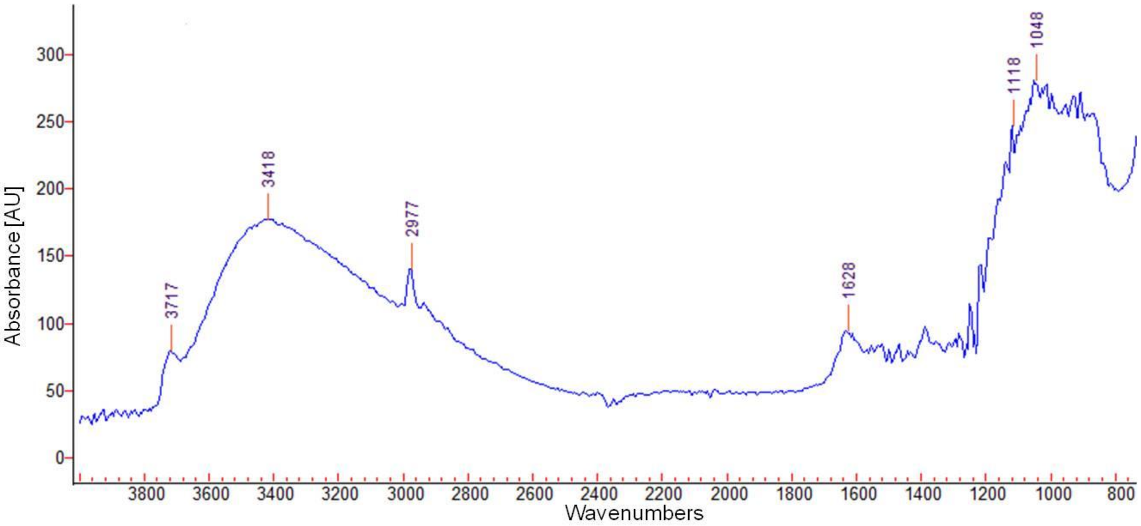

Figure 6.26. PAS-IR Absorbance spectrum for hematite nanoparticles.

Lastly, EDS was performed on the hematite nanoparticles. The spectrum shown in Figure 6.27 indicates that no non-crystalline impurities were found in the sample that would not have appeared in the XRD pattern.

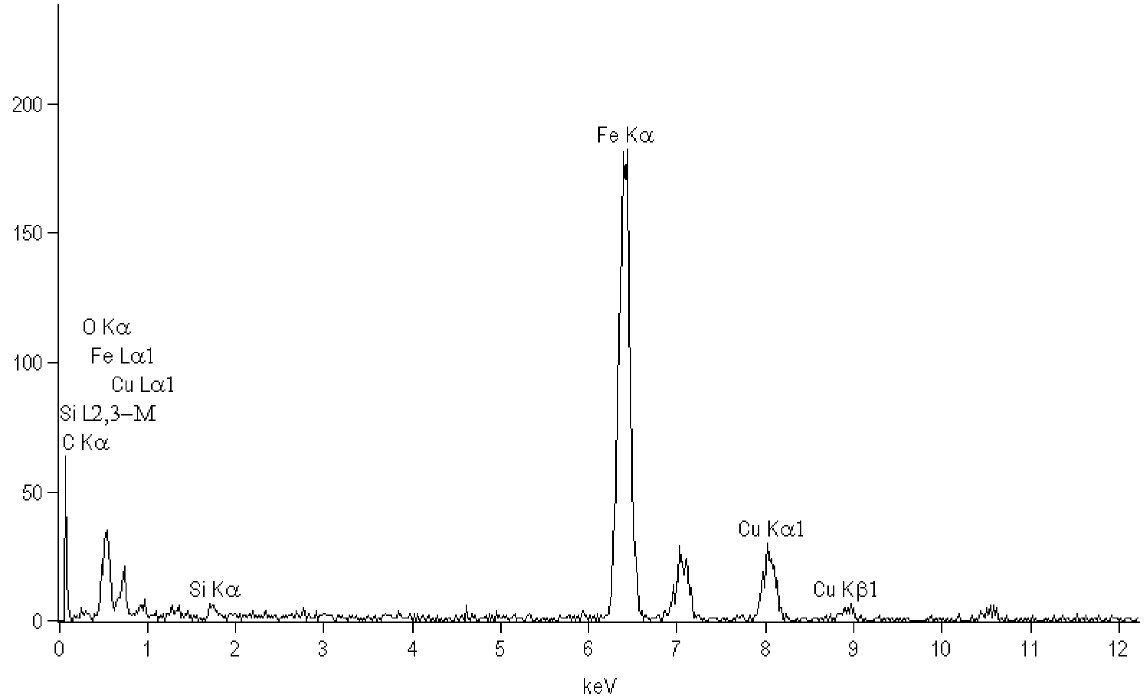

Figure 6.27. EDS spectrum for hematite nanoparticles.

6.5 Conclusion

We have successfully synthesized four different phases of iron oxide and oxy-hydroxide nanoparticles. These phases have been characterized thoroughly by a variety of techniques establishing the size, shape, composition, purity and magnetic properties of each sample. In the next chapter, we will explore the adsorbent capacity of each of these materials for the removal of arsenite (As^{3+}) from neutral aqueous solutions. By having well characterized samples, we hope to determine the best phase for As removal.

CHAPTER 7

REMOVAL OF ARSENITE CONTAIMANT USING IRON OXIDES AND OXY-HYRDOXIDES NANOPARTICLES

7.1 Abstract

There is an increasing interest in the removal of arsenic from water through the utilization of iron's affinity for arsenic oxo-anions. Nano-size iron oxides including goethite, maghemite, magnetite and hematite have been synthesized and characterized systematically. These nanoparticles were exposed to arsenic solutions to measure the percent uptake of arsenic by each phase of iron oxides. Arsenic concentrations in the collected supernatant were measured using ICP-AES. The minimum detection limit for ICP-AES of arsenic was 113 ppb. Arsenic bound nanoparticles were characterized by PAS-IR, XPS, and EDS. All show that the arsenic oxo-acid is chemically bound to the surface. Adsorption isotherms were plotted for various sized maghemite nanoparticles to obtain Freundlich parameters. The adsorption constant (K) averages over a 400% increases in comparison to the literature[98d]; the parameter (n) is above1indicating favorable adsorption.

Our research, along with most of the literature, indicates that the hematite phase has the highest arsenic removal affinity of the iron oxide adsorbent class. In trying to harness this adsorption potential merged with the magnetic control seen in spinel ferrites, we have synthesized core-shell Iron Oxides@Cobalt Ferrites. This was done via the aminolytic method using a previously synthesized $CoFe_2O_4$ core which was reacted with iron oxide. Both samples, hematite and maghemite core-shell particles, were exposed to

various concentration of arsenite and maghemite core-shell particles were found to have the higher removal affinity. The higher affinity results from the difference in size between the core-shell nanoparticles with the maghemite derivative being 8 nm and the hematite derivative, 20 nm.

7.2 Introduction

Exposure to arsenic in drinking water results in increased occurrence of skin, kidney, lung, and bladder cancer. Chronic arsenic ingestion can cause skin hyper pigmentation and keratoses (scaly patches of skin that appear on the hands and feet). Both conditions are documented precursors to skin cancer[104]. The estimated annual cost arsenic removal in the United States alone is 181 million dollars or approximately 32 dollars per household[105]. This is well within the means of most Americans but out of range for residents of many developing countries.

Arsenic contamination of a drinking water source can result from natural or human activities. Arsenic, naturally occurring, is introduced into the water supply via these geogenic occurrences: volcanic activity, the erosion of rocks and minerals, and forest fires. Arsenic is used for the production of drugs, dyes, metals, paints, semi-conductors, soaps, and wood preservative. Other anthropogenic sources are pesticides, mining, and smelting [104].

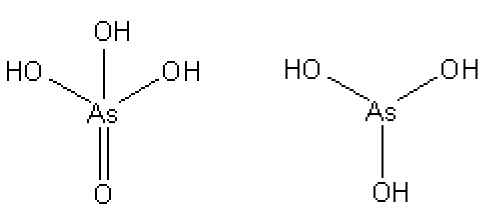

Figure 7.1. Structure of Arsenic Compounds

Arsenic in the environment can take many forms and a variety of adsorption mechanisms have been used to describe arsenic interactions with iron oxides. Speciation information for arsenic is crucial for understanding As-Fe binding. There are two inorganic forms of arsenic, arsenate As(V) and arsenite As(III) shown in Figure 7.1. Arsenate ($H_2AsO_4^-$) is predominantly anionic around neutral pH as arsenic acid, while arsenous acid, arsenite (H_3AsO_3), is uncharged, Figure 7.2 [106].

$$\begin{array}{lcll}
H_3AsO_4 & \longleftrightarrow & H^+ + H_2AsO_4^- & pKa = 2.20 \\
H_2AsO_4^- & \longleftrightarrow & H^+ + HAsO_4^{2-} & pKa = 6.97 \\
HAsO_4^{2-} & \longleftrightarrow & H^+ + AsO_4^{3-} & pKa = 11.53 \\
\multicolumn{4}{c}{\text{Arsenic Acid As (V)}} \\
\hline
H_3AsO_3 & \longleftrightarrow & H^+ + H_2AsO_3^- & pKa = 9.2 \\
H_2AsO_3^- & \longleftrightarrow & H^+ + HAsO_3^{2-} & pKa = 12.1 \\
HAsO_3^{2-} & \longleftrightarrow & H^+ + AsO_3^{3-} & pKa = 12.7 \\
\multicolumn{4}{c}{\text{Arsenous Acid As(III)}}
\end{array}$$

Figure 7.2 Acid-Base Equilibrium of Arsenic Acid

The speciation of arsenic in aqueous environments directly affects its toxicity in the body. Arsenite is usually more toxic as it is very water-soluble and much more mobile through biological membranes than arsenate. Both forms however are toxic and interfere with important biological systems such as energy production and protein folding. Arsenite has a more wide spread effect because it binds to the thiol groups of many proteins thus interferes with their function. Arsenate, which is similar in structure to phosphate, causes inhibition of oxidative phosphorylation[107]. This is why the EPA and WHO have lowered the maximum level of arsenic to 10 ppb.

The best available technologies (BAT) currently endorsed by the EPA for arsenic removal include anion exchange, activated alumina (AA), reverse osmosis (RO), modified coagulation/filtration, and modified lime softening. Concerns with these techniques include use of chemicals to treat water and their effect on water quality, large volumes of waste sludge generated with high arsenic concentration, need for secondary treatment, interference of other ions with the efficiency of removal, and high installation and maintenance cost [107].

The first BAT method uses anion exchange resins to electro- statically hold arsenic to its surface. This method can be used to treat water with arsenic concentration up to 2 μg/L but is one of the most expensive methods. Next, activated alumina utilizes an absorption mechanism where arsenic species are attached to a surface by chemical and physical properties. Though this method is well established and inexpensive, it is not acceptable for large scale use due to the need for constant and careful monitoring. In reverse osmosis, membranes are used to separate arsenic from water either by size or charge exclusion. With this method, the highest water quality is achieved. However, it requires expensive installation; frequent monitoring; and pH, temperature, and pressure control of the water system. All these factors make this method one of the most costly. In modified coagulation and filtration, a chemical process is used to turn the arsenic into an insoluble solid and is then filtered. As with reverse osmosis, this method requires control of water conditions such as pH and pressure. However, for coagulation the chemicals used are commonly available and relatively inexpensive. Lastly, with modified lime softening, lime is used for the precipitation of arsenic. This is a proven and reliable method but requires secondary treatment and produces highly toxic arsenic sludge [107,108,109].

One modification of the current BATs to improve arsenic removal is the incorporation of iron oxides. Iron oxides have unique arsenic adsorption properties and are inexpensive to produce. Some of the current research being done in this area include using iron oxide coated cement[110], bead cellulose loaded with iron oxy-hydroxide[111], natural iron ores[112], and zero-valent iron/filter sand[113]. This research does not consider the surface bonding mechanism between the arsenic and the iron.

There are many forms of iron oxides most of which are used in arsenic removal techniques. The iron oxide is formed in-situ by adding a non-oxide iron source to water. The exact nature of the arsenic binding and the effect of impurities on binding efficiency are not well understood[96]. Synthesizing well characterized iron oxides will afford better comprehension of the arsenic surface binding. Better understanding of the binding affinity for arsenic is necessary for the incorporation of iron oxides into the BATs. Knowing the best iron oxides or oxy-hydroxides for arsenic removal will allow for the exploitation of iron oxides most useful properties: magnetism. This can be accomplished either by the material's individual properties or by combining magnetic support with the nonmagnetic adsorption material. By utilizing the magnetic nature of the materials as well as the iron oxides affinity for arsenic, great improvements can be made to the currently preferred BATs.

The arsenic binding affinity and arsenic removal efficiency for different phases of iron oxides and oxy-hydroxides has been explored. We synthesized a range of nanosized iron oxide and oxy-hydroxide particles from published procedures[87, 101] and thoroughly characterized each batch by XRD, SQUID, XPS, TEM, EDS, and PAS-IR. All the maghemite samples contained hematite impurities and were magnetic. All the materials were exposed to stock arsenate solutions of varying concentrations. Arsenic uptake on particles was measured by HR-TEM EDS. Arsenic left in the supernatant after exposure was measured by ICP-AES which has a lower detection limit of 113 ppb. We were also able to show that the synthesized particles were reusable after light base stripping. This exciting discovery coupled with the magnetic properties allows for this iron oxide mixture to be a reusable, easily recyclable arsenic remover. Finally, we combined a non-magnetic removal phase, hematite, onto a magnetic support, $CoFe_2O_4$, in a core-shell system to pursue the best removal efficiency with magnetic control of adsorbent.

7.3 Experimental

7.3.1 Arsenic stock solutions

Aqueous stock solutions (2 mM) were be made with an As(III) source, sodium (meta)arsenite, dissolved in HPLC grade water. All samples were exposed to the same batch of As solution. The lower As concentration solutions (1 mM, 0.1 mM, and 0.01 mM) were all dilutions of this initial solution with HPLC grade water. The exact concentration for each solution was determined by ICP-AES.

7.3.2 Different phase removal affinity comparison

For each sample, ~50 mg of nanoparticles were exposed to the arsenite (25 mL, 2 mM) solution and agitated for 8 hrs. The samples were separated via a magnetic field or allowed to settle to isolate the particles from the supernatant, which was collected for analysis. The solid was washed three times with HPLC grade water then allowed to dry in air. This collection procedure was performed for all contaminant exposed particles. Surface studies were performed on the particles using photo-acoustic infrared spectroscopy (PAS-IR), Energy Dispersive X-ray Spectroscopy (EDS), and X-ray Photoelectron Spectroscopy (XPS). Collected supernatant was analyzed for As and Fe content by ICP-AES without any modifications.

PAS-IR was taken on the exposed powder samples without any purification or preparation. Samples were purged with the carrier gas, He, in the instrument. For EDS, dried powder sample were redispersed in HPLC grade water and deposited on carbon coated TEM grid. XPS was also taken on the exposed powder sample. For sample preparation, the powders were placed in a vacuum oven overnight to remove any excess moisture or atmosphere gas.

7.3.3 Arsenic Removal by Maghemite Nanoparticles to Detection Limit

Increasing amounts of maghemite nanoparticles (10 mg, 20 mg, 30 mg, 40 mg, 60 mg, 80 mg, and 100 mg) were exposed to the arsenite solution (25 mL, 1 mM) for 8 hrs to create a decay curve. Samples were collected by the same procedure from the above section. Supernatant was again analyzed by ICP-AES.

7.3.4 Size Influence of Maghemite Nanoparticles on Arsenic Adsorption

Each sample, ~25 mg of different sized maghemite nanoparticles (5 nm, 7 nm, 8 nm 10 nm, 12 nm, and 14 nm) were exposed to 25 mL of four different arsenite concentrations (2 mM, 1 mM, 0.1 mM and 0.01 mM) for 8 hrs. Collection of the particles was performed. ICP-AES was used to analyze the supernatant.

7.3.5 Surface Regeneration Study with Maghemite Nanoparticles

For each sample, ~20 mg of 2 mM arsenite exposed nanoparticles were stripped using various concentration of 25 mL NaOH solution (0.5 M, 1 M, 2.5 M, and 5 M) for 8 hrs. Particles were collected via a magnetic field and washed three times with HPLC grade water. Stripped particles were then re-exposed to 25 mL of arsenite solution (1 mM) for 8 hrs. Collection procedure was followed and supernatant analyzed by ICP-AES.

Next, two sizes of maghemite were exposed to As and regenerated several times. Maghemite nanoparticles (~50 mg) were weighed out in 30 mL beakers. The whole system was weighed then 15mL of arsenite (1 mM) was added. The particle-arsenic mixture was agitated overnight then the particles and supernatant were collected. After being washed with HPLC grade water, the exposed particles were regenerated with 1M NaOH solution for 2 hrs. Particles were collected and washed again and allowed to dry for 10 hrs. The dried system was re-weighed. The above procedure was repeated five times. All supernatants were submitted for analysis by ICP-AES as obtained.

7.3.6 Core-Shell Maghemite@$CoFe_2O_4$ and Hematite@$CoFe_2O_4$ Nanoparticles Synthesis

Core-shell nanoparticles were synthesized using the aminolytic method. Previously produced cobalt ferrite nanoparticles (~6 nm) were used as cores. Cores (~500 mg) were added to the reaction with ~0.3 g of iron(III)acetate. Dibenyzl ether (15 mL) as a solvent and oleylamine (5 mL) as a solvent, reagent, and surfactant were used.

The mixture was heated to 140˚C and held for an hour under Ar. The temperature was raised to 260˚C and maintained for an hour. The reaction was returned to room temperature and the particles were separated by the application of a magnetic field. The collected solid was washed with absolute ethanol several times. An XRD pattern was taken to confirm shell formation. Dried sample was heated to 600˚C in air to convert the maghemite shell to hematite. An XRD pattern was taken to confirm conversion. The heated sample was redispered in ethanol and magnetically separated using a peristaltic pump and a strong magnet.

7.3.7 Core-Shell Removal Affinity

Core-shell nanoparticles (~25 mg) with both hematite and maghemite shells were exposed to 25 mL of arsenite solution (1 mM) for 8 hrs. Particles were collected by the established procedure and the supernatant analyzed by ICP-AES.

7.4 Results and Discussion

7.4.1 Different phase removal affinity comparison

Different phases of iron oxides and oxy-hydroxides were all exposed to arsenite solution to determine which had the highest arsenite affinity. Figure 7.3. is a plot of the results. Hematite and maghemite had the highest arsenic uptake while magnetite had the lowest. All the maghemite nanoparticles synthesized had hematite impurities which may play a role in the arsenic removal ability of this material. Based on this information, studies were focused mainly on maghemite nanoparticles.

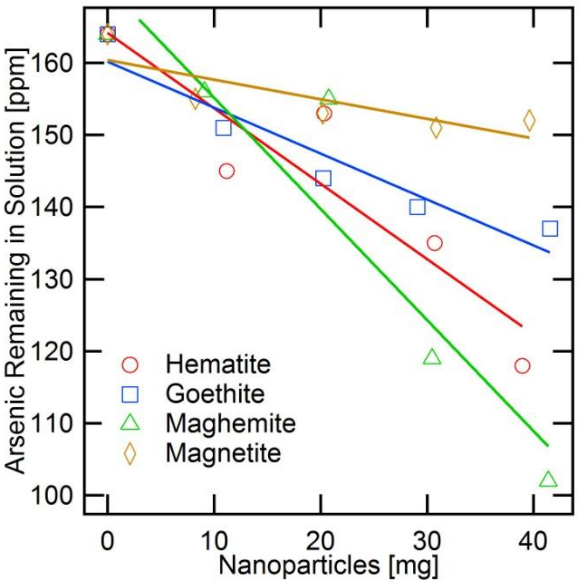

Figure 7.3. Arsenic uptake by different phases of iron oxides and oxy-hydroxides.

EDS and PAS-IR were performed on all iron oxide and oxy-hydroxide samples. Since the collected, exposed particles were washed with HPLC grade water several times before these characterization techniques were performed, the presence of As confirms that contaminant is bound to the surface and not just removed via magnetic shearing or precipitation. In Figures 7.4-7 are EDS spectra from all the exposed samples. The ratio of Fe to As are as follows: goethite 127:1, hematite 33:1, maghemite 217:1, and magnetite 199:1. Though these ratios are very small, they are not unexpected as EDS was performed on a single nanoparticle for each sample.

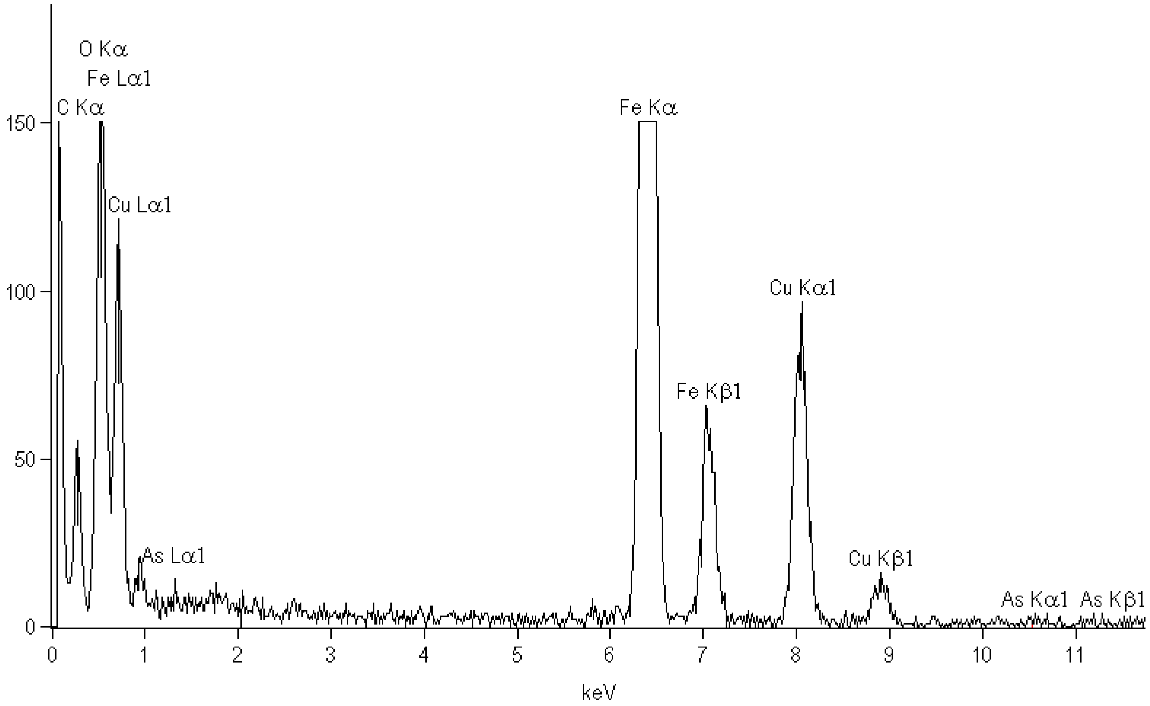

Figure 7.4. EDS spectrum of goethite nanoparticles exposed to As.

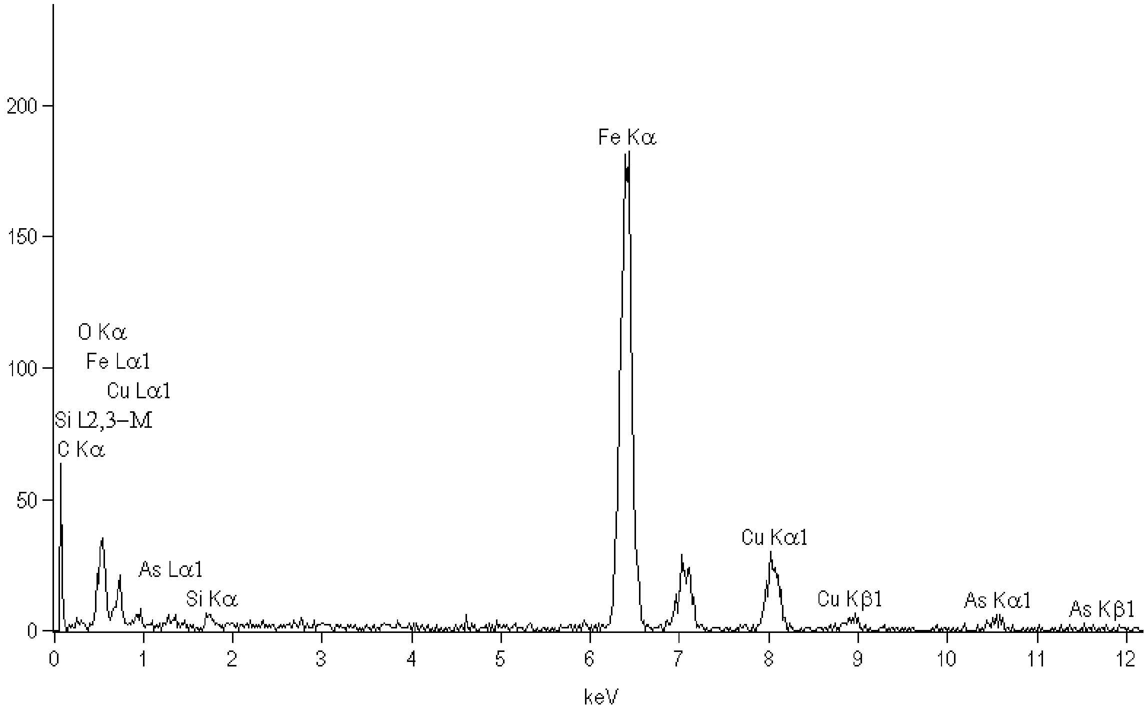

Figure 7.5. EDS spectrum of hematite nanoparticles exposed to As.

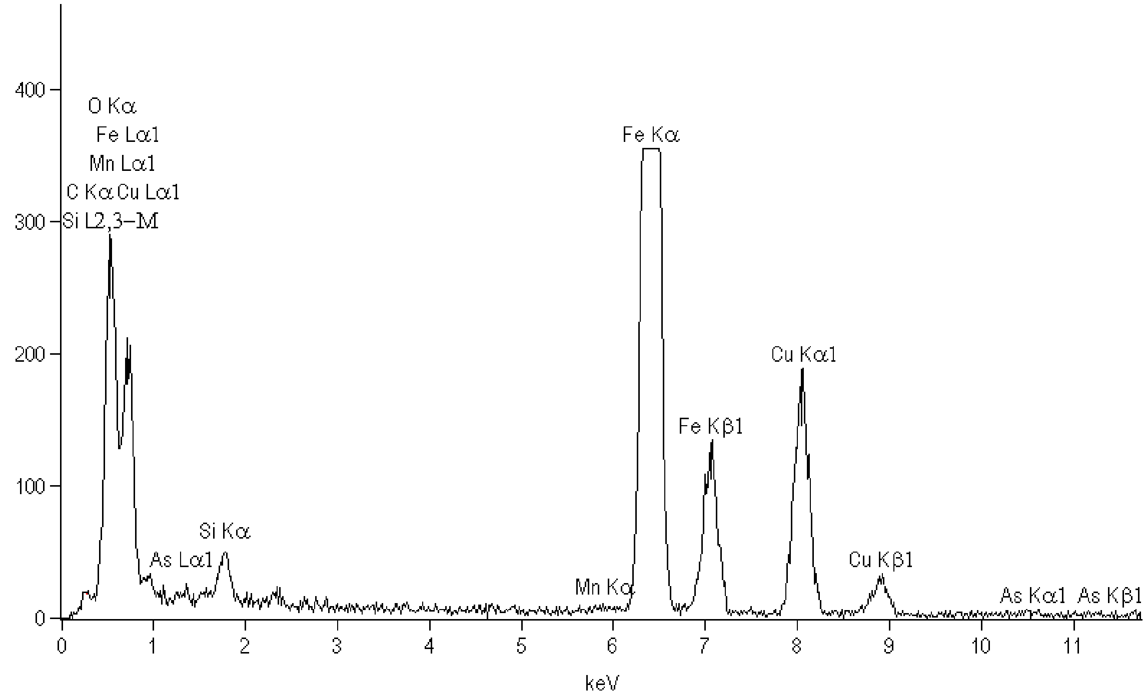

Figure 7.6. EDS spectrum of maghemite nanoparticles exposed to As.

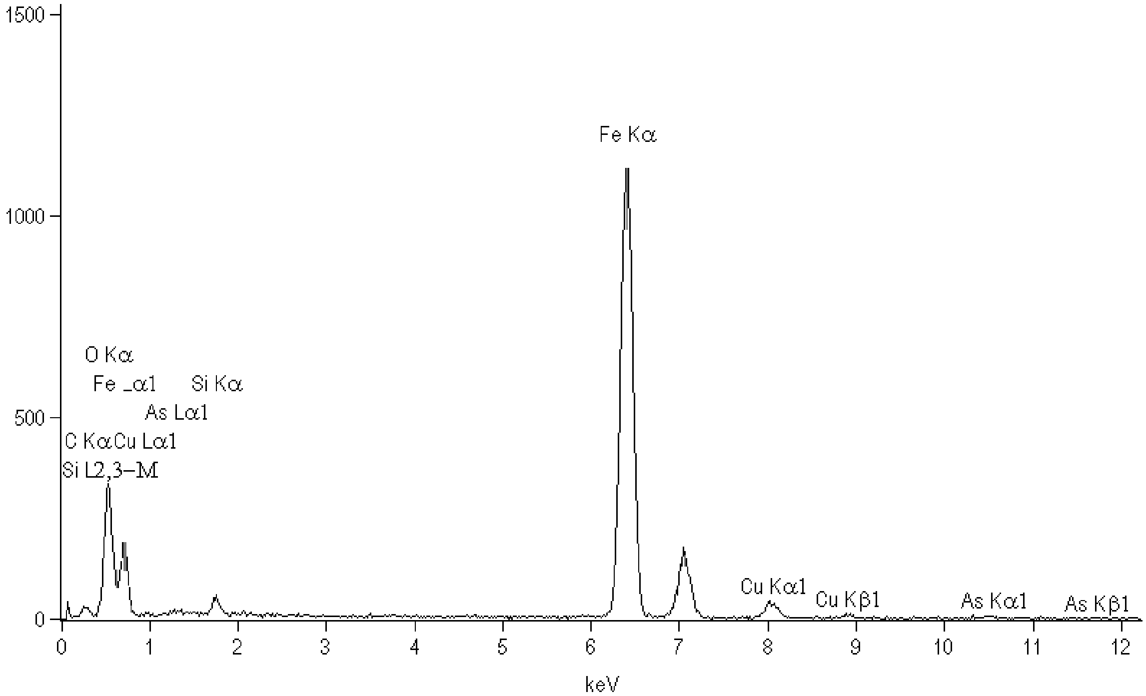

Figure 7.7. EDS spectrum of magnetite nanoparticles exposed to As.

PAS-IR was performed before and after exposure to try and determine binding polyhedron structure from stretching frequencies. Changes in the PAS-IR are seen but we have not been able to correlate these stretching modes to the exact binding motif for the oxy-acids polyhedra. Shown below in Figure 7.8-11 are the PAS-IR performed on the samples.

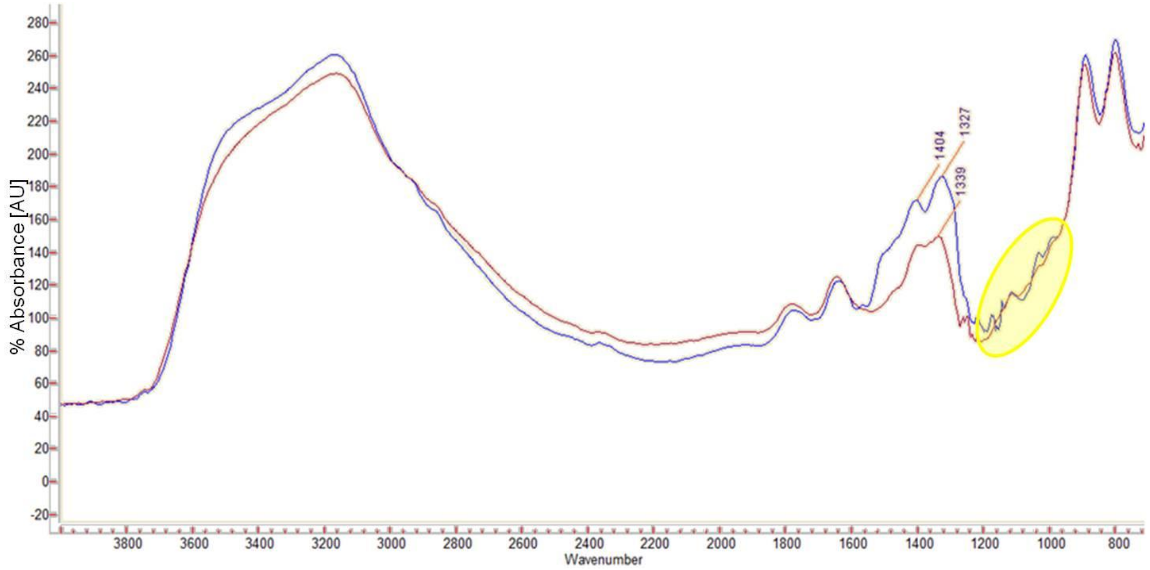

Figure 7.8. PAS-IR of goethite nanoparticle pure and as exposed overlaid. Highlighted area is As polyhedron stretching region.

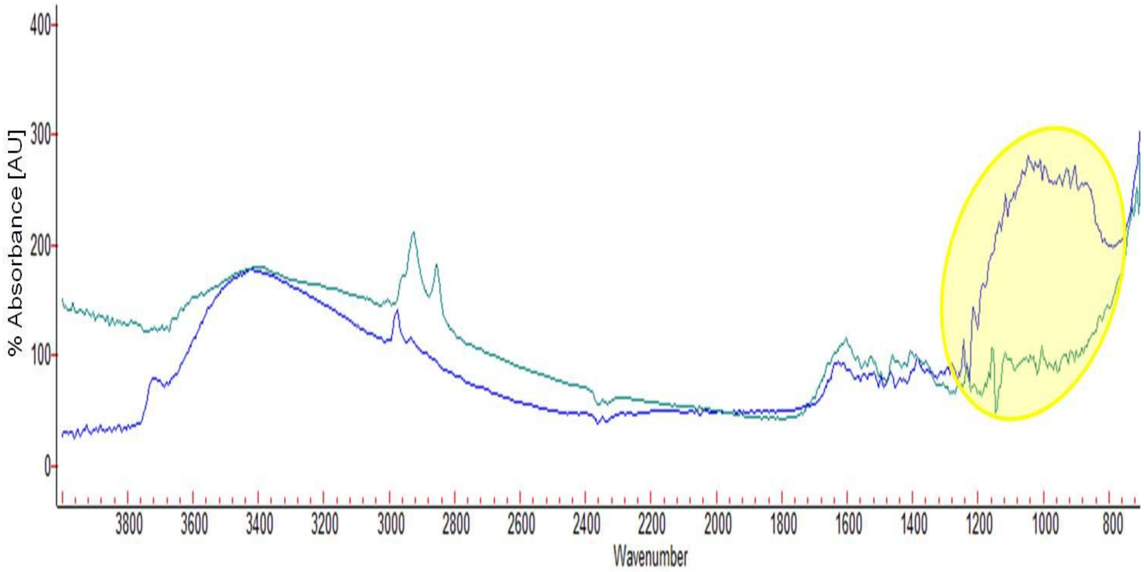

Figure 7.9 PAS-IR of hematite nanoparticle pure and as exposed overlaid. Highlighted area is As polyhedron stretching region.

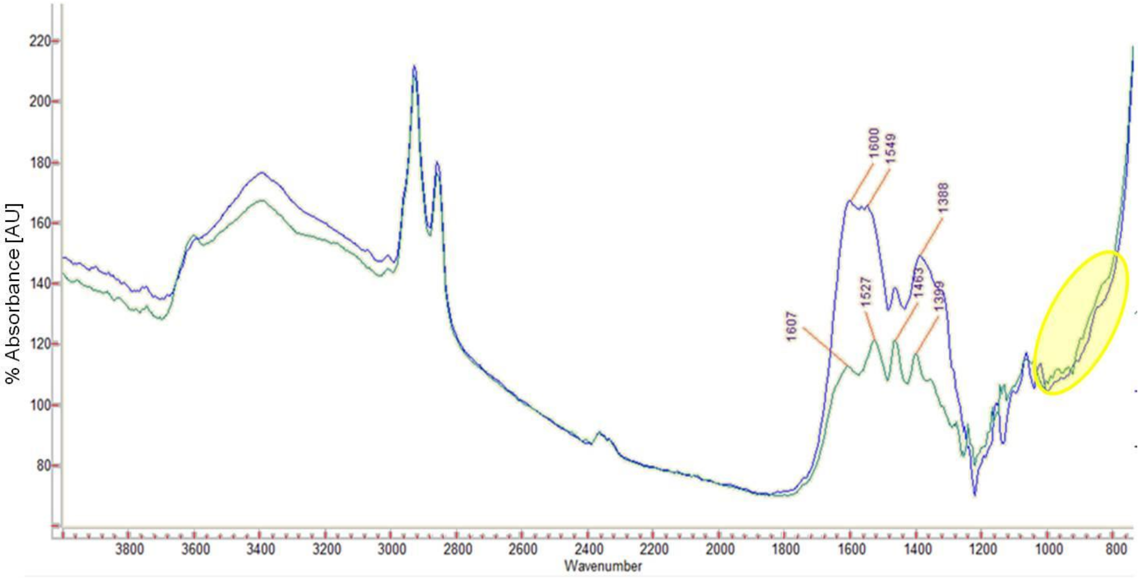

Figure 7.10. PAS-IR of maghemite nanoparticle pure and as exposed overlaid. Highlighted area is As polyhedron stretching region.

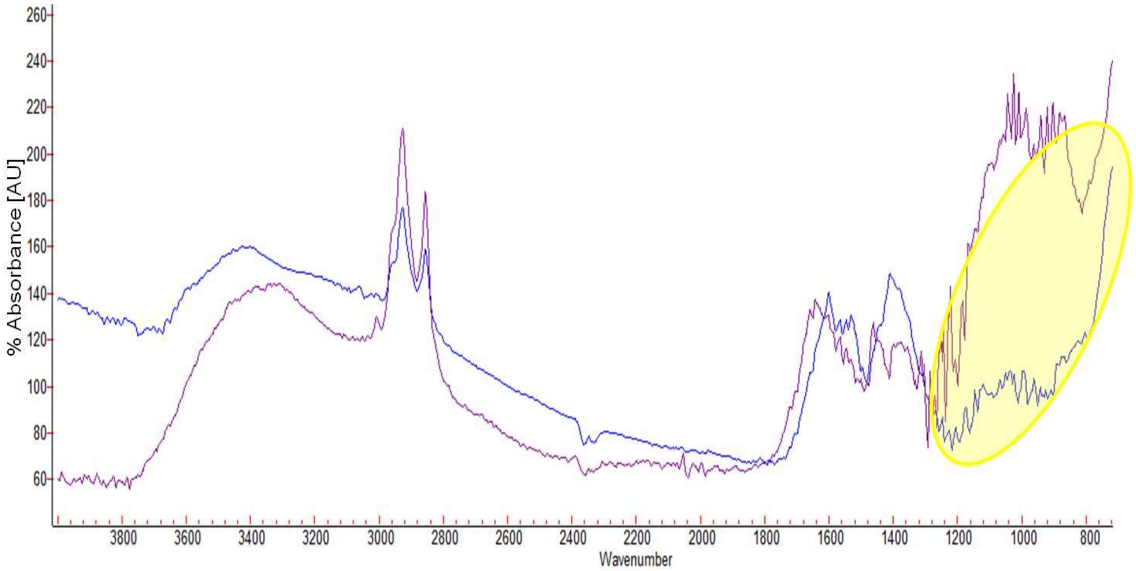

Figure 7.11. PAS-IR of magnetite nanoparticle pure and as exposed overlaid. Highlighted area is As polyhedron stretching region.

Some of the literature has suggested that the arsenic or iron atoms on the surface will undergo a redox process during adsorption[114]. XPS was done on all the samples to determine if there were any changes in oxidation state for either the adsorbent or contaminant. As seen in Figures 7.12-15 there is no change in chemical state after exposure.

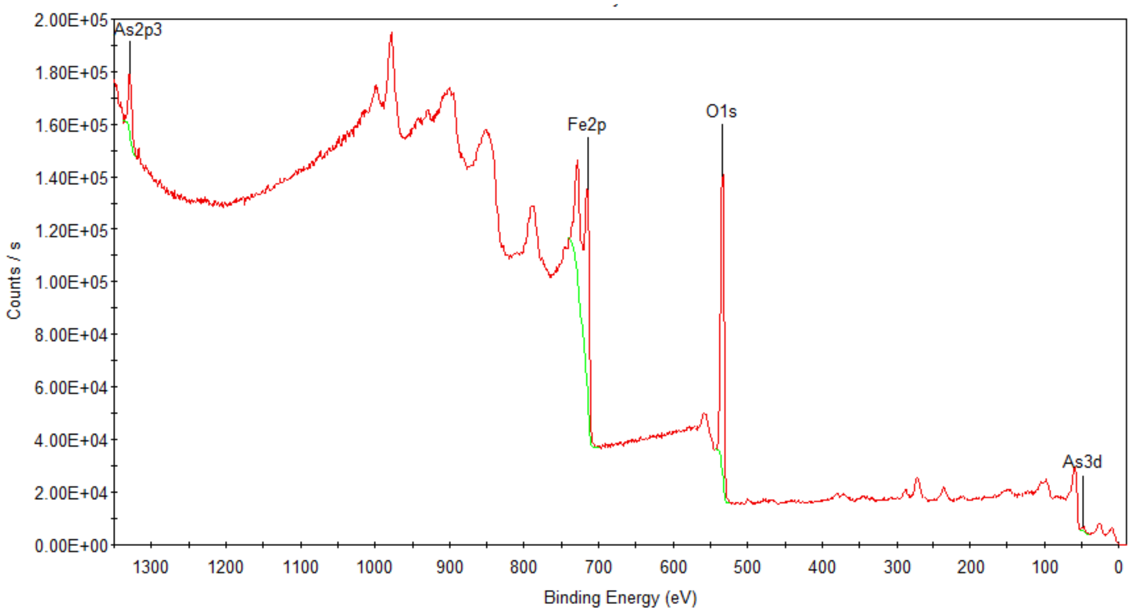

Figure7.12. XPS survey scan of as exposed goethite particles.

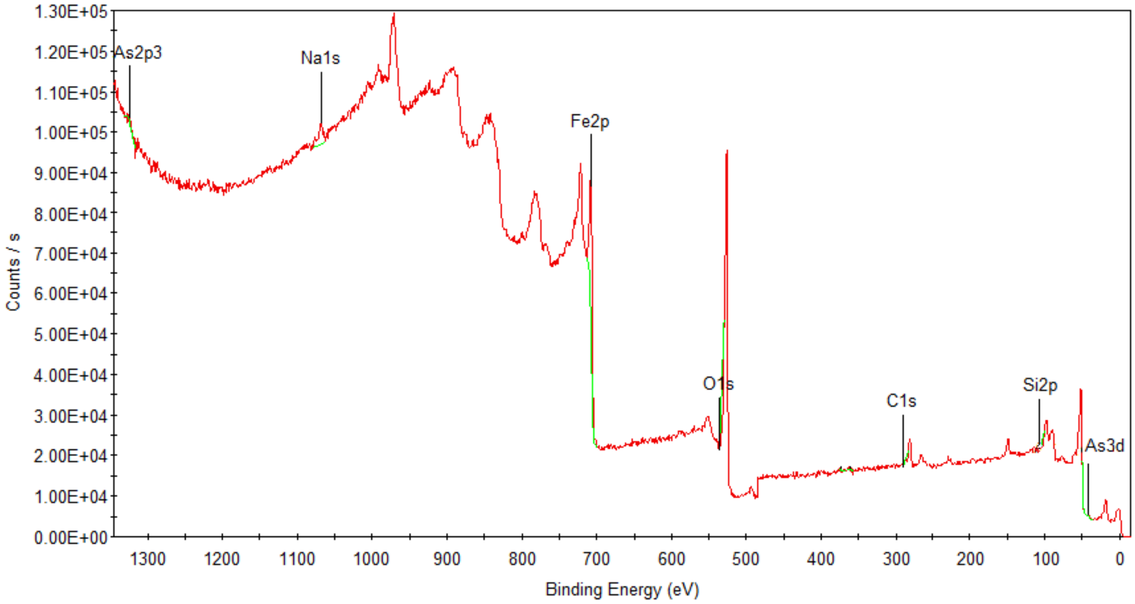

Figure7.13. XPS survey scan of as exposed hematite particles.

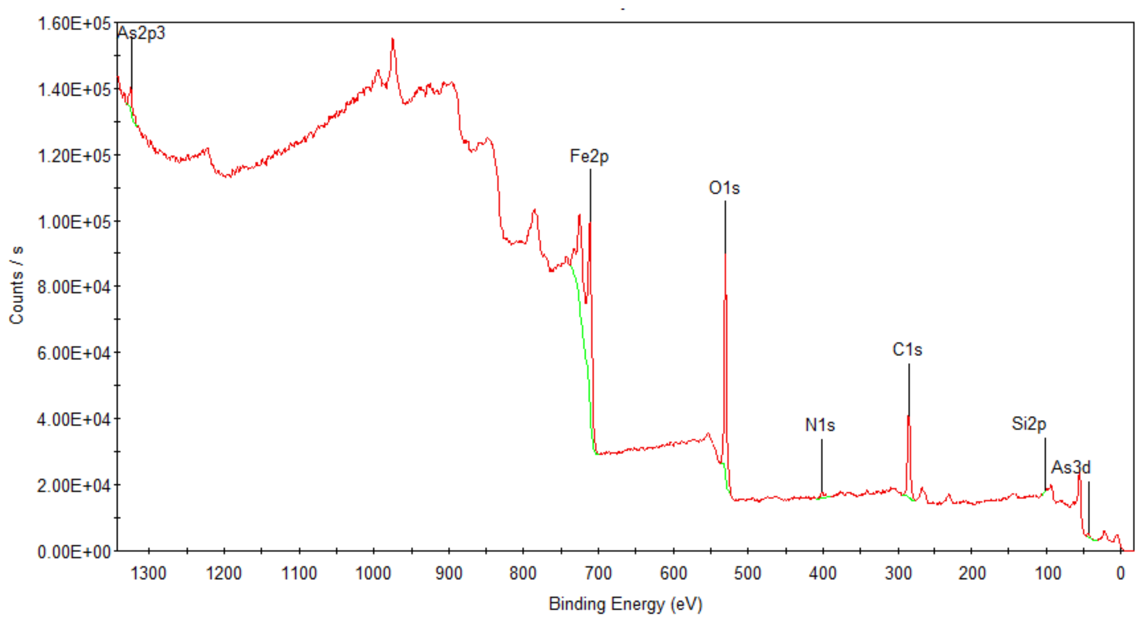

Figure7.14. XPS survey scan of as exposed maghemite particles.

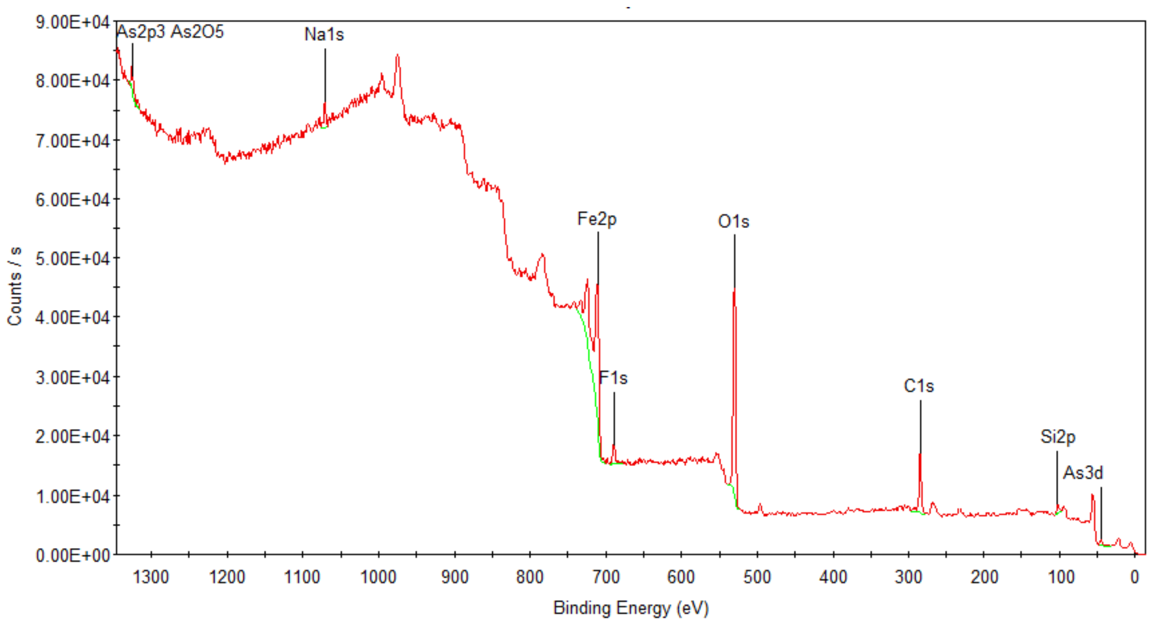

Figure7.15. XPS survey scan of as exposed magnetite particles.

7.4.2 Arsenic Removal by Maghemite to Detection Limit

Since maghemite nanoparticles have one of the higher removal affinities and magnetic properties that allow for facile separation for the water system, a more thorough decay curve was produced. Increasing amounts of maghemite nanoparticles were exposed to arsenite solutions in an effort to determine the amount of nanoparticles needed to reach the detection limit of ICP-AES (113 ppb As).

Figure 7.16 shows the arsenic concentration in the supernatant after eight hours of exposure to different amounts of nanoparticles. The first point is the concentration of the arsenite solutions as no particles were added. The plot shows that the arsenic concentration decreases with an increase in nanoparticle amount and the largest amount of nanoparticle removed more than 90% of the arsenic in solution.

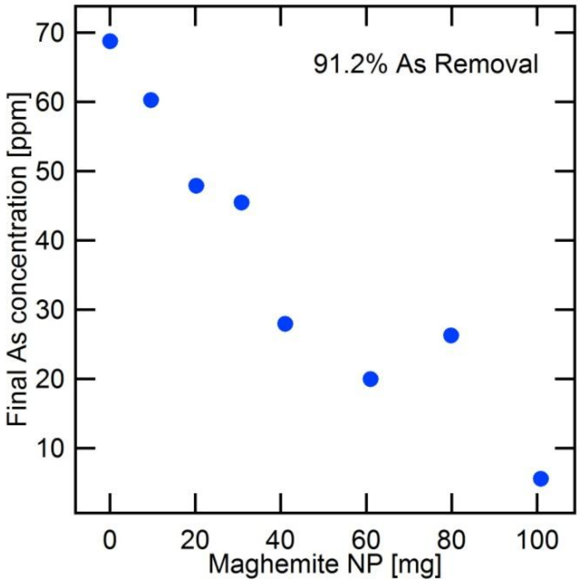

Figure 7.16 Arsenic Removal as a Function of Nanoparticle Amount

7.4.3 Size Influence of Maghemite Nanoparticles on Arsenic Adsorption

Since adsorbance is the binding of contaminants to the surface of a material, size studies are extremely important. With nanoparticles even a small decrease in size can produce an appreciable increase in surface area when the same amount of sample is used.

To determine this influence on arsenic uptake, various sized nanoparticles were exposed to four different concentrations of arsenite solution. In Figures 7.17 and 7.18, the effect of size on uptake is plotted. As expected, the smallest size has the highest uptake per gram of adsorbent. The trend is linear in the utilized concentration ranges. Eventually, saturation would be expected, but it is not reasonable to use higher concentrations of contaminant as those levels will not be reached in public water systems[115]. The points closest to the origin are all the same value because each sized nanoparticles reduced the lowest arsenic concentration to below the detection limits of ICP.

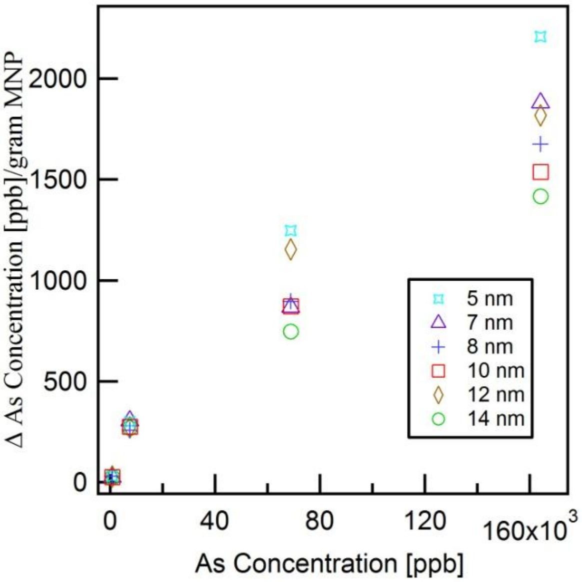

Figure 7.17. Arsenic uptake with respect to the initial arsenic concentration for various sized maghemite nanoparticles.

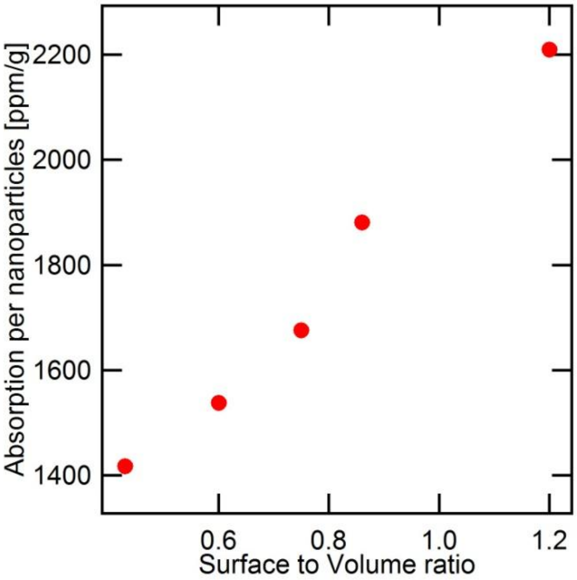

Figure 7.18. Arsenic uptake with respect to surface to volume ratio for maghemite nanoparticles.

Using the last three data sets, adsorption coefficients can be determined and will allow for the comparison between these nanoparticle adsorbents and literature values[98d] for other absorbents. The Freundlich isotherm[116] is given by the following equation:

$$q_e = K * C_e^{1/n} \tag{7.4.3.1}$$

where q_e is the mass of the contaminant adsorbed per mass of adsorbent, C_e is the contaminant concentration after adsorption, and K and n are constants relating to adsorption capacity and energy of adsorption, respectively. When written in logarithmic form, as seen below, K and n can be determined from the intercept and slope.

$$\log q_e = \log K + (1/n * \log C_e) \tag{7.4.3.2}$$

Figure 7.19 shows the plots of four of the maghemite sample sizes with the best linear correlation. As seen, the systems have a strong linear relationship and are well described by the Freundlich isotherms.

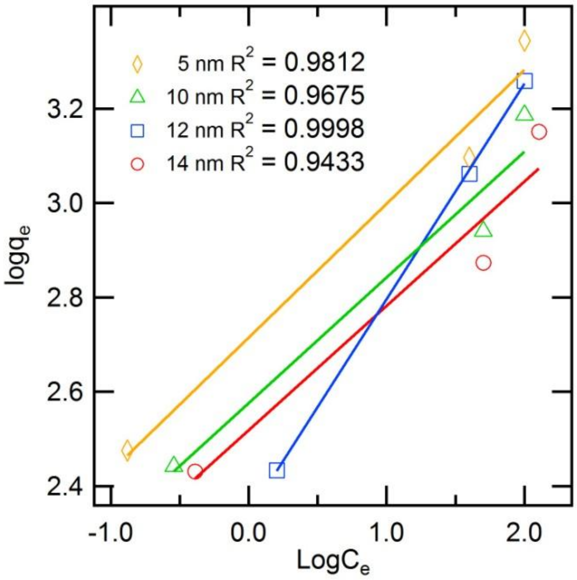

Figure 7.19. Arsenite adsorption on maghemite nanoparticles fitted by Freundlich isotherms.

In Table 7.4, literature values[98d] for several adsorbent materials have been provided. The maghemite system is a vast improvement over the current models. The values provided for the maghemite system are an average of the values for all samples sizes. For the smallest size (5 nm), there is over a 700% improvement on previously published values with an adsorption coefficient (K) of 518.56 mg/g.

Table 7.4.. Freundlich parameters for arsenic adsorbents

Adsorbents	**Freundlich Parameters** **K (mg/g)**	 **n**
Maghemite with hematite impurities NPs	361.19	3.34
Magnetite-maghemite NPs	9.4	2.1
Activated Carbon	5.09	1.76
Magnetite	10	2.5
Maghemite	3.4	6
Activated Alumina	0.2249	2.22
Akaganeite	69.7	2.5

7.4.4 Surface Regeneration Study with Maghemite Nanoparticles

During the investigation into the best arsenic removal phases, it was determined that the surface of the particle could be regenerated with base solution and that the particles would regain the arsenic uptake ability. Since some of the iron oxides phases have magnetic properties that allow for the manipulation and direction of the adsorbent, it is simple to reclaim the particles after exposure. To fully exploit these magnetic properties, a surface regeneration study was performed to determine optimal base concentration for surface stripping and the number of regenerations that could be obtain from one sample of adsorbents.

Figure 7.20 shows the arsenic uptake by nanoparticles stripped with the corresponding base solution. As is seen, there is very little variety between 0.5 M-7.5 M NaOH solutions. The highest concentration (10 M) produces the particles with the highest arsenic uptake however working with the very basic solution can be hazardous. The first data point is freshly synthesized particle which have the best removal affinity. The loss of arsenic removal after first use and regeneration is ~ 50%. By taking this uptake loss into consideration, the correct amount of particles can be added to the contaminated solution to reduce contaminant levels to the desired point. Based on these results, regeneration trials were done with a 1 M base stripping solution.

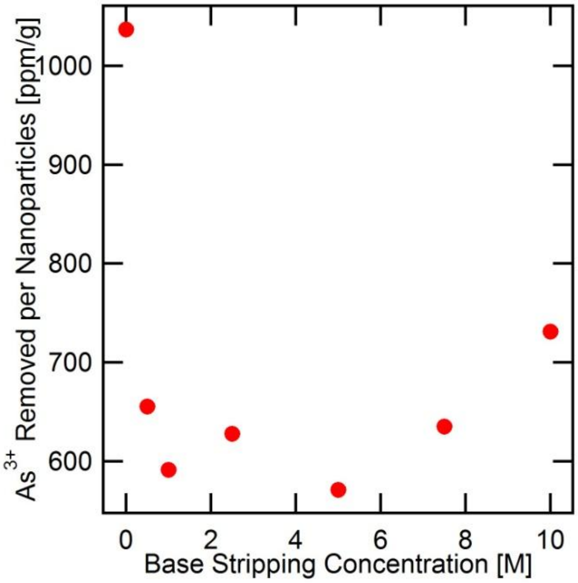

Figure 7.20. Arsenic uptake by particles regenerated with different concentration base solutions.

For the next part of the study, nanoparticles in beakers were weighed and exposed to arsenic solutions. After each exposure, the particle surface was regenerated by stripping solution and then re-exposed. Careful weight measurements were kept to account for any loss of adsorbents during washing and stripping. This stripping and re-exposure was repeated for five trials (Figure 7.21). Again, the smaller sized particles have the higher uptake but, since the smallest are similar in size, there is not much variation. After five regenerations of the surface, the arsenic uptake drops significantly. This could be improved by stripping with a higher concentration of base or for a longer period of time. Overall, this study is very encouraging for the use of these magnetic nanomaterials in water remediation.

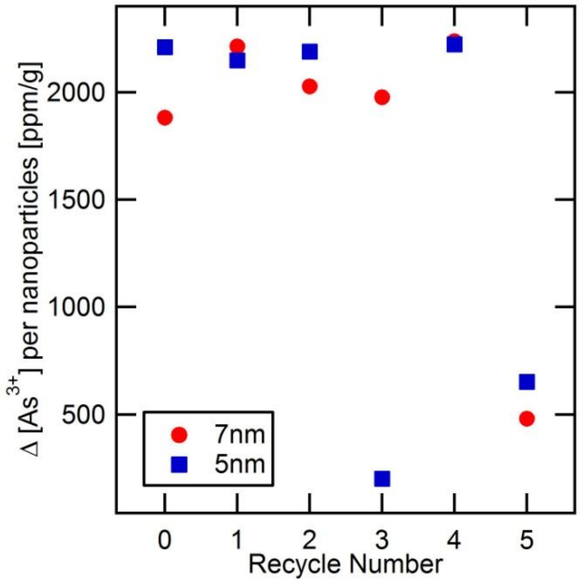

Figure 7.21. Arsenic uptake with respect to recycle number for maghemite adsorbent.

7.4.5 Core-Shell Removal Affinity

Since the hematite phase had the best removal affinity, core-shell nanoparticles were synthesized to combine the best removal phase with the desired magnetic properties. Core-shell nanoparticles with both hematite and maghemite shell were produced using the aminolytic method. An XRD pattern was taken before heat treatment and only spinel ferrite peaks can be identified (Figure 7.22). From previous research, the conversion temperature from maghemite (spinel ferrite structure) to hematite (corundum structure) is 550˚C so the core-shell sample was heated to 600˚C to ensure complete conversion. During the synthesis process, iron acetate could have produced new particles instead of forming a shell. To remove all pure iron oxide particles, magnetic separation was performed using a forced flow system and a magnetic field. Only the particles that were attracted to the magnetic field were collected. These particles were analyzed by XRD and show the expected hematite peaks (Figure 7.22).

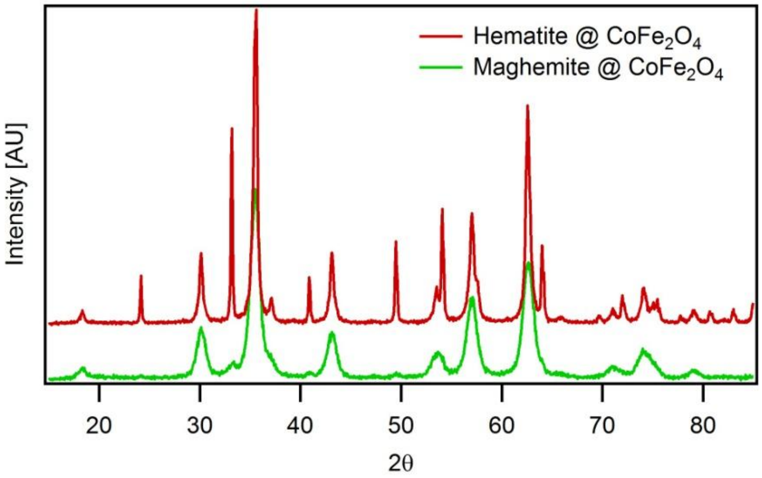

Figure 7.22. XRD pattern for core-shell nanoparticles.

These core-shell particles, both maghemite and hematite, were exposed to arsenite solution. Figure 7.23 shows the plot of adsorption per gram of nanoparticle as it correlates to the initial concentration of arsenic in solution. As expected, as the concentration increases so does the uptake per adsorbent. However, maghemite core-shell particles have a higher removal affinity than the hematite derivative. This was unpredicted due to the higher removal affinity of hematite seen earlier (7.4.1). To account for this discrepancy, size was collected for the two core-shell samples. The hematite sample was ~20 nm while the maghemite sample was only ~12 nm. As shown in a previous section (7.4.3), size of the adsorbent does directly influence the uptake of contaminants due to the change in ratio between surface area and volume. Future work should include synthesizing core-shell particles of comparable small sizes.

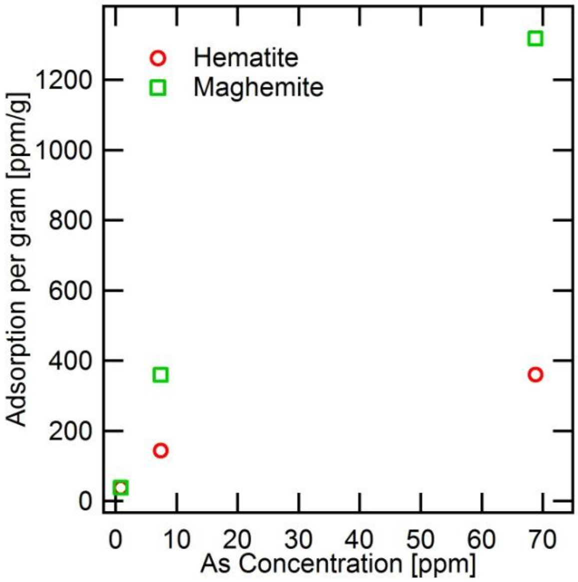

Figure 7.23. Arsenic uptake with respect to the initial arsenic concentration for core-shell nanoparticles.

7.5 Conclusions

The arsenic binding affinity and efficiency of arsenic removal for different phases of iron oxides and oxy-hydroxides has been investigated. Previously synthesized nanosized iron oxide and oxy-hydroxide particles were exposed to stock arsenite solutions of varying concentrations. Maghemite and hematite nanoparticle had a high arsenic removal affinity. Freundlich isotherms were calculated for maghemite nanoparticles and show over a 700% better adsorption efficiency than literature values[98d]. Because the maghemite particles were magnetic, we were also able to completely recover the adsorbent which promoted a surface regeneration study. We have shown that the synthesized particles were reusable after light base stripping. This exciting discovery coupled with the magnetic properties allows for this iron oxide mixture to be a reusable, easily recyclable arsenic remover.

Finally, we combined a non-magnetic removal phase, hematite, on a magnetic support, $CoFe_2O_4$, in a core-shell system to pursue the best removal efficiency with magnetic control of adsorbent. Both samples, hematite and maghemite core/shell particles, were exposed to various concentration of arsenite and maghemite core-shell particle were found to have the higher removal affinity. The higher affinity results from the difference in size between the core-shell nanoparticles with the maghemite derivative being 8 nm and the hematite derivative, 20 nm.

CHAPTER 8

REMOVAL OF OXO-ACIDS CONTAINMENTS, ARSENATE AND CHROMATE, USING IRON OXIDES AND OXY-HYRDOXIDES

8.1 Abstract

There are increasing interests in the removal of oxo-anion containments from water through the utilization of iron's affinity for oxo-acids. Nano-size iron oxides including goethite, maghemite, magnetite and hematite have been synthesized and characterized systematically. These nanoparticles were exposed to arsenate (As^{5+}) and chromate (Cr^{6+}) solutions to measure the percent uptake of containment by each phase of iron oxides. Nanoparticles were dispersed in the solutions for approximately 8 hours at room temperature. After agitation, a strong magnet was applied for 30 min to separate the particles from solution. The supernatant solutions were collected for analysis. Arsenic and chromium concentrations in the supernatant were measured using ICP-AES. Arsenic bound maghemite and chromium bound nanoparticles were characterized by PAS-IR, and XPS. All these methods show that the oxo-acid is chemically bound to the surface.

8.2 Introduction

The extraction of metals especially arsenic and chromium from water systems is essential due to the inherent toxicity. For solution phase, chelation is a highly efficient method to selectively remove toxic metal from the environment. However, for metal that form inorganic oxoanions, chelation cannot be used because there is no direct between the inorganic center and chelating agent. Even though there are numerous chelating agents for cations, very few extract anions from solution. Iron oxides have shown to remove oxoanions from solutions[117]. Research on these materials is primarily focused on arsenic removal but there may be the potential to remove other toxic adsorbates from the water supply.

One very toxic oxoanions is chromate (CrO_4^{2-}). Chromium is a carcinogen with both mutagenic and genotoxic affects[118]. When reduced in the body the reactive intermediates target and damage DNA[119]. Those molecules are using taken up into the body via general channel. Thus chromium uptake is especially severe in waters that have low salinities when the contaminant is present.

The primary sources of chromium contamination are anthropogenic. They originate from electroplating steel, textile industries and other metal processes[120]. Purifying of industrial waste water is challenging and costly due to the large volumes and multiple contaminants. Chromium can also enter the environment through leakage, poor storage or unapproved disposal procedures[121].

In this chapter, we study the removal affinity of iron oxides and oxy-hydroxides for different oxoanions, arsenate and chromate. This will help determine the affinity for oxoanions for the surface of these materials versus the affinity of Fe for As. Hopefully, iron oxides and oxy-hydroxide will prove beneficial from removing both hazardous contaminants from aqueous solutions.

8.3 Experimental

8.3.1 Arsenic and chromium stock solutions

Aqueous stock solutions (2 mM) were be made with an As(V) source, sodium hydrogen arsenate, and a Cr (VI) source, potassium chromate, dissolved in HPLC grade water. All samples were exposed to the same batch of As or Cr solution. The lower As and Cr concentrations (1 mM, 0.1 mM, and 0.01 mM) were all dilutions of their stock solutions with HPLC grade water. The exact concentration for each solution was determined by ICP-AES.

8.3.2 Different phase removal affinity comparison

For each sample, ~25 mg of nanoparticles were exposed to the arsenate and chromate (15 mL, 1 mM) solutions and agitated for 8 hrs. The samples were separated via a magnetic field or allowed to settle to isolate the particles from the supernatant which was collected for analysis. The solid was washed three times with HPLC grade water then allowed to dry in air. This collection procedure was performed for all contaminant exposed particles. Surface studies were performed on the particles using Photo-Acoustic Infrared Spectroscopy (PAS-IR) and X-ray Photoelectron Spectroscopy (XPS). Collected supernatant was analyzed for As and Cr content by ICP-AES without any modifications.

PAS-IR was taken on the exposed powder samples without any purification or preparation. Samples were purged with the carrier gas, He, in the instrument. XPS was also taken on the exposed powder samples which were placed in a vacuum oven overnight to remove any excess moisture or atmosphere gas.

8.3.3 Size Influence of Maghemite Nanoparticles on Arsenic and Chromium Adsorption

Each sample, ~25 mg of different sized maghemite nanoparticles (5 nm, 7 nm, and 10 nm) were exposed to 15 mL of three different arsenite concentrations (2 mM, 1 mM, and 0.1 mM) for 8 hrs. Collection of the particles was performed. ICP-AES was used to analyze the supernatant.

8.3.4 Surface Regeneration Study with Maghemite Nanoparticles

Two sizes of maghemite were exposed to As or Cr and regenerated several times. Maghemite nanoparticles (~50 mg) were weighed out in 30 mL beakers. The whole system was weighed then 15mL of arsenate or chromate (1 mM) was added. The particle-contaminant mixture was agitated overnight then the particles and supernatant were collected. After being washed with HPLC grade water, the exposed particles were regenerated with 1M NaOH solution for 2 hrs. Particles were collected and washed again and allowed to dry for 10 hrs. The dried system was re-weighed. The above procedure was repeated five times. All supernatants were submitted for analysis by ICP-AES as obtained.

8.4 Results and Discussion

8.4.1 Different phase removal affinity comparison

Different phases of iron oxides and oxy-hydroxides were all exposed to arsenate and chromate solutions to determine which had the highest arsenate and chromate affinities. Table 8.4. gives the results. Hematite and maghemite had the highest arsenic uptake while magnetite had the lowest. All maghemite nanoparticles synthesized had hematite impurities which may play a role in the arsenic removal ability of this material. Based on this information, studies were focused mainly on maghemite nanoparticles. It is clear that though iron oxides can to bind different oxy-acids, there is a preference for As.

Table 8.4. Contaminant uptake by different phases of iron oxides and oxy-hydroxides.

Phase	Cr^{6+} uptake per g NPs [ppm/g]	As^{5+} uptake per g NPs [ppm/g]
Goethite	0	149.59
Hematite	49.71	0
Maghemite	398.75	724.82
Magnetite	254.63	563.99

PAS-IR were performed on all iron oxide and oxy-hydroxide samples. Before and after exposure to contaminants, spectra were taken to try and determine the binding polyhedron structure from stretching frequencies. Changes in the spectra are seen, but we have not been able to correlate these stretching modes to the exact binding motif for the oxy-acid polyhedra. Shown below in Figure 8.1-8 are the PAS-IR spectra performed on the samples over the wavenumbers for oxo-acids stretching frequencies.

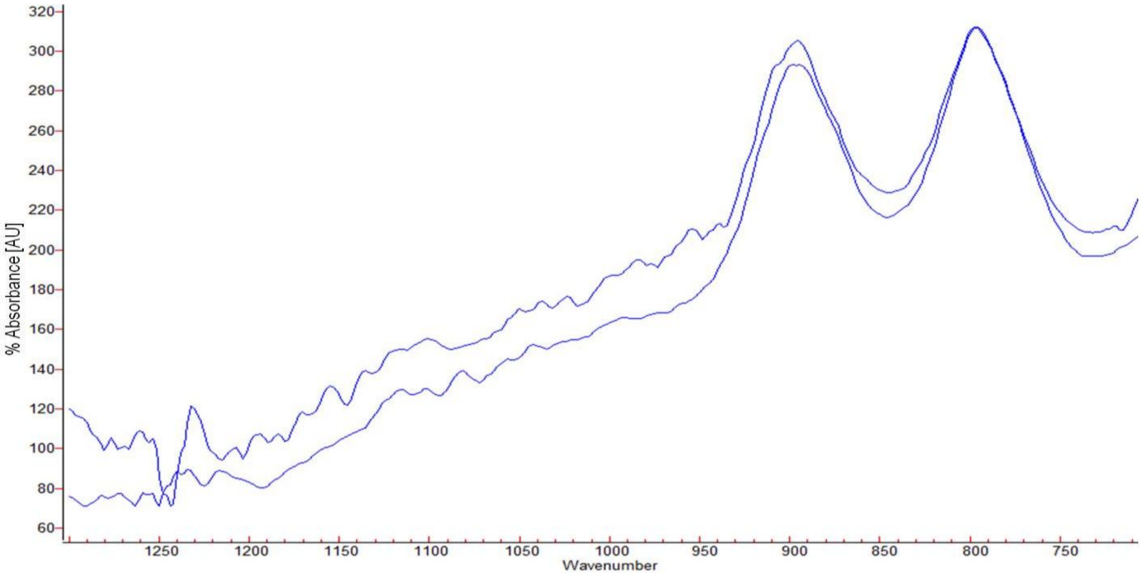

Figure 8.1. PAS-IR of goethite nanoparticle pure and Cr exposed overlaid.

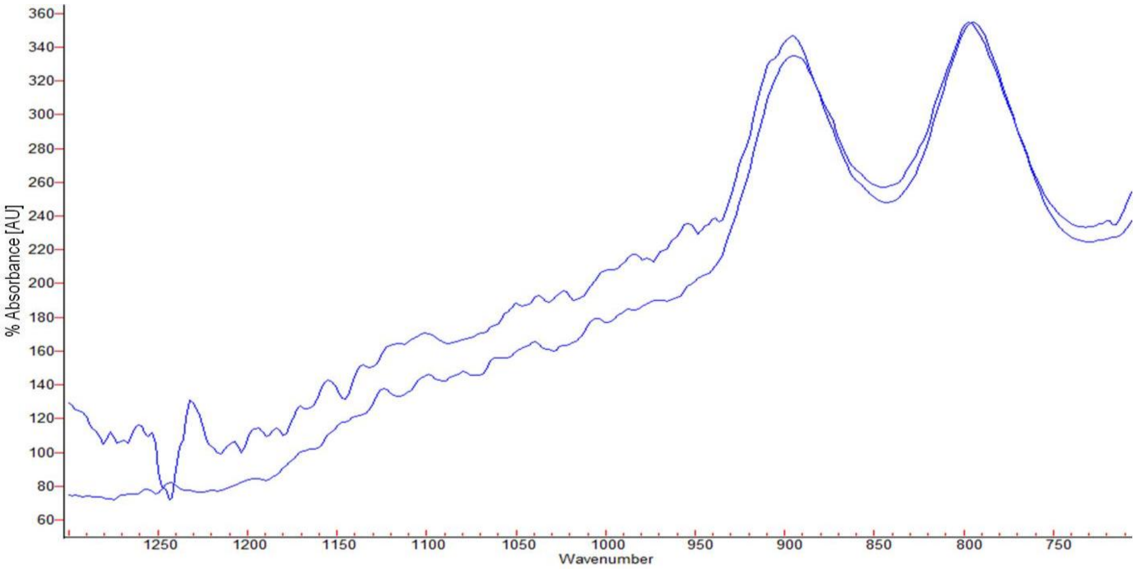

Figure 8.2. PAS-IR of goethite nanoparticle pure and As exposed overlaid.

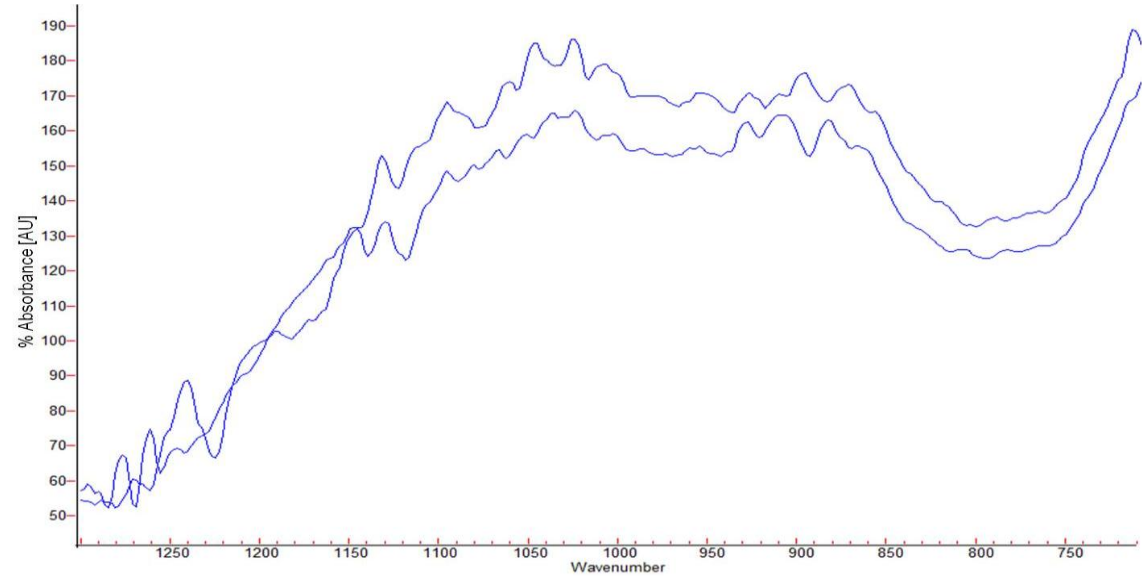

Figure 8.3. PAS-IR of hematite nanoparticle pure and Cr exposed overlaid.

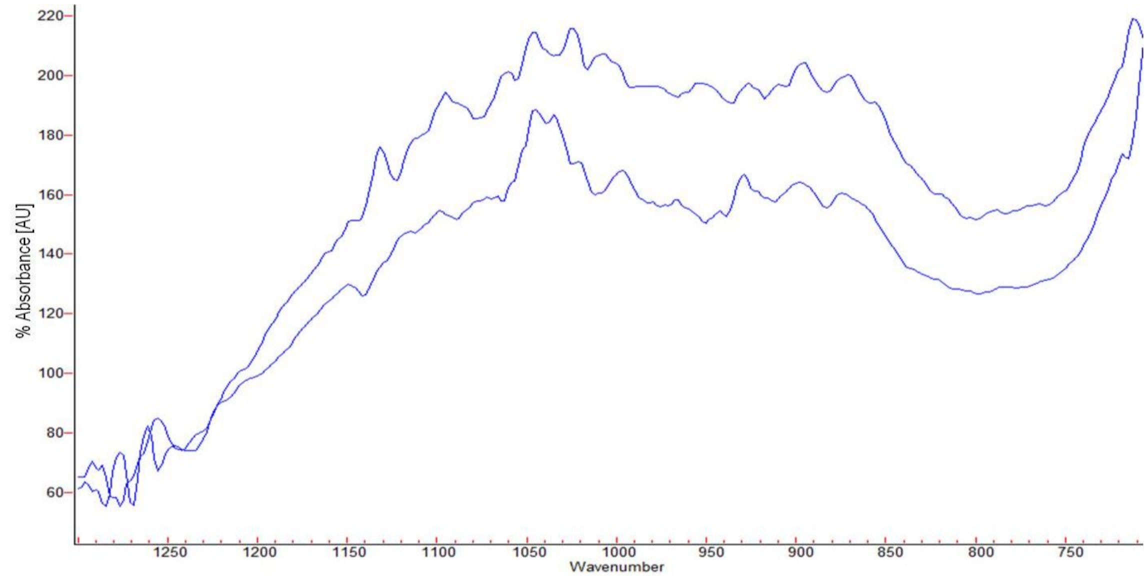

Figure 8.4. PAS-IR of hematite nanoparticle pure and As exposed overlaid.

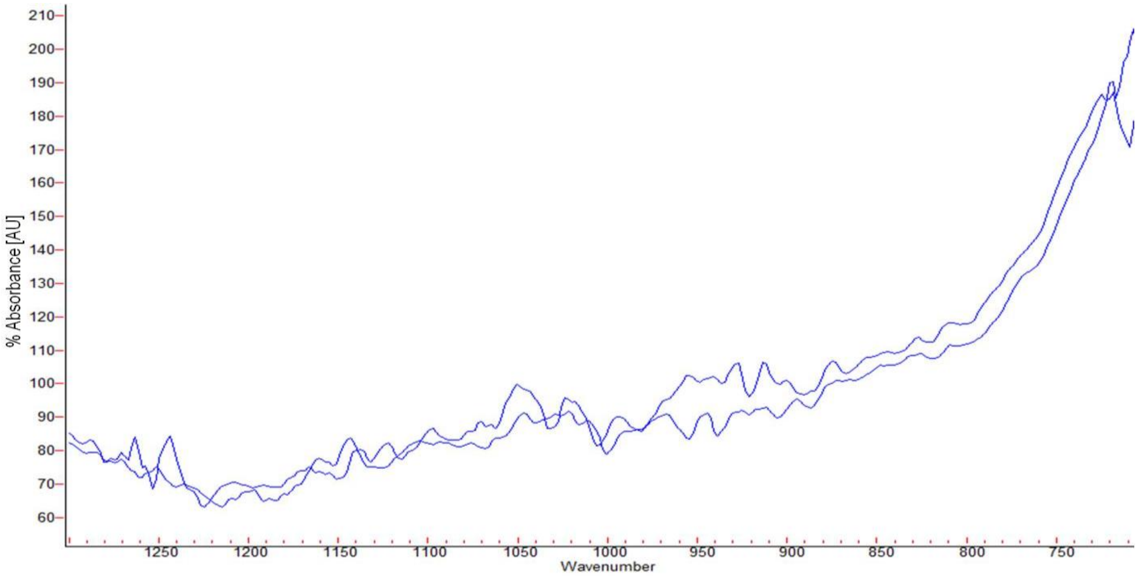

Figure 8.5. PAS-IR of maghemite nanoparticle pure and Cr exposed overlaid.

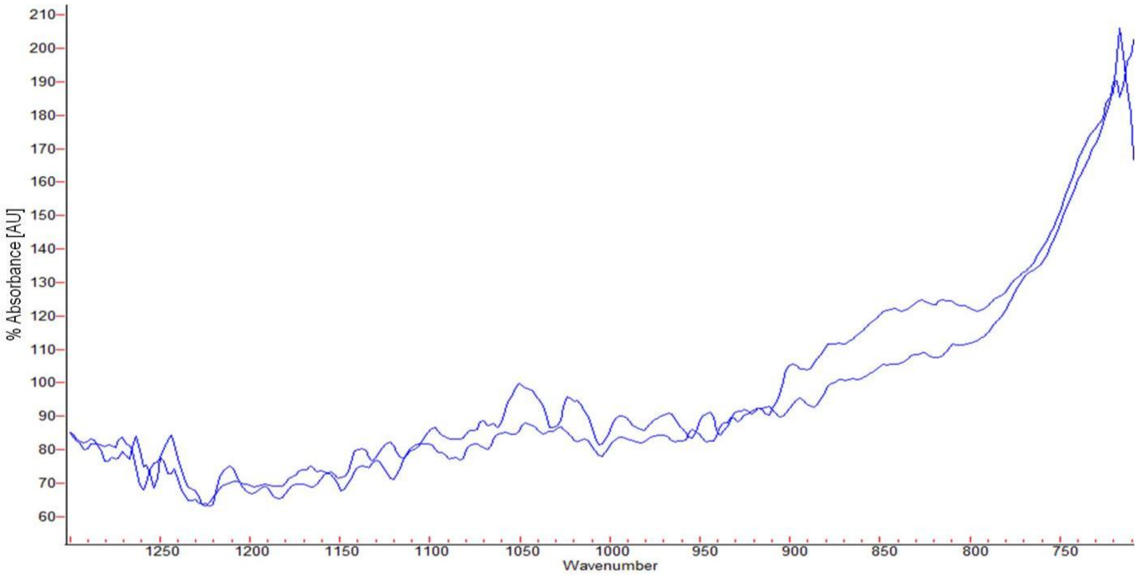

Figure 8.6. PAS-IR of maghemite nanoparticle pure and As exposed overlaid.

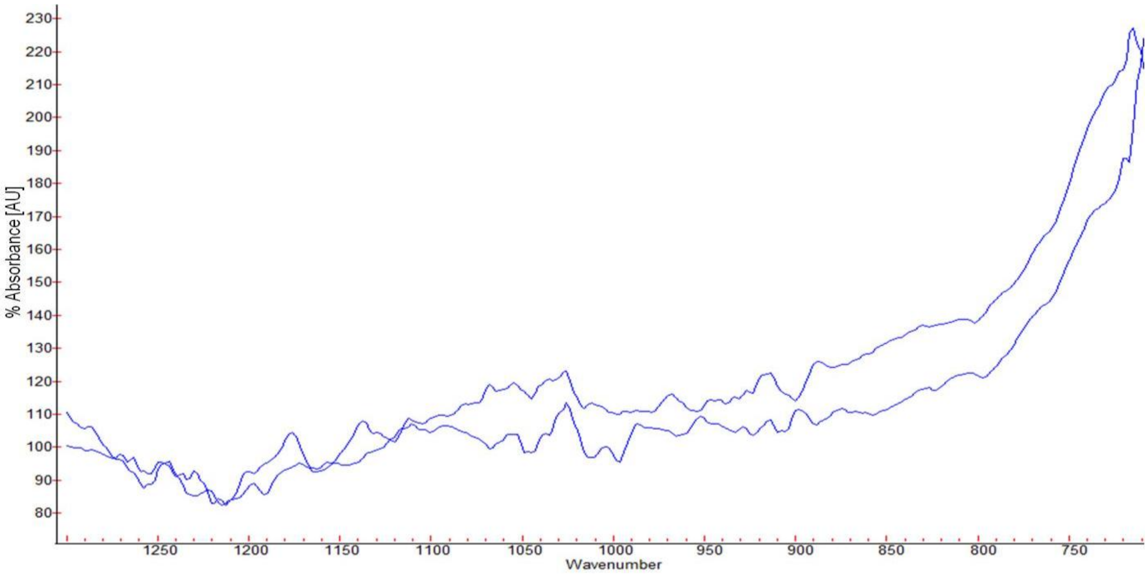

Figure 8.7. PAS-IR of magnetite nanoparticle pure and Cr exposed overlaid.

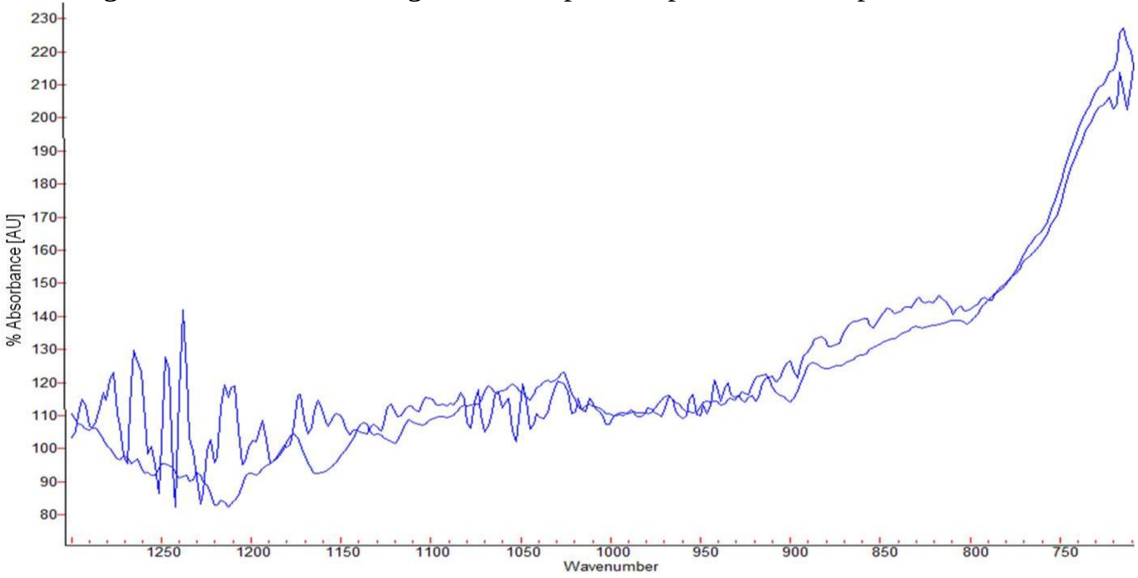

Figure 8.8. PAS-IR of magnetite nanoparticle pure and As exposed overlaid.

XPS was also taken on samples (Figure 8.9-15). Since the collected, exposed particles were washed with HPLC grade water several times before this characterization technique was performed, the presence of As and Cr confirms that contaminant is bound to the surface and not just removed via magnetic shearing or precipitation. The ratio of iron to arsenic in each of the phases is as follows: goethite 43:1, hematite 64:1, maghemite 13:1, and magnetite 21:1. For the chromate exposed particles the ratio were also calculated: goethite 127:1, maghemite 35:1, and magnetite 215:1.

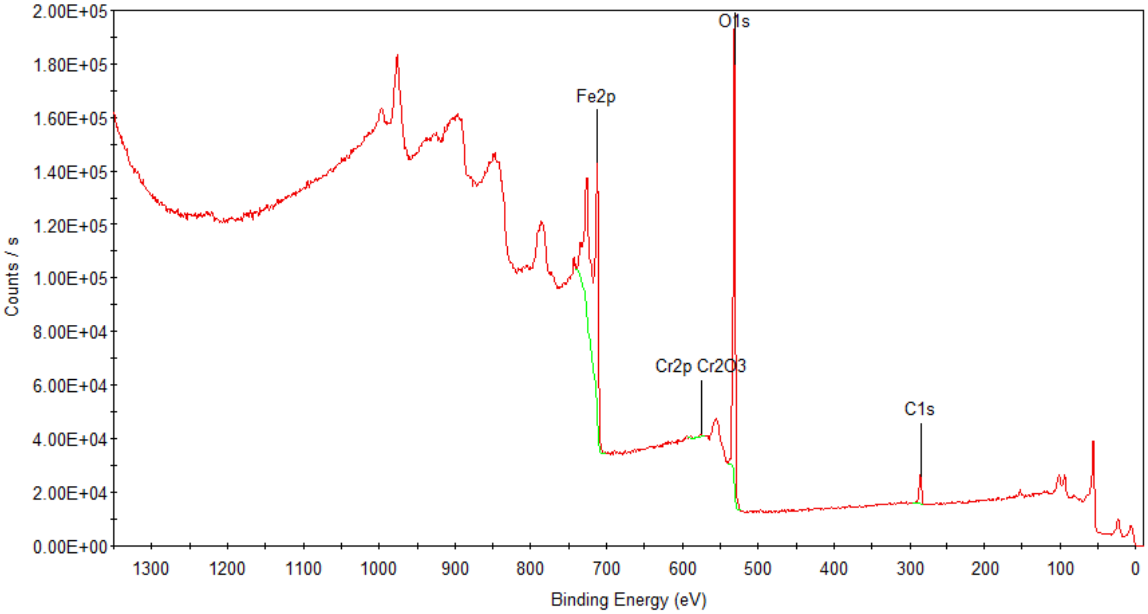

Figure8.9. XPS survey scan of Cr exposed goethite particles.

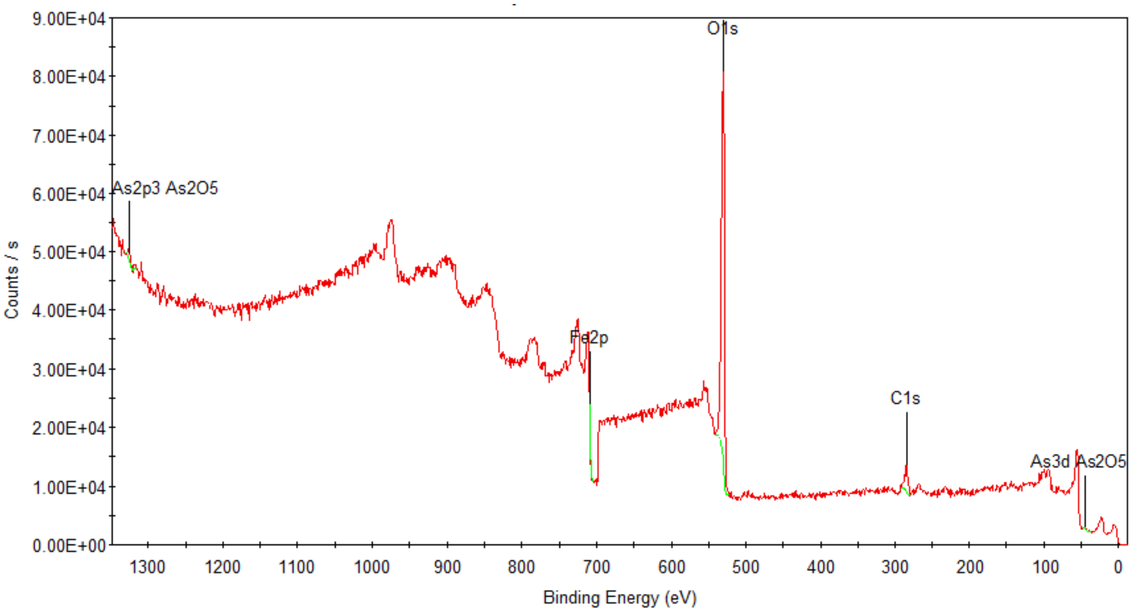

Figure8.10. XPS survey scan of As exposed goethite particles.

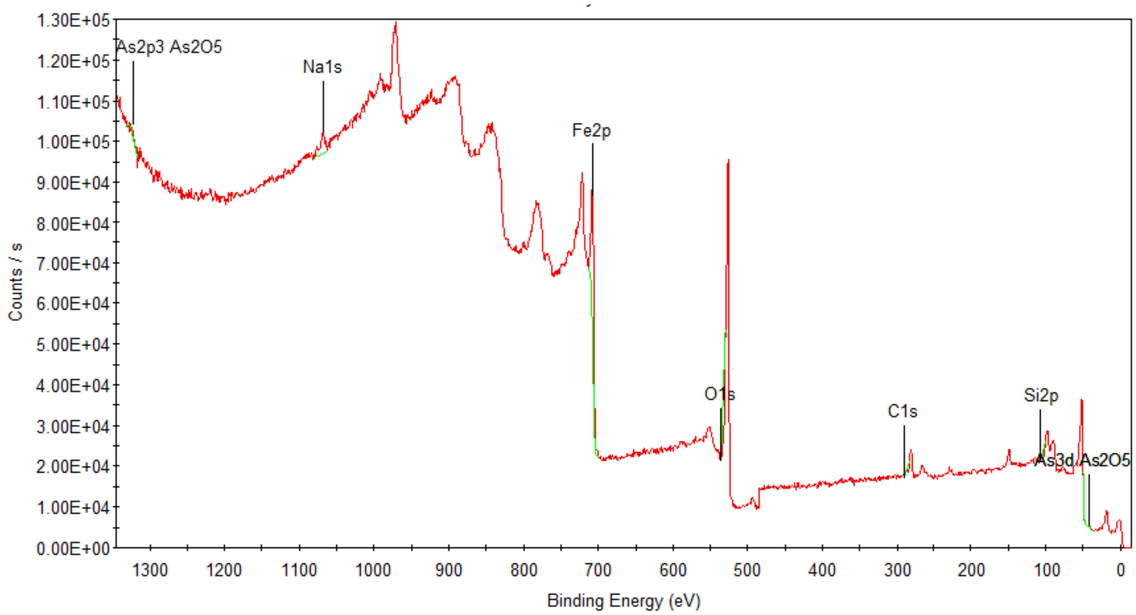

Figure 8.11. XPS survey scan of As exposed hematite particles.

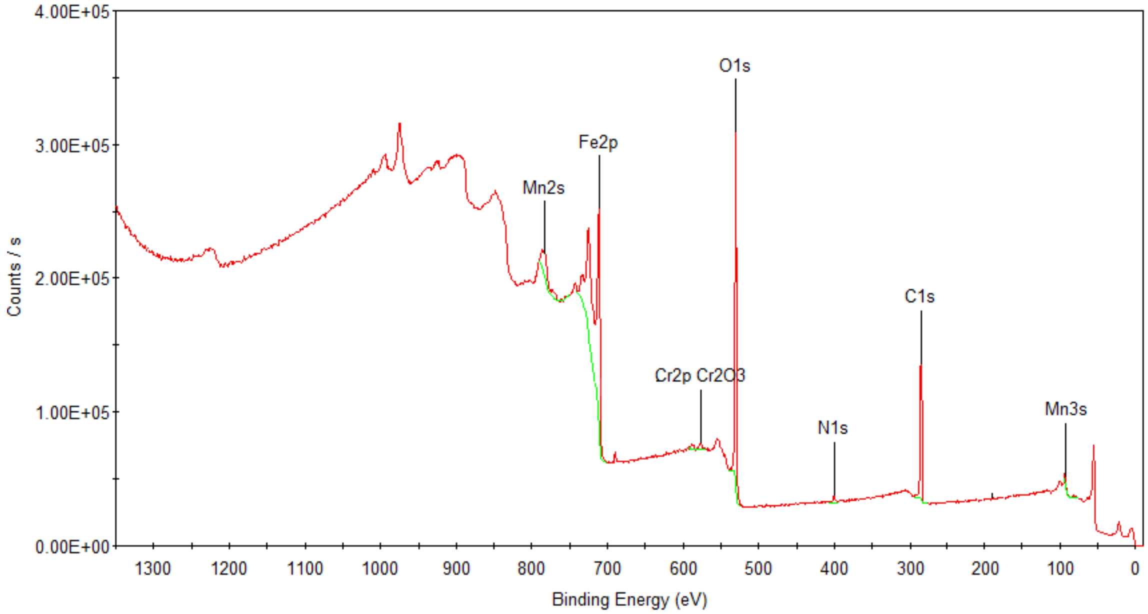

Figure 8.12. XPS survey scan of Cr exposed maghemite particles.

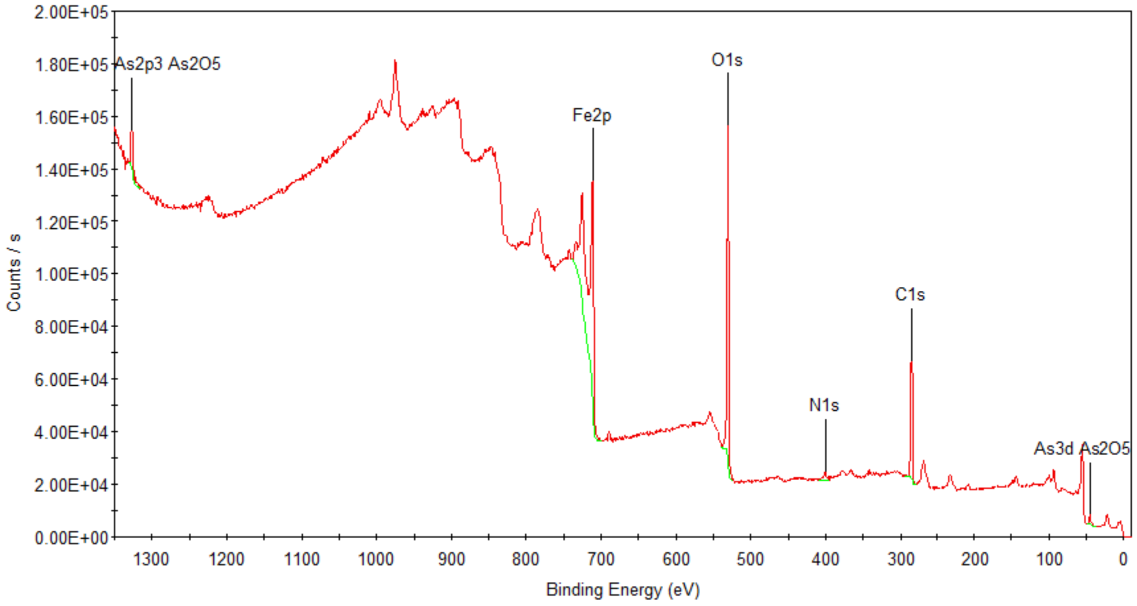

Figure 8.13. XPS survey scan of As exposed maghemite particles.

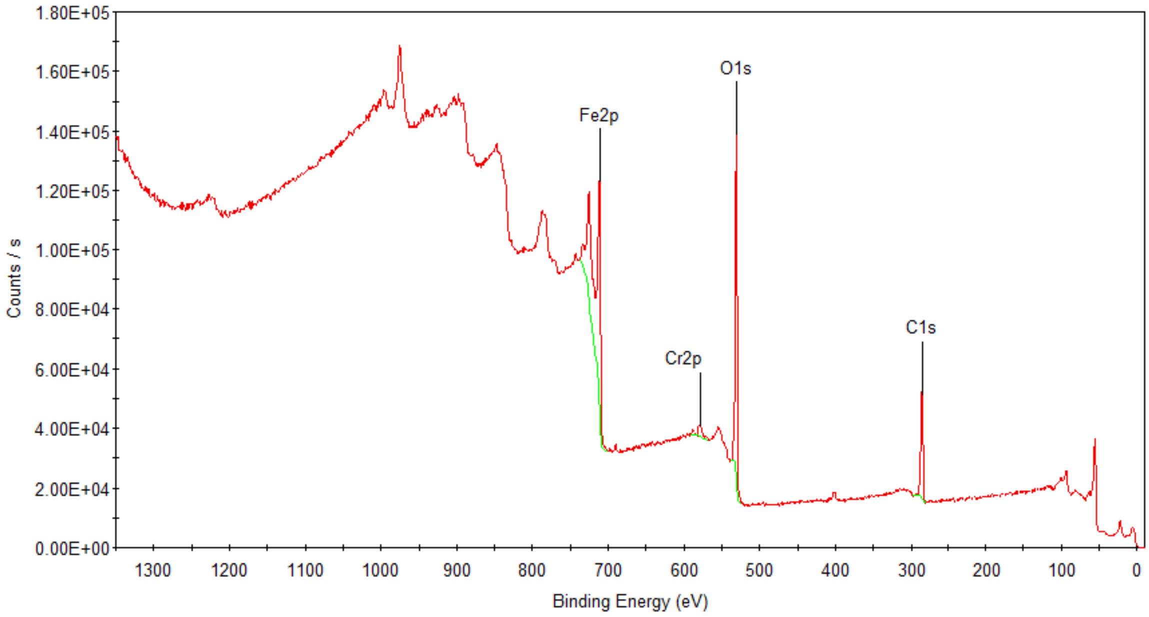

Figure 8.14. XPS survey scan of Cr exposed magnetite particles.

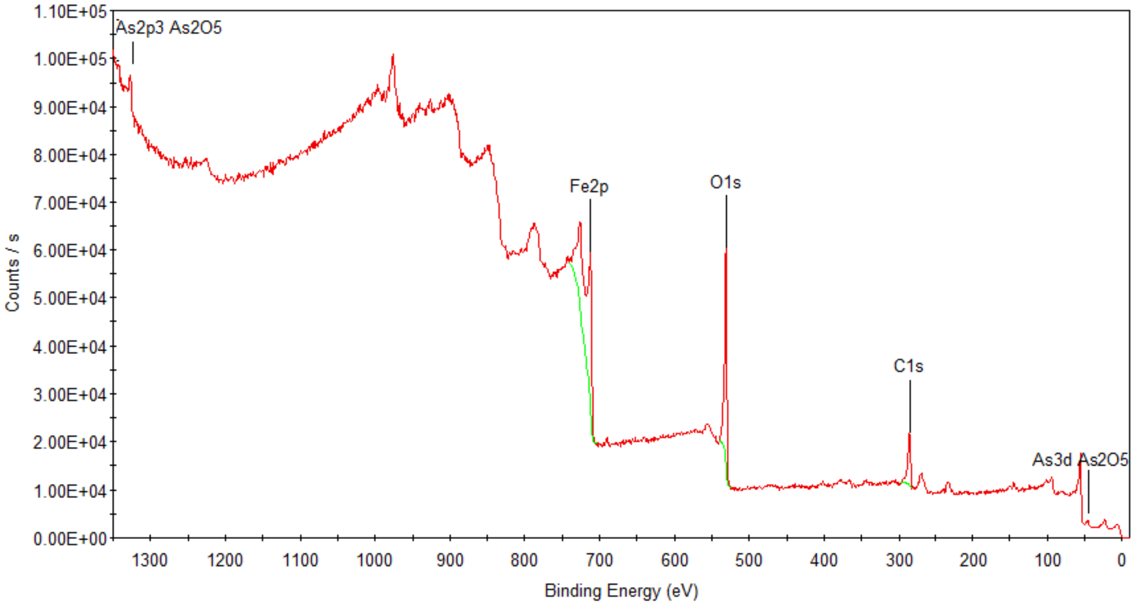

Figure 8.15. XPS survey scan of As exposed magnetite particles.

8.4.2 Size Influence of Maghemite Nanoparticles on Arsenic and Chromium Adsorption

Since adsorbance is the binding of contaminants to the surface of a material, size studies are extremely important. With nanoparticles even a small decrease in size can produce an appreciable increase in surface area when the same amount of sample is used. To determine this influence on arsenic and chromium uptake, various sized nanoparticles were exposed to three different concentrations of arsenate and chromate solutions. In Figures 8.16 and 8.17, the effects of size on uptake are plotted. The trends for both the arsenate and chromate are not as linear as previously reported for the arsenite data. While adsorption is dependent on agitation rate, these contaminants are also more pH dependent than arsenite thus adsorption is less favored. Also, the adsorption affinity between the contaminant and adsorbent might be lower especially in the Cr samples.

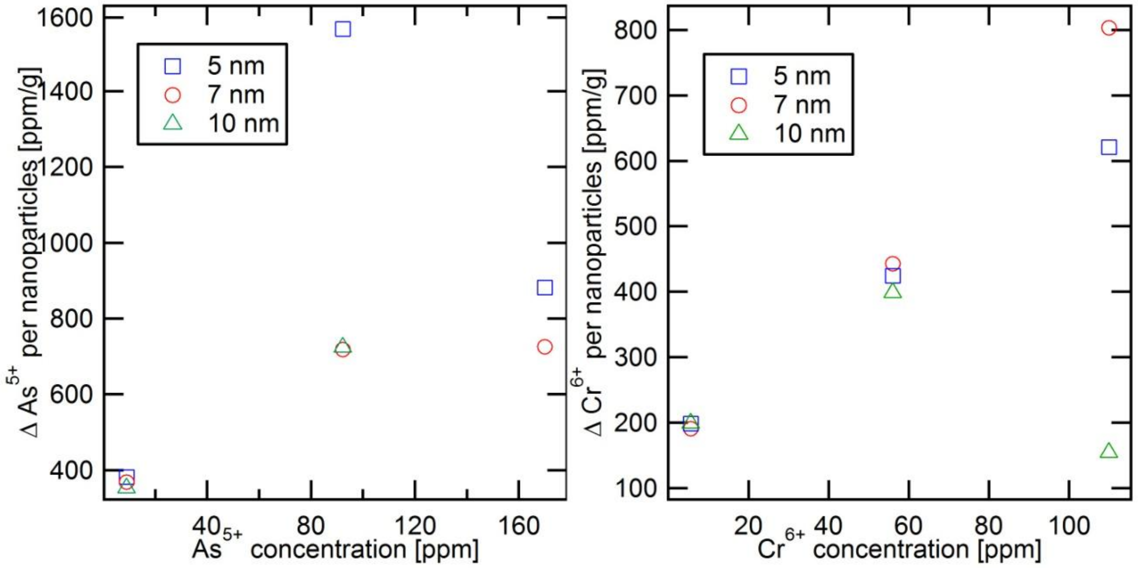

Figure 8.16. Arsenic and chromium uptake with respect to the initial arsenic concentration for various sized maghemite nanoparticles.

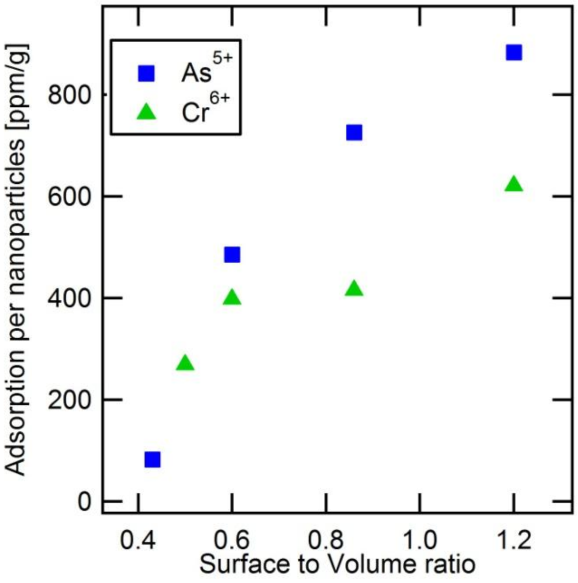

Figure 8.17. Arsenic and chromium uptake with respect to surface to volume ratio for maghemite nanoparticles.

8.4.3 Surface Regeneration Study with Maghemite Nanoparticles

During the investigation into the best arsenic removal phases, it was determined that the particle surface could be regenerated with base solution and that the particles would regain arsenic uptake. Since some of the iron oxides phases have magnetic properties that allow for the manipulation and direction of the adsorbent, it is simple to reclaim the particles after exposure. To fully exploit these properties, a surface regeneration study was performed to determine the number of regenerations that could be obtained from one sample of adsorbents.

For this part of the study, nanoparticles in beakers were weighed and exposed to arsenic and chromium solutions. After each exposure, the particle surface was regenerated by stripping solution and then re-exposed. Careful weight measurements were kept to account for any loss of adsorbents during washing and stripping. This stripping and re-exposure was repeated for five trials (Figure 8.18). Again, the smaller sized particles have the higher uptake, but since the smallest are similar in size, there is not much variation. Each successive regeneration of the particle's surface causes some loss in arsenic uptake. After five regenerations of the surface, the arsenic uptake drops significantly. This could be improved by stripping with a higher concentration of base or for a longer period of time, e.g. overnight. For the chromium regeneration study, there is an immediately loss in chromium affinity with surface regeneration. The next few regenerations have a small though steady chromium uptake ability. The fifth regeneration shows the highest uptake of chromium which could be attributed to finally achieve a thorough surface stripping.

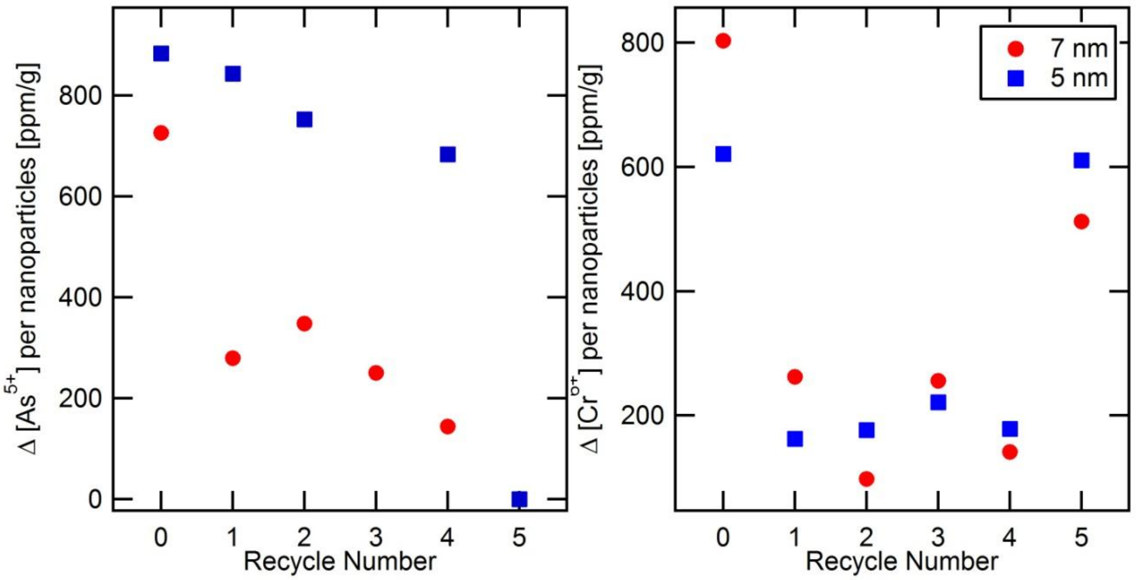

Figure 8.18. Arsenic and Chromium uptake with respect to recycle number for maghemite adsorbent.

8.5 Conclusion

We have explored remarkable affinity of different phases of iron oxides and oxy-hydroxides for the removal oxy-acid contaminants. The two contaminants evaluated where arsenate and chromate. Arsenate toxicity has already been discussed in the previous chapter as the basis for removal from global water systems. Chromates also poses an environmental and health hazardous so their binding affinity to the iron oxides and oxy-hydroxides is a benefit. However, the iron oxides especially maghemite will still have a greater affect on arsenic concentration than chromate.

REFERENCES

1. Service, R. F., Small Clusters Hit the Big Time. *Science* **1996,** *271*, 920-922.

2. Freestone, I., Meeks, N., Sax, M., and Higgit, C., The Lycurgus Cup - A Roman Nanotechnology. *Gold Bullentin* **2007,** *40* (4), 270.

3. Murray, C. B.; Norris, D. J.; Bawendi, M. G., Synthesis and characterization of nearly monodisperse CdE (E = sulfur, selenium, tellurium) semiconductor nanocrystallites. *Journal of the American Chemical Society* **1993,** *115* (19), 8706-8715.

4. Vestal, C. R.; Zhang, Z. J., Effects of Surface Coordination Chemistry on the Magnetic Properties of MnFe2O4 Spinel Ferrite Nanoparticles. *Journal of the American Chemical Society* **2003,** *125* (32), 9828-9833.

5. Kikuchi, Y., Magnetostrictive materials and applications. *Magnetics, IEEE Transactions on* **1968,** *4* (2), 107-117.

6. Zhukov, A.; Cobeño, A. F.; Gonzalez, J.; Blanco, J. M.; Aragoneses, P.; Dominguez, L., Magnetoelastic sensor of liquid level based on magnetoelastic properties of Co-rich microwires. *Sensors and Actuators A: Physical* **2000,** *81* (1-3), 129-133.

7. (a) Bhame, S. D. a. J., P. A., Tuning of the magnetostrictive properties of $CoFe_2O_4$ by Mn substitution for Co. *Journal of Applied Physics* **2006,** *100*, 113911-1-113911-4; (b) McCallum, R. W., Dennis, K. W., Jiles, D. C., Snyder, J. E., and Chen, Y. H. , Composite magnetostrictive materials for advance automotive magnetomechanical sensors. *Low Temperature Physics* **2001,** *27* (4), 266-274.

8. Greenough, R. D.; Jenner, A. G. I.; Schulze, M. P.; Wilkinson, A. J., The properties and applications of magnetostrictive rare-earth compounds. *Journal of Magnetism and Magnetic Materials* **1991,** *101* (1-3), 75-80.

9. Scarberry, K. E.; Dickerson, E. B.; McDonald, J. F.; Zhang, Z. J., Magnetic Nanoparticle−Peptide Conjugates for in Vitro and in Vivo Targeting and Extraction of Cancer Cells. *Journal of the American Chemical Society* **2008,** *130* (31), 10258-10262.

10. Manning, B. A.; Hunt, M. L.; Amrhein, C.; Yarmoff, J. A., Arsenic(III) and Arsenic(V) Reactions with Zerovalent Iron Corrosion Products. *Environmental Science & Technology* **2002,** *36* (24), 5455-5461.

11. Fecht, H. J., Nanostructure formation by mechanical attrition. *Nanostructured Materials* **1995,** *6* (1-4), 33-42.

12. Roca, A. G.; et al., Progress in the preparation of magnetic nanoparticles for applications in biomedicine. *Journal of Physics D: Applied Physics* **2009,** *42* (22), 224002.

13. (a) Manova, E.; Kunev, B.; Paneva, D.; Mitov, I.; Petrov, L.; Estournès, C.; D'Orléan, C.; Rehspringer, J.-L.; Kurmoo, M., Mechano-Synthesis, Characterization, and Magnetic Properties of Nanoparticles of Cobalt Ferrite, CoFe2O4. *Chemistry of Materials* **2004,** *16* (26), 5689-5696; (b) Mahmoud, M. H.; Hamdeh, H. H.; Ho, J. C.; O'Shea, M. J.; Walker, J. C., Mössbauer studies of manganese ferrite fine particles processed by ball-milling. *Journal of Magnetism and Magnetic Materials* **2000,** *220* (2-3), 139-146.

14. Tavakoli, A.; Sohrabi, M.; Kargari, A., A review of methods for synthesis of nanostructured metals with emphasis on iron compounds. *Chemical Papers* **2007,** *61* (3), 151-170.

15. Pardavi-Horvath, M.; Takacs, L., Magnetic nanocomposites by reaction milling. *Scripta Metallurgica et Materialia* **1995,** *33* (10-11), 1731-1740.

16. Rao, K. H., Raju, S. B., Aggarwal, K., and Mendiratta, R. G., Effect of Cr impurity on the dc resistivity of Mn-Zn ferrites. *Journal of Applied Physics* **1981,** *52* (3), 1376-1379.

17. Aruna, S. T. a. M., A. S., Combustion synthesis and nanomaterials. *Current Opinion in Solid State and Materials Science* **2008,** *12,* 44-55.

18. Mimani, T. a. P., K. C., Solution Combustion Synthesis of Nanoscale Oxides and Their Composites. *Mater. Phys. Mech.* **2001,** *4*, 134-137.

19. Tyagi, A. K., Combustion synthesis: a soft-chemical route for functional nano-ceramics. *BARC Newsletter* **2007,** (285), 39-48.

20. Costa, A. C. F. M.; Silva, V. J.; Ferreira, H. S.; Costa, A. A.; Cornejo, D. R.; Kiminami, R. H. G. A.; Gama, L., Structural and magnetic properties of chromium-doped ferrite nanopowders. *Journal of Alloys and Compounds* **2009,** *483* (1-2), 655-657.

21. Kambale, R. C.; et al., The effect of Mn substitution on the magnetic and dielectric properties of cobalt ferrite synthesized by an autocombustion route. *Smart Materials and Structures* **2009,** *18* (11), 115028.

22. Ghosh, N. N.; Pramanik, P., Aqueous sol-gel synthesis of nanosized ceramic composite powders with metal-formate precursors. *Materials Science and Engineering: C* **2001,** *16* (1-2), 113-117.

23. Teja, A. S., and Koh, P-K., Synthesis, Properties, and applications of magnetic iron oxide nanoparticles. *Progress in Crystal Growth and Characterization of Materials* **2009,** *55*, 22-45.

24. Kim, C. S.; Yi, Y. S.; Park, K.-T.; Namgung, H.; Lee, J.-G., Growth of ultrafine Co--Mn ferrite and magnetic properties by a sol--gel method. *Journal of Applied Physics* **1999,** *85* (8), 5223-5225.

25. Liu, C.; Zhang, Z. J., Size-Dependent Superparamagnetic Properties of Mn Spinel Ferrite Nanoparticles Synthesized from Reverse Micelles. *Chemistry of Materials* **2001,** *13* (6), 2092-2096.

26. Vestal, C. R.; Zhang, Z. J., Synthesis of CoCrFeO4 Nanoparticles Using Microemulsion Methods and Size-Dependent Studies of Their Magnetic Properties. *Chemistry of Materials* **2002,** *14* (9), 3817-3822.

27. (a) Song, Q.; Ding, Y.; Wang, Z. L.; Zhang, Z. J., Tuning the Thermal Stability of Molecular Precursors for the Nonhydrolytic Synthesis of Magnetic MnFe2O4 Spinel Nanocrystals. *Chemistry of Materials* **2007,** *19* (19), 4633-4638; (b) Song, Q.; Zhang, Z.

J., Shape Control and Associated Magnetic Properties of Spinel Cobalt Ferrite Nanocrystals. *Journal of the American Chemical Society* **2004,** *126* (19), 6164-6168.

28. Hyeon, T.; Lee, S. S.; Park, J.; Chung, Y.; Na, H. B., Synthesis of Highly Crystalline and Monodisperse Maghemite Nanocrystallites without a Size-Selection Process. *Journal of the American Chemical Society* **2001,** *123* (51), 12798-12801.

29. Sun, S.; Zeng, H., Size-Controlled Synthesis of Magnetite Nanoparticles. *Journal of the American Chemical Society* **2002,** *124* (28), 8204-8205.

30. Song, Q.; Zhang, Z. J., Correlation between Spin−Orbital Coupling and the Superparamagnetic Properties in Magnetite and Cobalt Ferrite Spinel Nanocrystals. *The Journal of Physical Chemistry B* **2006,** *110* (23), 11205-11209.

31. Zhang, Z.; Liu, S.; Chow, S.; Han, M.-Y., Modulation of the Morphology of ZnO Nanostructures via Aminolytic Reaction: From Nanorods to Nanosquamas. *Langmuir* **2006,** *22* (14), 6335-6340.

32. (a) Ebsworth, E. A. V., Rankin, D. W. H., Cradock, S., *Structural Methods in Inorganic Chemistry*. 1 ed.; Blackwell Scientific Publication: Oxford, 1987; (b) Skoog, D. A., Joller, F. J., and Nieman, T. A., *Principles of Instrumental Analysis*. 5 ed.; Thomson Learning, Inc.: 1998.

33. Cullity, B. D., *Elements of X-ray Diffraction*. 2 ed.; Addison-Welsey: 1977.

34. Glusker, J. P., Lewis, M., and Rosi, M., Crystal Structure Analysis for Chemists and Biologists. Wiley-Vch: 1994.

35. (a) Giacovazzo, C., *Fundamentals of Crystallography*. 2 ed.; Oxford University Press: Oxford, 2002; (b) Pecharsky, V. K. a. Z., P. Y., *Fudamentals of Powder Diffraction and Structural Characterization of Materials*. Kluwer Academica Publishers: Boston, 2003.

36. Smart, L. E., and Moore, E. A., *Solid State Chemistry*. 3 ed.; Taylor & Francis Group: Boca Raton, 2005.

37. Patterson, A. L., The Scherrer Formula for X-Ray Particle Size Determination. *Physical Review* **1939,** *56* (10), 978.

38. (a) Wang, Z. L., Structural Analysis of Self-Assembling Nanocrystal Superlattices. *Advanced Materials* **1998,** *10* (1), 13-30; (b) Wang, Z. L., *Elastic and Inelastic Scattering in Electron Diffraction and Imaging*. Plenum Press: New York, 1995.

39. Josephson, B. D., The Discovery of Tunneling Supercurrents. *Science* **1974,** *184* (4136), 527-530.

40. Barone, A., and Paterno, G., *Physics and Applications of the Josephson Effect*. John Wiley & Sons: New York, 1982.

41. Rondinone, A. J. a. Z., Z. J., Magnetic Characterization. *Handbook of Nanophase and Nanostructured Materials* **2003,** *2*, 252-282.

42. Michaelian, K. H., *Photoacoustic Infrared Spectroscopy*. John Wiley & Sons, Inc.: Hoboken, 2003; Vol. 159.

43. Perrett, B., Harris, M., Pearson, G. N., Willets, D. V., and Pitter, M. C., Remote photoacoustic detection of liquid contamination of a surface. *Applied Optics* **2003,** *42* (24), 4901-4908.

44. Spinel. http://super.gsnu.ac.kr/lecture/inorganic/spinel.html (accessed 1 March).

45. Smart, L. E., and Moore, E. A., *Solid State Chemistry: An Introduction*. 3rd ed.; Taylor & Francis Group: Boca Raton, 2005; p 407.

46. Shriver, D. a. A., P., *Inorganic Chemistry*. 3 ed.; W. H. Freeman and Company: New York, 1999.

47. Frenkel, J. a. D., J., Spontaneous and Induced Magnetisation in Ferromagnetic Bodies. *Nature* **1930,** *126* (3173), 274.

48. Leslie-Pelecky, D. L.; Rieke, R. D., Magnetic Properties of Nanostructured Materials. *Chemistry of Materials* **1996,** *8* (8), 1770-1783.

49. Neel, L., *Ann. Geophys. (C.N.R.S.)* **1949,** *5*, 99.

50. Bean, C. P. a. L., J. D., Superparamagnetism. *Journal of Applied Physics* **1959,** *30* (4), s120-s129.

51. Jun, Y.-w.; Seo, J.-w.; Cheon, J., Nanoscaling Laws of Magnetic Nanoparticles and Their Applicabilities in Biomedical Sciences. *Accounts of Chemical Research* **2008,** *41* (2), 179-189.

52. Liu, C.; Zou, B.; Rondinone, A. J.; Zhang, Z. J., Chemical Control of Superparamagnetic Properties of Magnesium and Cobalt Spinel Ferrite Nanoparticles through Atomic Level Magnetic Couplings. *Journal of the American Chemical Society* **2000,** *122* (26), 6263-6267.

53. Dormann, J. L., Fiorani, D., and Tronc, E. , *Mangetic Relaxation in Fine-Particle Sytems*. John Wiley & Sons, Inc.: 1997; Vol. XCVIII.

54. Stoner, E. C.; Wohlfarth, E. P., A mechanism of magnetic hysteresis in heterogeneous alloys. *Magnetics, IEEE Transactions on* **1991,** *27* (4), 3475-3518.

55. Solzi, M., *Fundamental Properties of Nanostructured Materials*. World Scientific: River Edge, NJ, 1994.

56. Neel, L., *J. Phys. Radium* **1954,** *15*, 225.

57. Batlle, X.; Labarta, A., Finite-size effects in fine particles: magnetic and transport properties. *Journal of Physics D: Applied Physics* **2002,** *35* (6), R15.

58. Kodama, R. H., Magnetic nanoparticles. *Journal of Magnetism and Magnetic Materials* **1999,** *200* (1-3), 359-372.

59. Dimitrov, D. A.; Wysin, G. M., Effects of surface anisotropy on hysteresis in fine magnetic particles. *Physical Review B* **1994,** *50* (5), 3077.

60. Broese van Groenou, A.; Bongers, P. F.; Stuyts, A. L., Magnetism, microstructure and crystal chemistry of spinel ferrites. *Materials Science and Engineering* **1969,** *3* (6), 317-392.

61. Blaum, A. Determination of the g-Factor of the bound Electron in hydrogen-like Calcium. http://www.quantum.physik.uni-mainz.de/mats/experiments/g-factor-ca/index.html (accessed 1 March).

62. Han, M., Vestal, C. R., and Zhang, Z. J., Quantum Couplings and Magnetic Properties of CoCrxFe2-xO4 (O<x<1) Spinel Ferrites Nanoparticles Synthesized with Reverse Micelle Method. *Journal of Physical Chemistry B* **2004,** *108*, 583-587.

63. Patange, S. M., Shirsath, S. E., Toksha, B. G., Jadhav, S. S., and Jadhav, K. M., Electrical and magnetic properties of Cr3+ substituted nanocrystalline nickel ferrite. *Journal of Applied Physics* **2009,** *106*, 023914-1-023914-7.

64. (a) Sun, S.; Murray, C. B.; Weller, D.; Folks, L.; Moser, A., Monodisperse FePt Nanoparticles and Ferromagnetic FePt Nanocrystal Superlattices. *Science* **2000,** *287* (5460), 1989-1992; (b) Harasawa, T.; Suzuki, R.; Shimizu, O.; Olcer, S.; Eleftheriou, E., Barium-Ferrite Particulate Media for High-Recording-Density Tape Storage Systems. *Magnetics, IEEE Transactions on* **2010,** *46* (6), 1894-1897.

65. (a) Raj, K.; Moskowitz, B.; Casciari, R., Advances in ferrofluid technology. *Journal of Magnetism and Magnetic Materials* **1995,** *149* (1-2), 174-180; (b) Lòpez, J. L.; Pfannes, H. D.; Paniago, R.; Tourinho, F. A., Influence of particle size on superparamagnetic relaxation of MnFe2O4 particles in ferrofluids. *Journal of Magnetism and Magnetic Materials* **2001,** *226-230* (Part 2), 1878-1880.

66. (a) Mitchell, D. G., MR imaging contrast agents--what's in a name?. *Journal of magnetic resonance imaging* **1997,** *7* (1), 1-4; (b) Kim, D.-H.; Zeng, H.; Ng, T. C.; Brazel, C. S., T1 and T2 relaxivities of succimer-coated MFe23+O4 (M=Mn2+, Fe2+ and Co2+) inverse spinel ferrites for potential use as phase-contrast agents in medical MRI. *Journal of Magnetism and Magnetic Materials* **2009,** *321* (23), 3899-3904.

67. (a) Matsumoto, T.; Nakamura, K.; Nishida, T.; Hieda, H.; Kikitsu, A.; Naito, K.; Koda, T., Thermally assisted magnetic recording on a bit-patterned medium by using a near-field optical head with a beaked metallic plate. *Applied Physics Letters* **2008,** *93* (3), 031108; (b) Srinivasan, G.; Bichurin, M. I.; Mantese, J. V., FERROMAGNETIC-FERROELECTRIC LAYERED STRUCTURES: MAGNETOELECTRIC INTERACTIONS AND DEVICES. *Integrated Ferroelectrics* **2005,** *71* (1), 45-57.

68. (a) Caltun, O.; Dumitru, I.; Feder, M.; Lupu, N.; Chiriac, H., Substituted cobalt ferrites for sensors applications. *Journal of Magnetism and Magnetic Materials* **2008,** *320* (20), e869-e873; (b) Paulsen, J. A.; Ring, A. P.; Lo, C. C. H.; Snyder, J. E.; Jiles, D. C., Manganese-substituted cobalt ferrite magnetostrictive materials for magnetic stress sensor applications. *Journal of Applied Physics* **2005,** *97* (4), 044502.

69. Kim, D.-H.; Nikles, D. E.; Johnson, D. T.; Brazel, C. S., Heat generation of aqueously dispersed CoFe2O4 nanoparticles as heating agents for magnetically activated drug delivery and hyperthermia. *Journal of Magnetism and Magnetic Materials* **2008,** *320* (19), 2390-2396.

70. (a) El-Okr, M. M.; Salem, M. A.; Salim, M. S.; El-Okr, R. M.; Ashoush, M.; Talaat, H. M., Synthesis of cobalt ferrite nano-particles and their magnetic characterization. *Journal of Magnetism and Magnetic Materials* **2011,** *323* (7), 920-926; (b) Hasegawa, K. i.; Sato, T., Particle-Size Distribution of CoFe[sub 2]O[sub 4] Formed by the Coprecipitation Method. *Journal of Applied Physics* **1967,** *38* (12), 4707-4713.

71. (a) Zhao, L.; Zhang, H.; Xing, Y.; Song, S.; Yu, S.; Shi, W.; Guo, X.; Yang, J.; Lei, Y.; Cao, F., Studies on the magnetism of cobalt ferrite nanocrystals synthesized by hydrothermal method. *Journal of Solid State Chemistry* **2008,** *181* (2), 245-252; (b) Zhen, L.; He, K.; Xu, C. Y.; Shao, W. Z., Synthesis and characterization of single-crystalline MnFe2O4 nanorods via a surfactant-free hydrothermal route. *Journal of Magnetism and Magnetic Materials* **2008,** *320* (21), 2672-2675; (c) Hou, X.; Feng, J.; Xu, X.; Zhang, M., Synthesis and characterizations of spinel MnFe2O4 nanorod by seed-hydrothermal route. *Journal of Alloys and Compounds* **2010,** *491* (1-2), 258-263.

72. Moumen, N.; Pileni, M. P., New Syntheses of Cobalt Ferrite Particles in the Range 2−5 nm: Comparison of the Magnetic Properties of the Nanosized Particles in Dispersed Fluid or in Powder Form. *Chemistry of Materials* **1996,** *8* (5), 1128-1134.

73. (a) Xiong, G.; Mai, Z.; Xu, M.; Cui, S.; Ni, Y.; Zhao, Z.; Wang, X.; Lu, L., Preparation and Magnetic Properties of CoCrFeO4 Nanocrystals. *Chemistry of Materials* **2001,** *13* (6), 1943-1945; (b) Gul, I. H.; Maqsood, A., Structural, magnetic and electrical

properties of cobalt ferrites prepared by the sol-gel route. *Journal of Alloys and Compounds* **2008,** *465* (1-2), 227-231; (c) Monros, G.; Cards, J.; Tena, M. A.; Escribano, P.; Badenes, J.; Cordoncillo, E., Spinets from gelatine-protected gels. *Journal of Materials Chemistry* **1995,** *5* (1), 85-90; (d) Li, J.; Yuan, H.; Li, G.; Liu, Y.; Leng, J., Cation distribution dependence of magnetic properties of sol-gel prepared MnFe2O4 spinel ferrite nanoparticles. *Journal of Magnetism and Magnetic Materials* **2010,** *322* (21), 3396-3400.

74. Gabal, M. A.; Ata-Allah, S. S., Concerning the cation distribution in MnFe2O4 synthesized through the thermal decomposition of oxalates. *Journal of Physics and Chemistry of Solids* **2004,** *65* (5), 995-1003.

75. Vestal, C. R.; Zhang, Z. J., Synthesis and Magnetic Characterization of Mn and Co Spinel Ferrite-Silica Nanoparticles with Tunable Magnetic Core. *Nano Letters* **2003,** *3* (12), 1739-1743.

76. (a) Denecke, M. A.; Gunßer, W.; Buxbaum, G.; Kuske, P., Manganese valence in precipitated manganese ferrite. *Materials Research Bulletin* **1992,** *27* (4), 507-514; (b) Tailhades, P.; Rousset, A.; Bendaoud, R.; Fert, A. R.; Gillot, B., Structural study of new manganese defect ferrites. *Materials Chemistry and Physics* **1987,** *17* (6), 521-529; (c) Novak, P., Roskove, V., Simsa, Z., and Brabers, V. A. M., Effect of Mn3+ ion orbit lattice coupling on magnetic anisotropy of MnxFe3-xO4. *Journel de Physique, Colloque* **1971,** *1*, CI-59-CI-61.

77. Wykoff, R. W. G., *Crystal Structures*. Interscience Pub.: London, 1965; Vol. 3.

78. Chen, J. P.; Sorensen, C. M.; Klabunde, K. J.; Hadjipanayis, G. C.; Devlin, E.; Kostikas, A., Size-dependent magnetic properties of MnFe_{2}O_{4} fine particles synthesized by coprecipitation. *Physical Review B* **1996,** *54* (13), 9288.

79. (a) Yasuoka, H., Hirai, A., Sinjo, T., Kiyama, M., Bando, Y., and Takada, T., NMR Determination of Metal Ion Distribution in Manganese Ferrite Prepared from Aqueous Solution. *Journal of the Physical Society of Japan* **1967,** *22* (1), 174-180; (b) Sakurai, J. a. S., T., Neutron Diffraction of Manganese Ferrite Prepared from Aqueous Solution. *Journal of the Physical Society of Japan* **1967,** *23* (6), 1426; (c) Hastings, J. M.; Corliss, L. M., Neutron Diffraction Study of Manganese Ferrite. *Physical Review* **1956,** *104* (2), 328; (d) Simsa, Z.; Brabers, V., Influence of the degree of inversion on magnetic properties of MnFe<inf>2</inf>O<inf>4</inf>. *Magnetics, IEEE Transactions on* **1975,** *11* (5), 1303-1305.

80. West, A. R., *Basic Solid State Chemistry*. John Wiley & Sons: Chichester, 1988; Vol. S. .

81. van der Zaag, P. J.; Brabers, V. A. M.; Johnson, M. T.; Noordermeer, A.; Bongers, P. F., Comment on ``Particle-size effects on the value of T_{C} of MnFe_{2}O_{4}: Evidence for finite-size scaling''. *Physical Review B* **1995,** *51* (17), 12009.

82. (a) Bhame, S. D. a. J., P. A., Enhanced magnetostrictive properties of Mn substituted cobalt ferrite $Co_{1.2}Fe_{1.8}O_4$. *Journal of Applied Physics* **2006,** *99*, 073901-1-073901-4; (b) Paulsen, J. A., Ring, A. P., Lo, C. C. H., Snyder, J. E., and Jiles, D. C., Manganese-substituted cobalt ferrite magnetostrictive materials fro magnetic stress sensor applications. *Journal of Applied Physics* **2005,** *97*, 044502-1-044502-3; (c) Chen, Y., Snyder, J. E., Dennis, K. W., McCallum, R. W., and Jiles, D. C., Temperature dependence of the magnetomechanical effect in metal-bonded cobalt ferrite composites under torsional strain. *Journal of Applied Physics* **2000,** *87* (9), 5798-5800.

83. Bozorth, R. M.; Tilden, E. F.; Williams, A. J., Anisotropy and Magnetostriction of Some Ferrites. *Physical Review* **1955,** *99* (6), 1788.

84. Rondinone, A. J.; Samia, A. C. S.; Zhang, Z. J., Superparamagnetic Relaxation and Magnetic Anisotropy Energy Distribution in CoFe2O4 Spinel Ferrite Nanocrystallites. *The Journal of Physical Chemistry B* **1999,** *103* (33), 6876-6880.

85. Rondinone, A. J.; Liu, C.; Zhang, Z. J., Determination of Magnetic Anisotropy Distribution and Anisotropy Constant of Manganese Spinel Ferrite Nanoparticles. *The Journal of Physical Chemistry B* **2001,** *105* (33), 7967-7971.

86. (a) Sawatzky, G. A.; Van Der Woude, F.; Morrish, A. H., Mossbauer Study of Several Ferrimagnetic Spinels. *Physical Review* **1969,** *187* (2), 747; (b) Sawatzky, G. A., Van der Woude, F., and Morrish, A. H., Cation Distribution in Octahedral and Tetrahedral Sites of the Ferrimagnetic Spinel $CoFe_2O_4$. *Journal of Applied Physics* **1968,** *39* (2), 1204-1206.

87. Liu, C.; Zou, B.; Rondinone, A. J.; Zhang, Z. J., Reverse Micelle Synthesis and Characterization of Superparamagnetic MnFe2O4 Spinel Ferrite Nanocrystallites. *The Journal of Physical Chemistry B* **2000,** *104* (6), 1141-1145.

88. Gibbs, M. R. J., Magnetostriction: 150 Years from the Discovery. *Physica Scripta*. **1992,** *T45*, 115-119.

89. (a) Yafet, Y. a. K., C., Antiferromagnetic Arrangements in Ferrites. *Physical Review* **1952,** *87* (2), 290-294; (b) Kaplan, T. A., Dwight, K., Lyons, D., and Menyuk, N., Classical Theory of the Ground Spin State in Spinels. *Journal of Applied Physics* **1961,** *32* (3), S13; (c) Tomiyasu, K., Horigane, K., Yokobori, T., Kousaka, Y., Takahashi, M., Hiraka, H., Akimitsu, J., and Yamada, K., Unquenched Geometric Frustration Effect on Spiral Spin Correlation in Magnetically Ordered Phase. *Journal of the Physical Society of Japan* **2009,** *78* (8), 084704-1-084704-5.

90. Gallardo, V.; et al., Magnetic colloids as drug vehicles. *Journal of Pharmaceutical Sciences* **2007**.

91. Dong, H.; Meininger, A.; Jiang, H.; Moon, K.-S.; Wong, C., Magnetic Nanocomposite for Potential Ultrahigh Frequency Microelectronic Application. *Journal of Electronic Materials* **2007,** *36* (5), 593-597.

92. López-López, M. T.; et al., Synthesis and magnetorheology of suspensions of cobalt particles with tunable particle size. *Journal of Physics: Conference Series* **2009,** *149* (1), 012073.

93. Poddar, P.; Gass, J.; Rebar, D. J.; Srinath, S.; Srikanth, H.; Morrison, S. A.; Carpenter, E. E., Magnetocaloric effect in ferrite nanoparticles. *Journal of Magnetism and Magnetic Materials* **2006,** *307* (2), 227-231.

94. Gravchikova, E. A.; et al., Preparation of strontium hexaferrite nanoparticles from oxide glasses. *Doklady Chemistry* **2007,** *415* (2), 193.

95. (a) WHO, *Guideline for drinking water quality*. 3 ed.; Geneva, Switzerland, 2001; Vol. 1; (b) Agency, U. S. E. P., *National Primary Drinking Water Standards*. EPA 816-F-03-016, 2003.

96. Manning, B. A., Hunt, M. L., Amrhein, C., and Yarmoff, J. A., Arsenic (III) and Arsenic(V) Reactions with Zerovalent Iron Corrosion Products. *Environ. Sci. Technol.* **2002,** *36*, 5455-5461.

97. Weckler, B.; Lutz, H. D., Lattice vibration spectra. Part XCV. Infrared spectroscopic studies on the iron oxide hydroxides goethite ([alpha]), akaganéite ([beta]), lepidocrocite ([gamma]), and feroxyhite ([delta]). *European Journal of Solid State and Inorganic Chemistry 35* (8-9), 531-544.

98. (a) Morin, G.; Wang, Y.; Ona-Nguema, G.; Juillot, F.; Calas, G.; Menguy, N.; Aubry, E.; Bargar, J. R.; Brown, G. E., EXAFS and HRTEM Evidence for As(III)-Containing Surface Precipitates on Nanocrystalline Magnetite: Implications for As Sequestration. *Langmuir* **2009,** *25* (16), 9119-9128; (b) Fakih, M.; Davranche, M.; Dia, A.; Nowack, B.; Morin, G.; Petitjean, P.; Châtellier, X.; Gruau, G., Environmental impact of As(V)-Fe oxyhydroxide reductive dissolution: An experimental insight. *Chemical Geology* **2009,** *259* (3-4), 290-303; (c) Giménez, J.; Martínez, M.; de Pablo, J.; Rovira, M.; Duro, L., Arsenic sorption onto natural hematite, magnetite, and goethite. *Journal of Hazardous Materials* **2007,** *141* (3), 575-580; (d) Chowdhury, S. R.; Yanful, E. K., Arsenic and chromium removal by mixed magnetite-maghemite nanoparticles and the effect of phosphate on removal. *Journal of Environmental Management* **2010,** *91* (11), 2238-2247.

99. Sakurai, S.; Namai, A.; Hashimoto, K.; Ohkoshi, S.-i., First Observation of Phase Transformation of All Four Fe2O3 Phases ($\gamma \rightarrow \varepsilon \rightarrow \beta \rightarrow \alpha$-Phase). *Journal of the American Chemical Society* **2009,** *131* (51), 18299-18303.

100. Rao, C. N. R., and Raveau, B., *Transition Metal Oxides: Structure, Properties, and Synthesis of Ceramic Oxides*. 2nd ed.; John Wiley & Sons, Inc.: New York, 1998.

101. Thies-Weesie, D. M. E.; de Hoog, J. P.; Hernandez Mendiola, M. H.; Petukhov, A. V.; Vroege, G. J., Synthesis of Goethite as a Model Colloid for Mineral Liquid Crystals. *Chemistry of Materials* **2007,** *19* (23), 5538-5546.

102. Tejedor-Tejedor, M. I.; Anderson, M. A., "In situ" ATR-Fourier transform infrared studies of the goethite (α-FeOOH)-aqueous solution interface. *Langmuir* **1986,** *2* (2), 203-210.

103. Wang, S.-B.; Min, Y.-L.; Yu, S.-H., Synthesis and Magnetic Properties of Uniform Hematite Nanocubes. *The Journal of Physical Chemistry C* **2007,** *111* (9), 3551-3554.

104. Choong, T. S. Y., Chuah, T. G., Robiah, Y., Gregory Koay, F. L., and Azni, I., Arsenic toxicity, health hazards and removal techniques from water: an overview. *Desalination* **2007,** *217,* 139-166.

105. Agency, U. S. E. P. Ground Water & Drinking Water. http://www.epa.gov/safewater/index.html (accessed 3 March).

106. Jain, A., Raven, K. P., and Loeppert, R. H., Arsenite and Arsentate Adsorption on Ferrihydrite: Surface Charge Reduction and Net OH- Release Stoichiometry. *Environ. Sci. Technol.* **1999,** *33,* 1179-1184.

107. Mondal, P., Majumder, C. B., and Mohanty, B., Laboratory based approaches for arsenic remediation from contaminated water: Recent developments. *J Hazardous Materials B* **2006,** *137,* 464-479.

108. Leist, M., Casey, R. J., and Caridi, The management of arsenic wastes: problems and prospects. *J Hazardous Materials B* **2000,** *76*, 125-138.

109. Kartinen, E. O., Martin, C. J., An overview of arsenic removal processes. *Desalination* **1995,** *103,* 79-88.

110. Kundu, S. a. G., A.K., Analysis and modeling of fixed bed column operations on As(V) removal by adsorption onto iron oxide-coated cement(IOCC). *J Colloid and Interface Science* **2005,** *290* (1), 52-60.

111. Guo, X., and Chen, F., Removal of Arsenic by Bead Cellulose Loaded with Iron Oxyhydroxide from Groundwater. *Environ Sci Technol* **2005,** *39,* 6808-6818.

112. Zhang, W., Singh, P., Paling, E., and Delides, S., Arsenic removal from contaminated water by natural iron ores. *Minerals Engineering* **2004,** *17*, 517-524.

113. Bang, S., Korfiatis, G. P., and Meng, X., Removal of arsenic from water by zero-valent iron. *J Hazardous Materials* **2005,** *121,* 61-67.

114. (a) Bang, S., Korfiatis, G. P., and Meng, X., Removal of arsenic from water by zero-valent iron. *J Hazardous Materials* **2005,** *121,* 61-67; (b) Ramos, M. A. V. Y., W.;

Li,X.; Koel, B.E.; and Zhang, W., Simultaneous Oxidation and Reduction of Arsenic by Zero-Valent Iron Nanoparticles: Understanding the Significance of the Core-Shell Structure. *Journal of Physical Chemistry C* **2009,** *113* (33), 14591-4.

115. Dhar, R. K. B., B.K.; Samanta, G.; Mandal, B.K.; Charkraborti, D.; Roy, S.; Jafar, A.; Islam, A.; Ara, G.; Kabir, S.; Khan, A.W.; Ahmed, S.A.; Hadi, S.A., Groundwater arsenic calamity in Bangladesh. *Current Science* **1997,** *73* (1), 48-59.

116. McKay, G.; Blair, H. S.; Gardner, J., Adsorption of dyestuffs onto chitin. External mass transfer processes. *Journal of Applied Polymer Science* **1982,** *27* (11), 4251-4261.

117. (a) Beer, P. D., Transition-Metal Receptor Systems for the Selective Recognition and Sensing of Anionic Guest Species. *Accounts of Chemical Research* **1998,** *31* (2), 71-80; (b) van Veggel, F. C. J. M.; Verboom, W.; Reinhoudt, D. N., Metallomacrocycles: Supramolecular Chemistry with Hard and Soft Metal Cations in Action. *Chemical Reviews* **1994,** *94* (2), 279-299.

118. Palmer, C. D. a. P., R.W., Natural Attenuation of Hexavalent Chromium in Groundwater and Soils. *US Enviromental Protection Agency* **1994,** *EPA/540/S-94/505*.

119. Stearns, D. M.; Kennedy, L. J.; Courtney, K. D.; Giangrande, P. H.; Phieffer, L. S.; Wetterhahn, K. E., Reduction of Chromium(VI) by Ascorbate Leads to Chromium-DNA Binding and DNA Strand Breaks in Vitro. *Biochemistry* **1995,** *34* (3), 910-919.

120. Palmer, C. D.; Wittbrodt, P. R., Processes Affecting the Remediation of Chromium-Contaminated Sites. *Environmental Health Perspectives* **1991,** *92* (ArticleType: research-article / Full publication date: May, 1991 / Copyright © 1991 The National Institute of Environmental Health Sciences (NIEHS)), 25-40.

121. Nriagu, J. O. a. N., E., *Chromium in the Natural and Human Environments*. John Wiley & Sons: New York, 1988; Vol. 20.

VITA

Lisa A. Vaughan

Lisa Vaughan was born in Austin, TX to Paul and Beth Linhardt. She attended the Tulane University and graduated with a B.S. in Chemistry, minor in Mathematics in 2006. Lisa conducted her graduate work at the Georgia Institute of Technology in Atlanta, Georgia under the direction of Z. John Zhang. In 2011, she graduated with a Ph.D. in Chemistry.